



5-2013

Transient Liquid Phase Bonding of Titanium-, Iron- and Nickel- Based Alloys

A. H. M. Esfakur Rahman

Follow this and additional works at: <https://commons.und.edu/theses>

 Part of the [Engineering Commons](#)

Recommended Citation

Rahman, A. H. M. Esfakur, "Transient Liquid Phase Bonding of Titanium-, Iron- and Nickel- Based Alloys" (2013). *Theses and Dissertations*. 885.

<https://commons.und.edu/theses/885>

This Dissertation is brought to you for free and open access by the Theses, Dissertations, and Senior Projects at UND Scholarly Commons. It has been accepted for inclusion in Theses and Dissertations by an authorized administrator of UND Scholarly Commons. For more information, please contact zeinebyousif@library.und.edu.

TRANSIENT LIQUID PHASE BONDING OF TITANIUM-, IRON- AND NICKEL-
BASED ALLOYS

by

A. H. M. Esfakur Rahman

Bachelor of Science, Bangladesh University of Engineering and Technology, 2004

Master of Science, Kongju National University, 2008

A Dissertation

Submitted to the Graduate Faculty

of the

University of North Dakota

In partial fulfillment of the requirements

for the degree of

Doctor of Philosophy

Grand Forks, North Dakota

May

2013

UMI Number: 3587453

All rights reserved

INFORMATION TO ALL USERS

The quality of this reproduction is dependent upon the quality of the copy submitted.

In the unlikely event that the author did not send a complete manuscript and there are missing pages, these will be noted. Also, if material had to be removed, a note will indicate the deletion.



UMI 3587453

Published by ProQuest LLC (2013). Copyright in the Dissertation held by the Author.

Microform Edition © ProQuest LLC.

All rights reserved. This work is protected against unauthorized copying under Title 17, United States Code



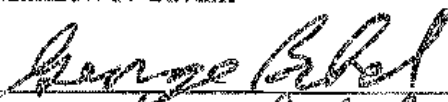
ProQuest LLC.
789 East Eisenhower Parkway
P.O. Box 1346
Ann Arbor, MI 48106 - 1346

Copyright 2013 A H M Esfakur Rahman

This dissertation, submitted by Esfakur Rahman in partial fulfillment of the requirements for the degree of Doctor of Philosophy from the University of North Dakota, has been read by the Faculty Advisory Committee under whom the work has been done, and is hereby approved.




Dr. Matthew N Cavalli



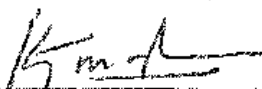
Dr. George Bibel



Dr. William Semke



Dr. Bishu Bandyopadhyay

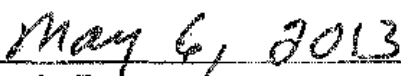


Dr. Kanishka Marasinghe

This dissertation is being submitted by the appointed advisory committee as having met all of the requirements of the Graduate School at the University of North Dakota and is hereby approved.



Dr. Wayne Swisher
Dean of the Graduate School



Enter the Date

Title	Transient Liquid Phase Bonding of Titanium-, Iron- and Nickel-based Alloys
Department	Mechanical Engineering
Degree	Doctor of Philosophy

In presenting this dissertation in partial fulfillment of the requirements for a graduate degree from the University of North Dakota, I agree that the library of this University shall make it freely available for inspection. I further agree that permission for extensive copying for scholarly purposes may be granted by the professor who supervised my dissertation work or, in his absence, by the Chairperson of the department or the dean of the Graduate School. It is understood that any copying or publication or other use of this dissertation or part thereof for financial gain shall not be allowed without any written permission. It is also understood that due recognition shall be given to me and to the University of North Dakota in any scholarly use which may be made of any material in my dissertation.

A H M Esfakur Rahman
10/3/2013

TABLE OF CONTENTS

LIST OF FIGURES	ix
LIST OF TABLES	xv
ACKNOWLEDGEMENT	xvii
ABSTRACT	xviii
CHAPTER	
I. INTRODUCTION	
Metal Joining Processes	1
Diffusion Bonding	1
Solid-Phase Diffusion Bonding	2
Transient Liquid Phase (TLP) Bonding	2
TLP Bonding Steps	3
TLP bonding parameters and interlayers	4
Titanium-based Alloys	5
Iron-based Alloys	6
Nickel-based Alloys	8
II. TLP BONDING OF COMMERCIALY PURE ALLOYS	
Specimen Fabrication	10
Ti Joints	10
Fe Joints	11
Ni Joints	12

Microstructural Characterization	12
Mechanical Testing	12
Results and Discussion	13
Ti-Ti Bonding	13
Microstructures	13
Mechanical Properties	19
Conclusions	22
Fe-Fe Bonding	22
Microstructures	22
Mechanical Properties	37
Conclusions	40
Ni-Ni Bonding	40
Microstructure	40
Mechanical Properties	49
Conclusion	49
III. MODELLING OF TRANSIENT LIQUID PHASE DIFFUSION BONDING	
Introduction	50
TLP Modeling	50
Model 1 (Stationary Interface)	51
Model 2 (Moving Solid/Liquid Interface)	52
Modeling of Diffusion Controlled Transformation Using Thermodynamic and Kinetic Database	58
Multicomponent Diffusion Model	59
Atomic Mobility	61

Optimization of Mobility Parameter	62
Determination of Interdiffusion Coefficient	62
Moving Boundary Model	64
Ni-Cu Binary System	66
Experimental Information	66
Experimental Procedure	68
Results and Discussion	69
Ni-Al Binary System	75
Ni-(Au-Gc) Ternary System	77
Conclusions	78
IV. TLP BONDING OF INDUSTRIALLY-IMPORTANT ALLOYS	
Specimen Fabrication	80
SS 321 Joints	80
Inconel 718 Joints	81
Ti-6Al-4V Joints	81
Microstructural Characterization	82
Mechanical Properties	82
Results and Discussion	82
TLP Bonding of SS 321	82
Microstructure	82
Mechanical Properties	96
TLP Bonding of Inconel 718	98
Microstructure	98

Mechanical Properties	106
TLP Bonding of Ti-6Al-4V	107
Microstructure	107
Conclusions	111
V. CONCLUSIONS	113
APPENDICES	117
REFERENCES	129

LIST OF FIGURES

Figure	Page
1. a) Schematic representation of diffusion bond geometry, b) diffusion bonded microstructure sample, and c) tensile specimen (top – before bonding, bottom – after bonding)	10
2. SEM images of diffusion bonded Ti using Ag interlayer at 1030°C for 10 h, a) bond center line, b) ~ 80 μm away from the bond centerline, c) ~ 160 μm away from the bond centerline and d) the schematic representation of different regions from the bond centerline to the interior of base material	13
3. SEM images of diffusion bonded titanium using Ag interlayer at 1030°C for 30 h	14
4. Ti-Ag phase diagram generated in ThermoCalc version TCW5	14
5. SEM images of diffusion bonded titanium using Cu interlayer at 900°C for 10 h	15
6. SEM images of diffusion bonded titanium using Cu interlayer a) at 1000°C for 10 h and b) enlarged image of (a)	16
7. SEM images of diffusion bonded titanium using Cu interlayer a) at 1020°C for 10 h and b) enlarged image of (a)	16
8. Ti-Cu phase diagram generated in ThermoCalc version TCW5	17
9. SEM images of diffusion bonded titanium using Cu interlayer at 1100°C for 10 h	17
10. a) SEM images of diffusion bonded titanium without interlayer at 980° C for 20 h (etched with 8% HF and 4% HNO ₃), and b) magnified image of (a)	18
11. SEM images of fracture surfaces of (a) pure Ti, (b) diffusion bonded Ti using Ag at 1030°C for 10h , (c) diffusion bonded Ti using Cu interlayer at 1030°C for 10 h; (d), (e) and (f) are magnified image of (a), (b) and (c), respectively	20
12. Fracture surface of tensile specimen, faying surfaces were polished by hand before bonding	20
13. SEM images of fracture surface of Ti-Ti bonded at 980°C for 10h, the bonding surface was polished by a) hand (grit# 600) and b) wheel (grit#120) before bonding	21

14. (a) SEM images of diffusion bonded Fe using Al interlayer (0.1 mm) at 900°C for 10 h (surface finish 600 μm) and (b) enlarged image of (a)	22
15. Concentration profiles of Al and Fe in diffusion bonded Fe using Al interlayer (0.1 mm) at 900°C for 10 h	23
16. Fe-Al phase diagram generated in ThermoCalc version TCW5	23
17. Diffusion bonded cp-Fe at 900°C for 20 h using Al interlayer (100 μm)	24
18. SEM images of diffusion bonded Fe using Au-20Sn interlayer (100 μm) at 600°C for 10 h	24
19. SEM image of diffusion bonded Fe using Au-20Sn eutectic alloy interlayer (100 μm) at 650°C for 10 h	25
20. Au-Sn phase diagram generated in ThermoCalc version TCW5	26
21. SEM images of diffusion bonded Fe using Cu interlayer (25 μm) at (a) 1070°C for 10 h and (b) 1085°C for 30 h	26
22. Fe-Cu phase diagram generated in ThermoCalc version TCW5	27
23. SEM image of diffusion bonded Fe using Cu interlayer (25 μm) at 1090°C for 10 h.....	28
24. SEM images of diffusion bonded Fe using Cu interlayer (25 μm) at 1100°C for (a) 3 h and (b) 4 h	29
25. (a) SEM image of diffusion bonded Fe using Cu interlayer (25 μm) at 1100°C for 5 h.....	29
26. (a) BSE mode image of diffusion bonded Fe using Cu interlayer (25 μm) at 1100°C for 10 h, element mapping of (b) Cu and (c) Fe taken from the joint area	30
27. (a) SEM image of diffusion bonded Fe using Au-12Ge interlayer (100 μm) at 900°C for 1 h	31
28. Au-Fe Phase diagram [38]	32
29. Element mapping of Fe and Au of diffusion bonded Fe using Au-12Ge interlayer (100 μm) at 900°C for 1 h taken from the bond centerline	33
30. SEM image of diffusion bonded Fe using Au-12Ge interlayer (100 μm) (a) at 900°C for 10 h and (b) enlarged image of (a)	33
31. SEM image of diffusion bonded Fe using Au-12Ge interlayer (100 μm) at 920°C for 15 h	34

32. SEM images of diffusion bonded Fe using Au-12Ge interlayer (100 μm) at (a) 950°C and (b) 990°C for 15 h	35
33. Schematic of the test geometry of tensile specimen	37
34. Optical micrographs of raw, normalized and diffusion bonded tensile specimen	39
35. SEM image of diffusion bonded Ni using Al interlayer (100 μm) at 800°C for 10 h.....	41
36. Ni-Al equilibrium diagram generated in ThermoCalc version TCW5	41
37. (a) SEM image of diffusion bonded Ni using Al interlayer (100 μm) at 800°C for 30 h and (b) magnified image of (a)	42
38. (a) SEM image of diffusion bonded Ni using Al interlayer (25 μm) at 800°C for 10 h and (b) magnified image of (a)	43
39. Concentration profiles of Al in diffusion bonded Ni using Al interlayer (25 μm) at 800°C for 10 h	43
40. (a) SEM image of diffusion bonded Ni using Au-12Ge interlayer (100 μm) at 900°C for 1 h and (b) magnified image of (a)	44
41. (a) SEM image of diffusion bonded Ni using Au-12Ge interlayer (100 μm) at 900°C for 15 h and (b) magnified image of (a)	45
42. (a) SEM image of diffusion bonded Ni using Au-12Ge interlayer (100 μm) at 960°C for 10 h and (b) magnified image of (a)	46
43. SEM images of diffusion bonded Ni using Cu interlayer (25 μm) at 1070°C for (a) 10 h and (b) 15 h	47
44. SEM images of diffusion bonded Ni using Cu interlayer (25 μm) at 1100°C for 10 h	47
45. Schematic diagram showing the concentration profile across a TLP bond at one instant in time. Only half of the joint is shown; the other half (from $x = -L$ to $x = 0$) will be symmetrical [45]	55
46. Schematic of concentration-distance profile	64
47. The α phase growing into β phase in a binary system under isothermal conditions. The corresponding concentration profile is shown in the lower left part of the figure and the phase diagram in the lower right part of the figure [62]	65
48. Temperature dependency of self-diffusion coefficient of Cu [63]	67
49. Temperature dependency of self-diffusion coefficient of Ni [64]	67

50. Temperature dependency of tracer diffusion coefficient of Ni in pure Cu [65]	67
51. Temperature dependency of tracer diffusion coefficient of Cu in pure Ni [66]	68
52. Calculated thermodynamic factor (θ) of the fcc phase of Ni-Cu alloy at 900°C and 1000°C (ThermoCalc/DICTRA database ssol4)	69
53. The calculation scheme in DICTRA for diffusion controlled transformation [62]	70
54. Schematic of problem setup in DICTRA	72
55. Experimental [68] and calculated interdiffusion coefficient of Ni-Cu system at 1000°C	72
56. (a) SEM image of diffusion bonded Ni using Cu interlayer (25 μ m) at 1050°C for 15h and (b) concentration profile of Cu from the bond centerline to the interior of base metal	73
57. (a) SEM image of diffusion bonded Ni using Cu interlayer (25 μ m) at 1070°C for 10 h and (b) concentration profile of Cu from the bond centerline to the interior of base metal	74
58. SEM image of diffusion bonded Ni using Cu interlayer (25 μ m) at 1100°C for 10 h and concentration profile of Cu from the bond centerline to the interior of base metal	74
59. Concentration profile of Al in Ni-Al diffusion couple at 800°C for 10h, interlayer thickness: 100 μ m	76
60. Concentration profile of Al in Ni-Al diffusion couple at 800°C for 10h, interlayer thickness 25 μ m	77
61. Concentration profiles of Au and Ge in Ni-(Au-Ge) diffusion couple at 900°C for 10h, interlayer thickness: 100 μ m.....	78
62. (a) SEM image of diffusion bonded SS 321 using Au-12Ge interlayer (100 μ m) at 900°C for 1 h and (b) magnified image of (a)	83
63. (a) SEM image of diffusion bonded SS 321 using Au-12Ge interlayer (100 μ m) at 950°C for 10 h and (b) magnified image of (a)	84
64. (a) SEM image of diffusion bonded SS 321 using Au-12Ge interlayer at 1010°C for 15 h and (b) magnified image of (a)	85
65. (a) SEM image of diffusion bonded SS 321 using Au-12Ge interlayer at 1050°C for 15 h and (b) magnified image of (a)	86
66. (a) SEM image of diffusion bonded SS 321 using Au-12Ge interlayer at 1050°C for 15 h in vacuum with cooling in air and (b) magnified image of (a)	87

67. (a) SEM image of diffusion bonded SS 321 at 1050°C for 20 h using Au-12Ge interlayer in vacuum and quenched in water and (b) magnified image of (a)	88
68. (a) SEM image of diffusion bonded SS 321 using Au-12Ge interlayer at 1050°C for 20 h in vacuum, cooled in flow of water and (b) magnified image of (a)	89
69. (a) SEM image of diffusion bonded SS 321 using Au-12Ge interlayer at 1050°C for 20 h in vacuum and air-cooled and (b) magnified image of (a). Image was taken from the center of the sample	90
70. SEM image of diffusion bonded SS 321 using Au-12Ge interlayer at 1050°C for 20 h in vacuum and air-cooled, image taken from the edge of the sample	91
71. (a) SEM image of diffusion bonded SS 321 using Au-12Ge interlayer at 1050°C for 20 h in argon and cooled in air and (b) magnified image of (a)	91
72. (a) SEM image of diffusion bonded SS 321 using Au-12Ge interlayer at 1050°C for 20 h, bonded in argon, cooled in flow of water and (b) magnified image of (a) ..	92
73. (a) SEM image of diffusion bonded SS 321 using Au-20Sn interlayer (100µm) at 750°C for 10 h and (b) magnified image of (a)	94
74. SEM image of diffusion bonded SS 321 using Au-20Sn interlayer (100µm) at 800°C for 10 h	95
75. SEM image of diffusion bonded SS 321 at 1100°C for 10 h using Cu interlayer (25 µm)	95
76. SEM image of diffusion bonded SS 321 at 1120°C for 10 h using Cu interlayer (25 µm)	96
77. (a) SEM image of diffusion bonded Inconel 718 using Cu interlayer (25 µm) at 1050°C for 15 h in vacuum with slow cooling and (b) magnified image of (a)	99
78. SEM image of diffusion bonded Inconel 718 using Cu (25 µm) at 1150°C for 5 h in vacuum with slow cooling (4°C/min)	100
79. (a) SEM image of diffusion bonded Inconel 718 using Au-12Ge (100 µm) at 950°C for 15 h in vacuum and slow cooling and (b) magnified image of (a)	101
80. SEM image of diffusion bonded Inconel 718 using Au-12Ge (100 µm) at 1050°C for 15 h in vacuum and slow cooled	102
81. (a) SEM image of diffusion bonded Inconel 718 using Au-12Ge (100 µm) at 1050°C for 15 h in vacuum and quenched in water and (b) magnified image of (a)	103

82. (a) SEM image of diffusion bonded Inconel 718 using Au-12Ge (100 μm) at 1050°C for 15 h in vacuum and cooled in air and (b) magnified image of (a).....	104
83. SEM image of diffusion bonded Inconel 718 using Au-12Ge (100 μm) at 1050°C for 20 h in vacuum and cooled in air	105
84. (a) SEM image of diffusion bonded Ti-6Al-4V using Cu (25 μm) interlayer at 900°C for 10 h in vacuum, slow-cooled and (b) magnified image of (a)	107
85. (a) SEM image of diffusion bonded Ti-6Al-4V using Cu (25 μm) interlayer at 950°C for 10 h in vacuum, slow-cooled and (b) magnified image of (a)	108
86. SEM image of diffusion bonded Ti-6Al-4V using Cu (25 μm) interlayer at 950°C for 10 h in vacuum and slow-cooled	109
87. (a) SEM image of diffusion bonded Ti-6Al-4V using Cu (25 μm) interlayer at 1000°C for 10 h in vacuum, slow-cooled and (b) magnified image of (a)	110
88. SEM image of diffusion bonded Ti-6Al-4V using Cu (25 μm) interlayer at 1000°C for 10 h in vacuum, slow-cooled in furnace	111
89. Diffusion couple used for simulation in DICTRA	127

LIST OF TABLES

Table	Page
1. Summary of the microstructure of TLP bonded Ti using Ag and Cu interlayer (100 μm)	18
2. Ultimate tensile strengths of diffusion bonded Ti samples with Ag, Cu interlayers and without any interlayer	19
3. Summary of the microstructure of TLP bonded Fe using Al, Au-20Sn and Cu interlayer	36
4. Summary of the microstructure of TLP bonded Fe using Au-12Ge interlayer	37
5. Ultimate tensile strengths (UTS) of diffusion bonded Fe using Cu (25 μm) interlayer	38
6. Ultimate tensile strengths (UTS) of diffusion bonded Fe using Au-12Ge (100 μm) interlayer	39
7. Summary of the microstructure of TLP bonded Ni using Al, Au-12Ge and Cu interlayer	48
8. Assessed mobility parameter in the fcc Ni-Cu alloy	71
9. Compositions (wt. %) of AISI type stainless steel 321 (SS 321)	82
10. Summary of the microstructure of TLP bonded SS 321 using Au-12Ge bonded at 1050°C for 20 h with different environment and cooling method	93
11. Tensile strengths of TLP bonded SS 321 using Au-12Ge interlayer	97
12. Composition (wt. %) of Inconel 718 superalloy	99
13. EDS analysis of diffusion bonded Inconel 718 using Au-12Ge (100 μm) at 950°C for 15 h taken from 5 points shown in Figure 79 (b)	101
14. Summary of the microstructure of TLP bonded Inconel 718 using Cu and Au-12Ge interlayer in vacuum	106
15. Tensile strength of diffusion bonded Inconel 718	107

16. Summary of the microstructure of TLP bonded Ti-6Al-4V using interlayer in vacuum104

ACKNOWLEDGEMENTS

I would like to show my cordial gratitude and profound respect to my supervisors Associate Professors Matthew Cavalli, William Semke, Professors George Bibel, Bishu Bandyopadhyay, Department of Mechanical Engineering, and Professor Kanishka Marasinghe, Department of Physics, University of North Dakota, Grand Forks in appreciation of their continuous guidance, constructive suggestions and keen supervision through my entire work. Their continuous efforts made me acquainted with the world of the state-of-the-art research. According to my candid perception, I acknowledge that this dissertation would not be comprehensive without their shrewd observation. I am thankful to all my professors to whom I met and received cordial guidance in course of academic life. Thanks to all administrative staff of College of Engineering and Mines.

This work has been benefited directly and/or indirectly by a lot of people. I wish to pay my heartiest thank to machine shop instructors Gary Dubuque and Jay Evenstad. I am grateful to all my former and present Lab members without whom my works would have been more difficult.

Financial support from the National Science Foundation (Award #DMR-0907616) and the UND Senate Scholarly Activities Committee (SAAC) during the course of this work is gratefully acknowledged.

ABSTRACT

The operating temperature of land-based gas turbines and jet engines are ever-increasing to increase the efficiency, decrease the emissions and minimize the cost. Within the engines, complex-shaped parts experience extreme temperature, fatigue and corrosion conditions. Ti-based, Ni-based and Fe-based alloys are commonly used in gas turbines and jet engines depending on the temperatures of different sections. Although those alloys have superior mechanical, high temperature and corrosion properties, severe operating conditions cause fast degradation and failure of the components. Repair of these components could reduce lifecycle costs. Unfortunately, conventional fusion welding is not very attractive, because Ti reacts very easily with oxygen and nitrogen at high temperatures, Ni-based superalloys show heat affected zone (HAZ) cracking, and stainless steels show intergranular corrosion and knife-line attack. On the other hand, transient liquid phase (TLP) bonding method has been considered as preferred joining method for those types of alloys.

During the initial phase of the current work commercially pure Ti, Fe and Ni were diffusion bonded using commercially available interlayer materials. Commercially pure Ti (Ti-grade 2) has been diffusion bonded using silver and copper interlayers and without any interlayer. With a silver (Ag) interlayer, different intermetallics (AgTi , AgTi_2) appeared in the joint centerline microstructure. While with a Cu interlayer eutectic mixtures and Ti-Cu solid solutions appeared in the joint centerline. The maximum tensile strengths achieved were 160 MPa, 502 MPa, and 382 MPa when Ag, Cu and no

interlayers were used, respectively. Commercially pure Fe (cp-Fe) was diffusion bonded using Cu (25 μm) and Au-12Ge eutectic interlayer (100 μm). Cu diffused predominantly along austenitic grain boundaries in all bonding conditions. Residual interlayers appeared at lower bonding temperature and time, however, voids were observed in the joint centerline at higher joining temperature and time. Dispersed Au-rich particles were observed in the base metal near interface. The highest ultimate tensile strengths obtained for the bonded Fe were 291 ± 2 MPa using a Cu interlayer at 1030°C for 10 h and 315 ± 4 MPa using a Au-12Ge interlayer at 950°C for 15 h. Commercially pure Ni (cp-Ni) was diffusion bonded using a Al, Au-12Ge or Cu interlayer. The formation of intermetallics could not be avoided when Al interlayer was used. Even though no intermetallics were obtained with Au-12Ge or Cu interlayer, appreciable strength of the joint was not found. Next, the simple bonding systems were modeled numerically. It is hoped that the simple models can be extended for higher order alloys. The modeling of TLP joint means to come up with a mathematical model which can predict the concentration profiles of diffusing species. The concentration dependence of diffusivity in a multi-component diffusion system makes it complicated to predict the concentration profiles of diffusing species. The so-called chemical diffusivity can be expressed as a function of thermodynamic and kinetic data. DICTRA software can calculate the concentration profiles using appropriate mobility and thermodynamic data. It can also optimize the diffusivity data using experimental diffusivity data. Then the optimized diffusivity data is stored as mobility data which is a linear function of temperature. In this work, diffusion bonding of commercially pure Ni using Cu interlayers is reported. The mobility parameters of Ni-Cu alloy binary systems were optimized using DICTRA/Thermocalc

software from the available self-, tracer and chemical diffusion coefficients. The optimized mobility parameters were used to simulate concentration profiles of Ni-Cu diffusion joints using DICTRA/Thermocalc software. The calculated and experimental concentration profiles agreed well at 1100 °C. This method could not be extended for higher order alloys because of the lack of appropriate thermodynamic and kinetic database.

In the third phase industrially important alloys such as SS 321, Inconel 718 and Ti-6Al-4V were diffusion bonded. Diffusion bonded SS 321 with Au-12Ge interlayer provided the best microstructure when bonded in either vacuum or argon at 1050°C for 20 h and cooled in air. The maximum strength obtained of the joint was 387±4 MPa bonded in vacuum at 1050°C for 20 h and cooled in air. The microstructure of joint centerline of diffusion bonded Inconel 718 using Au-12Ge interlayer at 1050°C for 15 h and cooled in air consisted of residual interlayer (1.3-2.5 µm). The residual interlayer was disappeared by increasing the bonding time by 5 h, however, pores appeared in the joint centerline. As a result, the strength obtained for bonded Inconel 718 was much lower than that of the base alloy. The joint centerline microstructure of bonded Ti-6Al-4V using Cu interlayer was free of intermetallics and solid solution of Cu and base alloy. The strength of the joint is yet to be determined.

CHAPTER I

INTRODUCTION

Metal Joining Processes

Joining of metals and alloys is essential for fabrication and assembly. Reliability, speed and cost of fabrication and assembly motivated the development of a wide range of joining technologies. There are five basic joining processes which cover almost all metal joining: welding, brazing, soldering, adhesive bonding and mechanical fastening. Gas Metal Arc (GMA) welding is the most common metal joining process; it is a fusion welding process. Other fusion welding processes are gas welding, laser welding and electron beam welding. All fusion welding processes are liquid-phase welding. Solid phase diffusion bonding, stir welding, explosive welding and forge welding can be categorized as solid-phase welding.

Diffusion Bonding

Diffusion bonding is a general term for any joining process in which bonding is primarily due to atomic interdiffusion across the interface. Shirzadi [1] categorized diffusion bonding as a subdivision of both solid-phase and liquid phase welding. To avoid oxidation, diffusion bonding is performed under inert atmosphere (helium or argon) unless the oxide layer is thermodynamically unstable at bonding temperature (silver). Silver can be diffusion bonded in air. Diffusion bonding can be divided into two categories:

- Solid-phase Diffusion Bonding
- Transient Liquid Phase (TLP) Diffusion Bonding

Solid-phase Diffusion Bonding

In this joining process, two flat surfaces to be bonded are held together by an applied pressure and heated to an elevated temperature. The joining temperature ranges from 50 to 90% of the melting temperature of the base metal (absolute temperature) and bonding time ranges from a few minutes to few days. Since solid-state diffusion is extremely slow in metals, this process would take unreasonable long time to join industrially important alloys.

Transient Liquid Phase (TLP) Bonding

Transient liquid phase (TLP) bonding refers to diffusion bonding in which a filler metal with a relatively low melting temperature is used. TLP bonding is a widely used metal joining process [2]. This bonding method has the potential of fabricating high-strength joints with simple or complex microstructures depending on the type of interlayer used. TLP bonding is evolved from high temperature fluxless vacuum brazing [3,4]. The combination of bonding temperature, bonding time and interlayer material is chosen in such a way so that significant atomic transport from interlayer materials into base materials (and vice-versa) takes place during bonding. Boron, for example, is used as a melting point depressant in interlayers for TLP bonding of nickel-based alloys [5], because boron atoms can diffuse quickly through interstices in the face-centered cubic transition metal. The TLP process is very similar to the high-temperature brazing process. The main differences between TLP and brazing are the solidification behavior and the presence of interdiffusion. In TLP bonding, a low melting temperature interlayer is

inserted in between base metals. An interlayer for a TLP bonding can be a simple metal foil or an alloy containing a melting point depressant (e.g. B, Si, P) or a eutectic alloy with a low melting temperature. In certain cases, interlayers form low melting point eutectics with the base metals and melt below their original melting points [6]. The composition of the interlayer changes by interdiffusion and the liquid interlayer solidifies isothermally. The re-melt temperature of the TLP bonded region is similar to the melting temperature of parent alloy. This melting shift of the joint area differentiates TLP bonding from high-temperature brazing. Ideally, the solidified bond should consist of a primary solid solution of base metal with a composition very close to that of the base metal and free from intermetallics and second phase particles. TLP joints suffer limited amounts of microstructure disruption and joints formed after the solidification can have a microstructure similar to that of base alloys. This is why the mechanical properties of the TLP bonded region are often very close to that of the parent alloys [7].

TLP Bonding Steps

A typical TLP joint involves three steps – substrate dissolution, isothermal solidification and solid state homogenization. Since the melting temperature of the filler or interlayer materials is always lower than that of the parent metal, the filler or interlayer materials form a liquid at the bonding temperature. This liquid partially dissolves parent materials at the liquid/solid interfaces until a local equilibrium is achieved. The activation energy for base metal dissolution is usually very low compared to that for interstitial diffusion [8] as it does not need long range diffusion in solids. After the initial dissolution of base metal, the interlayer atoms begin to diffuse into the base metals. As these atoms continue to diffuse, the liquid interlayer thins. The liquid layer will be removed completely if

sufficient time is given. This step is known as the isothermal solidification stage. It's a much slower process than the substrate dissolution stage. However, the time required to finish this stage is dependent on the specific system and ranges from a few minutes to several hours. Additional holding time is required after isothermal solidification to homogenize filler or interlayer elements into the base materials. In a typical TLP bonding process, these three steps are sequential and are assumed to be not parallel. However, the formation of undesirable phases, for example intermetallics, brings the above assumption into questions.

TLP Bonding Parameters and Interlayers

Most TLP bonding processes are done in vacuum to control oxide formation on the faying surfaces and the interlayer. For some cases, an argon environment can be used if porosity is not a problem. Although it is almost impossible to remove the oxide layer from the faying surfaces, under inert atmosphere (vacuum or argon environment) the kinetics of oxidation are controllable. The heating methods could be radiant heating in a vacuum furnace, induction heating or infrared heating [3,9,10]. Usually a fixed clamping load is used for TLP bonding though it changes during the bonding process because the coefficients of thermal expansions are different for the jigs, clamping bolts, foils and parent metals. Also, after diffusion of the interlayer materials into the base metals, the overall length shrinks a bit. Surface finish before bonding, bonding temperature, and bonding time can be adjusted to obtain optimum joint quality.

An interlayer could be a thin foil or amorphous filler material. Ideally, an interlayer should melt below the melting temperature of the parent metal and not form intermetallics with parent metals, which will detrimentally affect the strength of the joint.

The thickness of the interlayer varies from a few μm to 100 μm . For thinner interlayers, sputter coatings are used. To obtain low melting point interlayers melting point depressants are introduced. The most common melting point depressants are boron, phosphorous and silicon [11-12]. These melting point depressants diffuse faster into the base metals but it is to be noted that these could form intermetallics and affect the strength. Sometimes binary eutectic alloys with low melting temperatures are also used as an interlayer [13].

Titanium-based Alloys

Titanium (Ti) and its alloys are considered technically superior and cost-effective engineering materials for use in industrial applications. They have been widely used in aerospace and chemical industries because of their high specific strength, good erosion resistance and favorable high temperature properties [14-16]. With the increased use of Ti and its alloys, the joining of Ti and its alloys is of great interest. Unfortunately, welding of Ti and Ti alloys is difficult as they are highly chemically reactive at high temperatures and tend to oxidize at very low partial pressures of oxygen. During the welding process, Ti alloys pick up oxygen and nitrogen from the atmosphere very easily [17]. As a result, diffusion bonding is a preferred joining method for Ti and Ti alloys.

Many reports on diffusion bonding and transient liquid phase bonding of Ti and Ti alloys have been published. Elrefaey *et al.* [18] reported diffusion bonding of Ti to low carbon steel using a copper-based interlayer (Cu-12Mn-2Ni, wt.%). The optimum parameters were found to be 850°C for 90 min. However, Cu-Ti intermetallics were formed in the bondline. The optimum bonding strength (tensile-shear) also occurred at 850°C for 90 min when an Ag-Cu-Zn interlayer was used [19]. Kundu *et al.* [20] conducted diffusion

bonding of titanium to 304 stainless steel using copper interlayers. The strength of the bond reached that of base Ti (319 MPa) for the sample bonded at 900°C for 1.5 h and the strength decreased with increasing bonding temperature due to the higher volume fraction of intermetallics. Dezellus *et al.* [21] performed transient liquid phase bonding of titanium to aluminum nitride using a Cusil (28Cu-Ag) interlayer. In this bonding process, Ti formed different intermetallics with copper. As a result, the copper content of the interlayer alloy decreased but the layer still remained in the liquid state. They observed that the solidification occurred faster at 795°C than at 850°C due to fast formation of the Cu-rich compound TiCu₄.

Gui-Sheng *et al.* [14] reported the bonding of a Ti-22Al-25Nb alloy using a Ti-15Cu-15Ni interlayer (melting point, 932°C). The authors found the optimum parameters in terms of strength were 970°C for 90 min using slow cooling. The strength reached 93% of the base alloy. Sheng *et al.* [22] reported on phase transformation superplastic diffusion bonding of a titanium alloy to stainless steel without using any interlayer. When a material is repeatedly heated and cooled in a transformation temperature range, it can be greatly deformed. This phenomenon is known as dynamic superplasticity. Using the optimum parameters (maximum and minimum temperature, number of heating and cooling cycles, specific pressure and heating rate) a tensile strength of 307 MPa (96.8% of the strength of Ti) was obtained.

Iron-based Alloys

Stainless steels (SS) are one of the two material families that are often used in hot sections of aero-engines and power generation turbines along with nickel-based superalloys. Stainless steels are also used in process plants, petrochemical industries,

pump and valve shafts, steam generators, expansion joints, super-heaters, re-heaters, etc. because of their high strength, ductility, resistance to creep and resistance to corrosion at elevated temperatures. Aero-engines and gas turbines are primarily designed for the optimum efficiency and output within the limit of available technology. Within the engines, complex-shaped parts experience extreme temperature, fatigue and corrosion conditions. Due to high operating temperatures increased effects from creep, fatigue and corrosion cause rapid degradation and failure of the components. Any means to repair these damages will increase their total part life and keep the costs to a minimum.

Fusion welding processes, which typically involve relatively large-scale melting of the parent metal at the joint-line and introduction of filler materials, are the most common metal joining processes. However, these joining processes have some adverse effects. For example, fusion welded T91 martensitic steels are prone to hot cracking [23]. Duplex stainless steels containing 50:50 ratios of ferrite and austenite provide superior mechanical and corrosion-resistant properties. Fusion welding of this alloy disrupts the austenite-ferrite ratios, thereby affecting the mechanical and corrosion-resistant properties. According to Floreen and Hayden [24], cleavage fracture in the ferrite phase was hindered by more ductile austenite phase in duplex stainless steel. Rapid cooling during fusion welding produces a change in microstructure (primarily formation of ferrite) causing less ductility and poor corrosion resistance [25]. Austenitic alloy SS 321 is utilized for many purposes mentioned above including nuclear facilities. As it is stabilized, it provides excellent intergranular corrosion-resistance when exposed to high temperature. This alloy is stabilized with titanium to prevent formation of chromium carbide during fusion welding. Still fusion welding causes segregation, formation of

intermetallics, loss of titanium and stress concentration sites. Fusion welded SS 321 is susceptible to knife-line attack if used in highly oxidizing environment [26].

Engine efficiency has become a prime issue in the last decades because it leads to causes reduced fuel consumption and engine emissions. Higher efficiency requires higher operating temperatures. The use of single crystal or columnar-grained blades permits turbine engine operation at higher temperatures and increases the creep resistance significantly [27-30]. For example, single crystal blades withstand up to 50°C higher temperatures compared to their polycrystalline counterparts [31]. This is due to the lesser amount of grain boundary strengthening elements which are known to be responsible for reducing creep strength at high temperatures. However, the casting of single crystals is a very challenging process. The yield of this process is comparatively low and gets lower as the blade size increases. A fabricating process for larger single crystal blades by joining smaller parts might overcome this size limitation. To combat both problems discussed above, solid/liquid phase diffusion bonding is considered a preferred joining method.

Nickel-based Alloys

Nickel-based superalloys are often used in hot-sections of aero-engines and land-based gas turbines. These alloys typically are used in turbine disk, axle, blade, guide blade, shell, tooling and liquid rocket components involving cryogenic temperatures [32-34]. To improve the efficiency, the operating temperature of power generation turbines and jet engines is being increasing continuously. At the same time, the complexity of the engine parts is also increasing. Although nickel-based superalloys provide superior strength, stress rupture, creep resistance, fatigue strength, oxidation and corrosion resistance at

high service temperatures, they suffer various types of damages such as hot corrosion, oxidation, sulphidation, erosion and thermal fatigue cracking. On the other hand, economical manufacturing requires the ability of superalloys components to be welded. Interests in repairing damaged superalloy components is increasing as the price of these alloys is increasing.

Weldability of nickel-based superalloys largely depends on the content of aluminum and titanium. Precipitation-hardened superalloys are prone to microfissuring during fusion welding and post-weld treatment [35]. In addition, non-equilibrium phase transformation and microsegregation occur during rapid solidification of the fusion zone which, in turn, affect the joint performance [36]. To eliminate these problems TLP bonding is considered as a preferred bonding process.

TLP bonding has been developed for low weldability alloys using commercially available low melting temperature interlayers. In the current work, commercially pure titanium (cp-Ti, grade 2), iron (cp-Fe) and nickel (cp-Ni) were used as the initial phase of the research project. These simple bond geometries were used to model the concentration profiles of diffusing species using ThermoCalc/DICTRA software. In the next phase, industrially important alloys such as Ti-6Al-4V, austenitic stainless steel (SS 321) and inconel 718 and were used. Specific focus was given to bonding temperature, bonding time, interlayer materials, interlayer thicknesses, polishing level of the faying surface, microstructure and tensile strength at room temperature. The interlayer materials have been selected depending on the metallurgy of the system and commercial availability. Joint microstructures and strengths were tailored by optimizing bonding conditions such as temperature, time and bonding environment.

CHAPTER II

DIFFUSION BONDING OF COMMERCIAL PURE ALLOYS

Specimen Fabrication

Ti Joints

Cylindrical grade 2 Ti rods (Online Metals) 6.35 mm in diameter and ~8 mm in length were used for diffusion bonding and subsequent microstructural examination. The samples were polished to a 600 grit finish and the surfaces were cleaned in an ultrasonic bath using isopropyl alcohol and stored in alcohol before bonding. The samples for tensile testing had a gauge length of 59 ± 0.5 mm and a diameter of 9.0 ± 0.1 mm in the gauge section. The bonding surface of each sample was polished to a 120 grit finish before bonding. The diffusion bonding was done with commercially pure copper

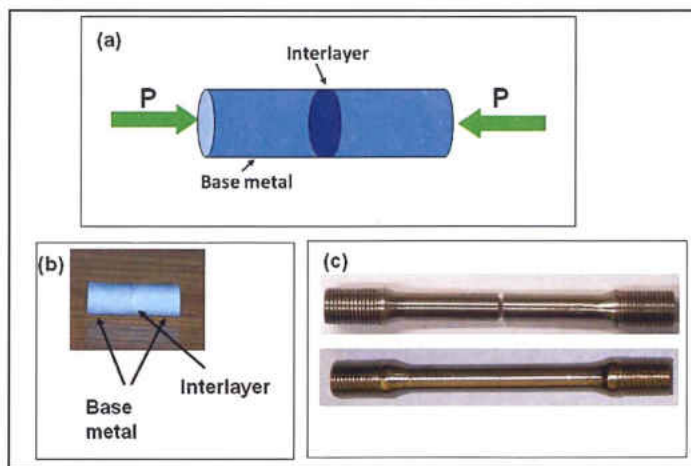


Figure 1. a) Schematic representation of diffusion bond geometry, b) diffusion bonded microstructure sample, and c) tensile specimen (top – before bonding, bottom – after bonding). (99.999% pure, Alfa Aesar, USA), or silver (99.998% pure, Alfa Aesar, USA)

interlayers and without any interlayers. The thickness of both interlayers was 100 μm . The samples to be bonded were held in a jig made of Ti (to eliminate the thermal expansion mismatch) under static pressure and placed in a tube furnace. The clamping torques used for microstructure samples and tensile samples were 10 in-lb and 35 in-lb, respectively. Schematics of the diffusion bond geometry and diffusion bonded samples are shown in Fig. 1. The heating chamber was repeatedly evacuated and filled with argon gas 10 times to make it oxygen-free and then filled with argon gas to have an inert environment for bonding. An oxygen trap was used in the line of argon flow into the heating furnace. Ti joints with Ag interlayers were bonded at 1030°C for 10-30 h and with Cu interlayers were bonded at 900-1100°C for 10 h. These joining temperatures were chosen based on the melting temperature of the interlayer and interlayer-base alloy phase diagrams. The heating rate or cooling rate applied was 4°C/min. Ti bonds without any interlayers were bonded at 980-1030°C for 10-30h. Metallographic samples bonded metals were mounted in epoxy resin. A longitudinal section of each bonded sample was polished down and prepared for microstructural observation.

Fe Joints

For diffusion bonding of cp-Fe, similar procedures were followed as for cp-Ti. Interlayers used were Al, Cu, Au-20Sn and Au-2Ge. Faying surfaces were polished to a 1200 grit finish. The thickness of interlayers varied from 25 μm 100 μm . Based on interlayer melting temperature and interlayer-base alloy phase diagrams, bonding temperatures varied from 600-1100°C for 1-30 h depending on the interlayer material. The jig used was made of Kovar (to minimize the thermal expansion mismatch) which is a high temperature resistant-alloy. The applied clamping torque was 10 in-lb and 35 in-lb for

microstructure samples and tensile samples, respectively. Metallographic samples were mounted in epoxy resin before polishing. Optical micrographs were taken using a computer integrated metallurgical optical microscope. The samples for optical images were etched using 5% Nital.

Ni joints

For diffusion bonding of cp-Ni, Al, Cu, Au-1.5Al, Au-20Sn and Au-12Ge interlayer were used. Bonding surfaces were polished to a 1200 grit finish before bonding. Bonding was done in a Kovar jig with 10 in-lb and 35 in-lb clamping torque for microstructure samples and tensile samples, respectively. The interlayer thicknesses varied from 25 μm to 100 μm . Depending on the melting temperature of interlayers and binary phase diagrams between interlayer and base alloy, the bonding temperatures and times used were 600-1100°C and 1-30 h, respectively.

Microstructural Characterization

Scanning electron microscopy (SEM) observations of bonded samples were carried out using a Hitachi S-3400N scanning electron microscope (SEM) and the compositions and different phases in the bonded zone were analyzed by energy dispersive spectrometry (EDS).

Mechanical Testing

To determine the mechanical properties of the bonded specimen, uniaxial tensile tests were performed using a screw-driven AG-IS 50 kN universal testing machine (Shimadzu) with a crosshead speed of 1 mm/min. Cylindrical tensile specimens were prepared according to the ASTM standard E 8M-99. An average of three samples was taken for

each tensile strength reported.

Results and Discussion

Ti-Ti Bonding

Microstructures

Fig. 2 shows the SEM images of diffusion bonded titanium (Ag interlayer) at 1030°C for 10 h. The bond centerline consisted of AgTi matrix with small particles (submicron to $\sim 2.5 \mu\text{m}$) of AgTi₂ (intermetallic, Fig. 2(a)). A eutectic mixture of α -Ti and AgTi₂ formed just outside to this central region. Closer to the base material, a mixture of Ag-Ti intermetallics and a solid solution of Ti and Ag was found (Fig. 2(b)). The bond region farthest from the centerline consisted of only a solid solution of Ti and Ag (Fig. 2(c)). As the bonding time increased to 30 h at 1030°C, the same microstructures appeared in the bond region but the dimensions of each region increased somewhat. Also, some regions of Ti-Ag solid solution were found in the AgTi matrix at the bond centerline (Fig. 3).

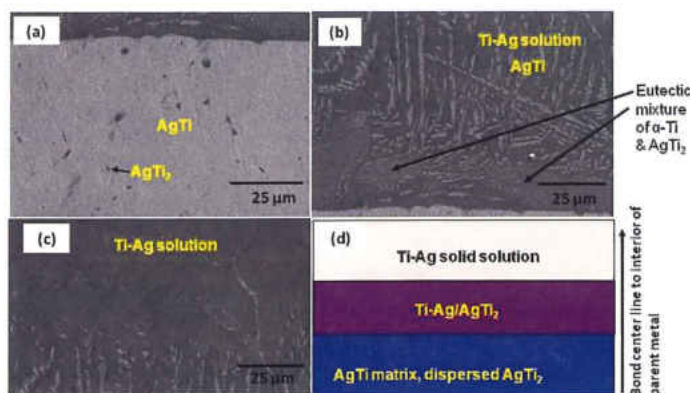


Figure 2. SEM images of diffusion bonded Ti using Ag interlayer at 1030°C for 10 h, a) bond center line, b) $\sim 80 \mu\text{m}$ away from the bond centerline, c) $\sim 160 \mu\text{m}$ away from the bond centerline and d) the schematic representation of different regions from the bond centerline to the interior of base material.

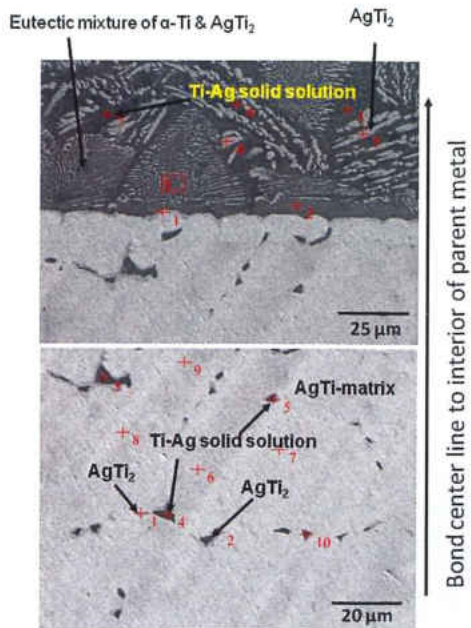


Figure 3. SEM images of diffusion bonded titanium using Ag interlayer at 1030°C for 30 h.

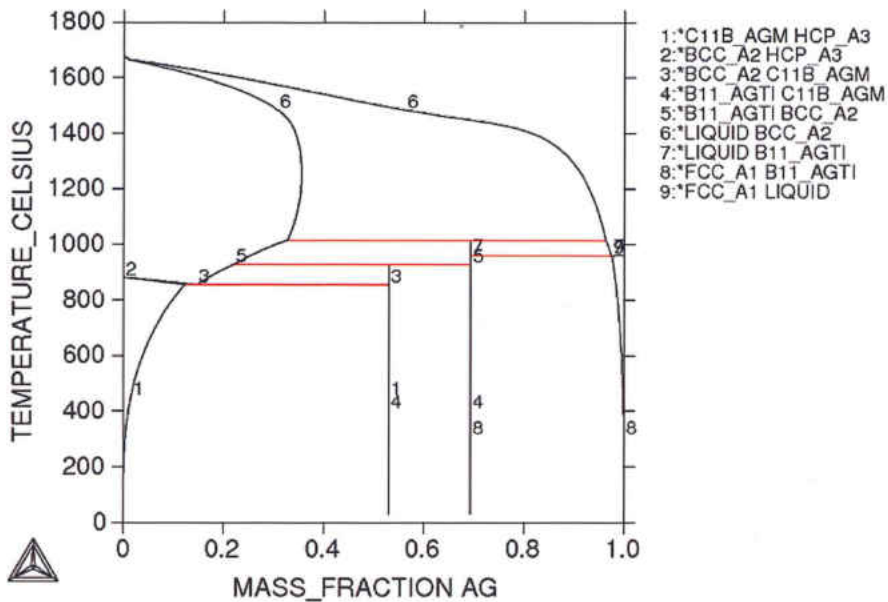


Figure 4. Ti-Ag phase diagram generated in ThermoCalc version TCW5.

According to the equilibrium phase diagram of Ti-Ag (Figure 4), Ti can dissolve more than 29.2 wt% Ag at 1030°C. But as the temperature decreases, the solubility of Ag into

Ti also decreases and at room temperature it is about 1 wt%. The goal was to obtain Ti-Ag solid solution or at least to reduce the intermetallics in the bond centerline because the intermetallics are brittle and thereby reduce the joint strength. However, a continuous layer of AgTi intermetallics was found under all conditions.

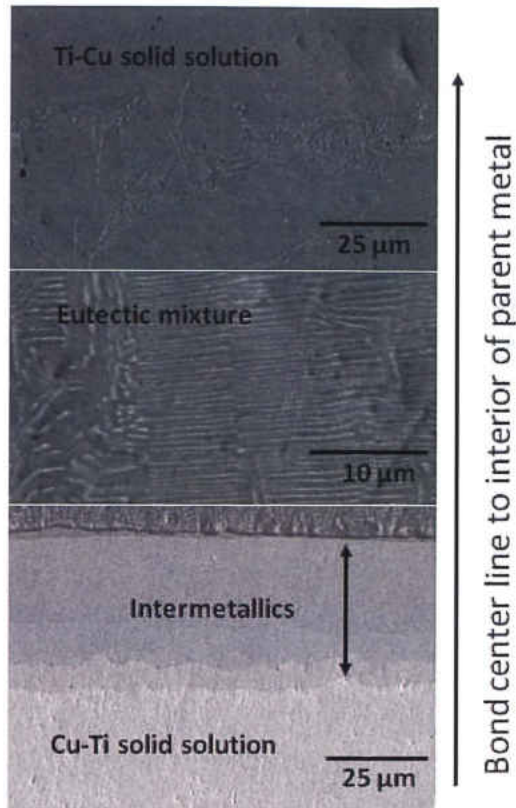


Figure 5. SEM images of diffusion bonded titanium using Cu interlayer at 900°C for 10 h.

Although Ag and Cu both form intermetallics with Ti, the microstructure of the bonded zone was different when Cu was used as an interlayer than when an interlayer of Ag was used. At 900°C for 10 h, the bonding zone consisted of a region of Cu-Ti solid solution, a region of different intermetallics (TiCu_4 , Ti_2Cu_3 , TiCu), a region of eutectic mixture of Ti and intermetallics and a region of Ti-Cu solution (Fig. 5). The composition of Cu was

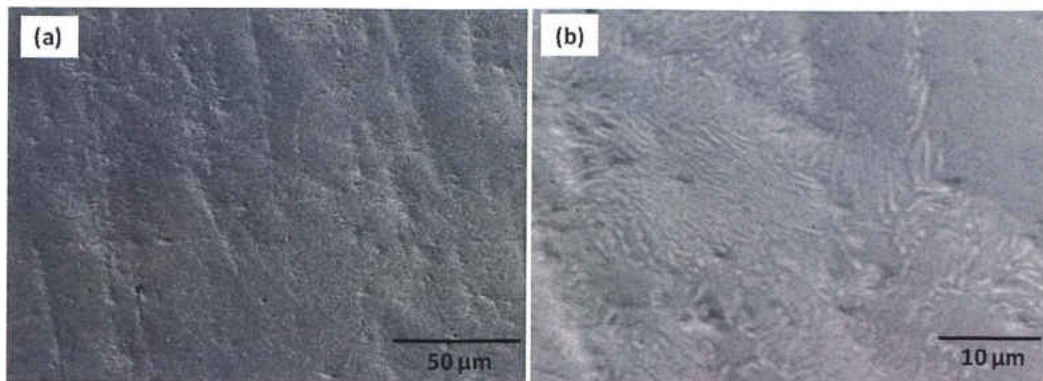


Figure 6. SEM images of diffusion bonded titanium using Cu interlayer a) at 1000°C for 10 h and b) enlarged image of (a).

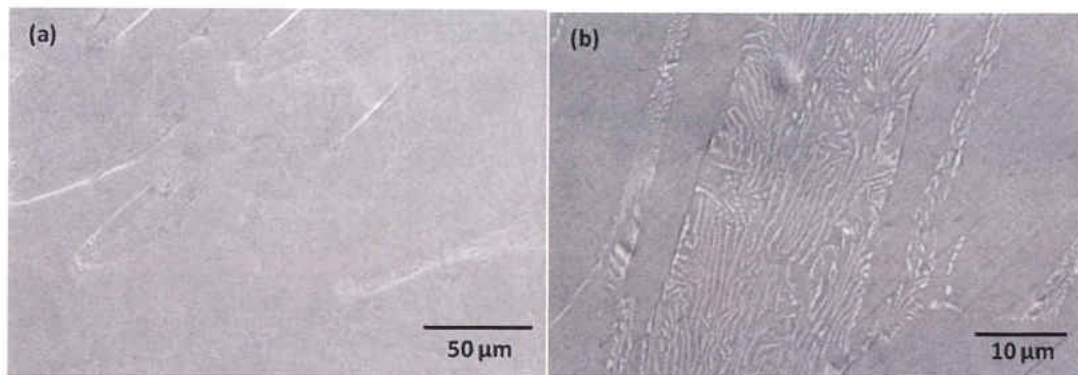


Figure 7. SEM images of diffusion bonded titanium using Cu interlayer a) at 1020°C for 10 h and b) enlarged image of (a).

discontinuous in the intermetallic region depending on the composition of intermetallics. As the bonding temperature increased to 1000°C, the continuous region of different intermetallics disappeared from the bond centerline. The centerline consisted of a eutectic mixture of Ti and Cu. A cross-section of the joint centerline is shown in Fig. 6. Similar microstructures were obtained at the centerline at 1020°C for 10 h (Fig. 7). Although the melting point of Cu is 1085°C, no residual Cu was found in the bond region at 1000°C or above. The reason could be the formation of β -Ti above 880°C which dissolves the

maximum ~17 wt. % of Cu at 1000°C (refer to the Ti-Cu phase diagram, Figure 8).

However, at 1100°C for 10 h some pores appeared in the bond region and the pore size increased at higher temperatures. The bond centerline consisted of Ti-Cu solid solution, eutectic, and some small areas of intermetallics, possibly Ti_3Cu . A cross-section of this joint is shown in Fig. 9.

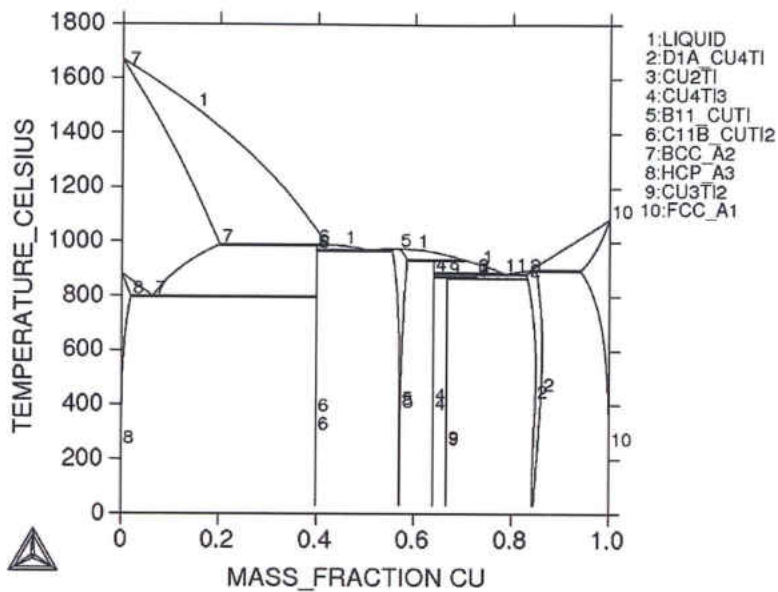


Figure 8. Ti-Cu phase diagram generated in ThermoCalc version TCW5.

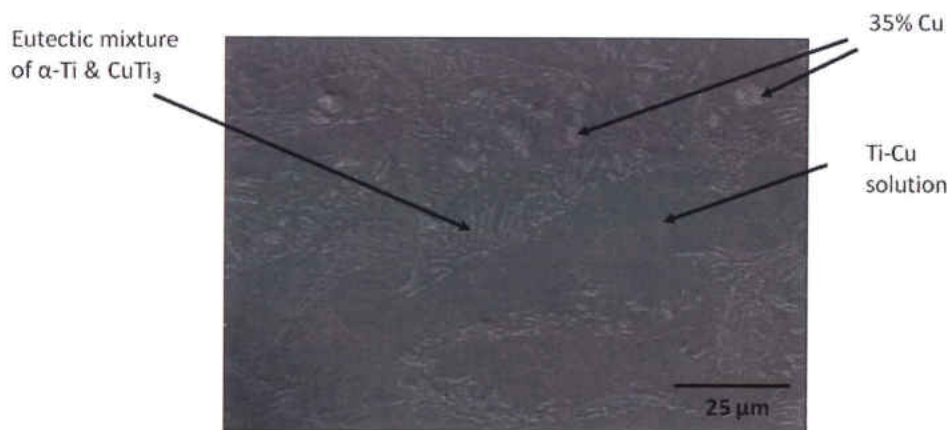


Figure 9. SEM images of diffusion bonded titanium using Cu interlayer at 1100°C for 10 h.

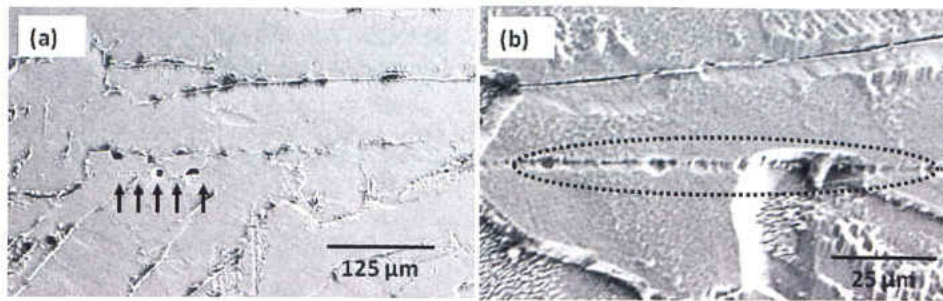


Figure 10. a) SEM images of diffusion bonded titanium without interlayer at 980° C for 20 h (etched with 8% HF and 4% HNO₃), and b) magnified image of (a).

Ti was also diffusion bonded without any interlayers. Fig. 10 shows the SEM images of diffusion bonded titanium without interlayer at 980°C for 20 h (etched with 8% HF and 4% HNO₃). The bond line was not visible under SEM until etched and it was not continuous; some regions were completely bonded while voids were present elsewhere. The bonding temperature (980°C) was ~65% of the melting point of Ti. The joint centerline microstructures were summarized in Table 1.

Table 1. Summary of the microstructure of TLP bonded Ti using Ag and Cu interlayer (100 μm).

Interlayer	Interlayer Thickness (μm)	Bonding Temp. (°C)	Bonding Time	Bond Centerline Microstructure
Ag	100	1030	10	AgTi matrix with submicron particles of AgTi ₂
Ag	100	1030	30	AgTi matrix with submicron particles of AgTi ₂
Cu	100	900	10	A region of Cu-Ti solid solution, a region of different intermetallics (TiCu ₄ , Ti ₂ Cu ₃ , TiCu), a region of eutectic mixture of Ti and intermetallics and a region of Ti-Cu solution
Cu	100	1000	10	A eutectic mixture of Ti and Cu and a solid solution of Ti and Cu
Cu	100	1020	10	A eutectic mixture of Ti and Cu and a solid solution of Ti and Cu
Cu	100	1100	10	Ti-Cu solid solution, eutectic mixture of Ti and CuTi ₃ , and some small areas of intermetallics, possibly Ti ₃ Cu

Mechanical Properties

Table 2. Ultimate tensile strengths of diffusion bonded Ti samples with Ag and Cu interlayers and without any interlayer.

Interlayer	Temperature (°C)	Time (h)	UTS (MPa)
Commercially pure Ti (Grade 2)			511±3
Ag	1030	10	72±17
Ag	1030	30	160±25
Cu	980	10	460±14
Cu	1000	10	468±10
Cu	1030	10	502±7
None	980	10	296±9
None	980	20	380±11
None	980	30	352±8
None	1030	10	343±5
None	1030	20	382±13
None	1030	30	358±8

To check the mechanical properties of the bonded samples, uniaxial tension tests were performed. Table 2 shows the tensile properties of the bonded samples with Ag and Cu interlayers and without any interlayer. The strengths of the samples bonded using Ag interlayers were very low due to the formation of a continuous layer of fragile intermetallics in the bonded region. The maximum strength achieved for this interlayer was 160±25 MPa at 1030°C for 30 h. The maximum strength increased to 502±7 MPa when Cu was used as an interlayer at 1030°C for 10h which is ~98% of the base metal strength (511 MPa). This might be due to the absence of a continuous region of intermetallics as discussed earlier. The ultimate tensile strength was also measured for bonding at 980°C ($0.65T_m$, T_m is the melting point of Ti) and 1030°C ($0.67T_m$) for 10-30 h without any interlayer. The strength increased with temperature and 10-20 h bonding

time, but decreased at 30h bonding time. The maximum ultimate tensile strength of 382 MPa was achieved at 1030°C for 20h. Figure 11 shows the SEM images of fracture surfaces of pure Ti, diffusion bonded Ti using Ag and Cu interlayer. The fracture surface of the cp-Ti showed ductile fracture while the fracture surface of bonded cp-Ti using Ag interlayer showed brittle fracture. On the other hand, bonded cp-Ti using Cu interlayer showed a mixed mode fracture with significant ductile regions.

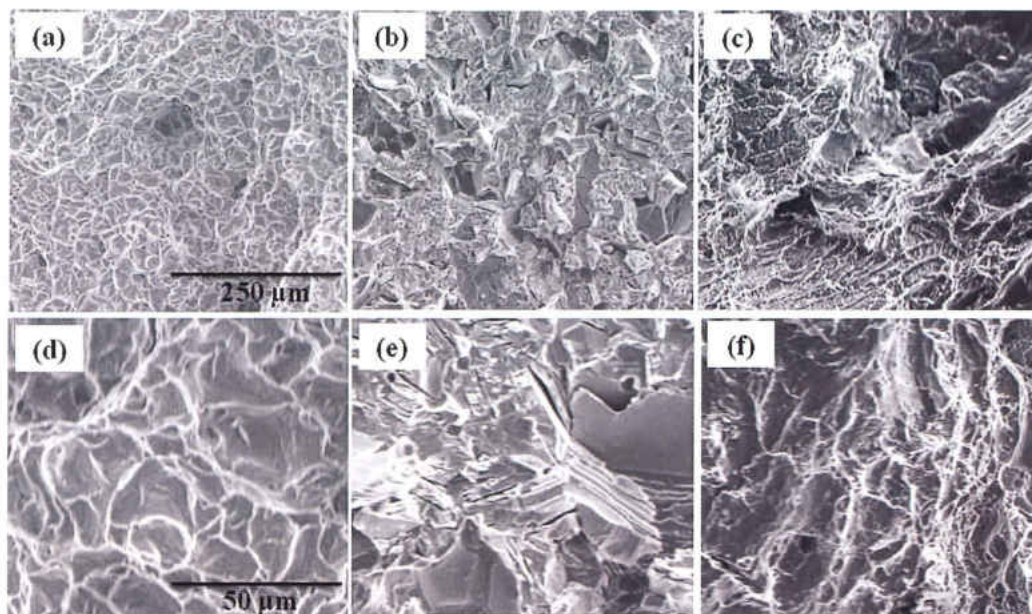


Figure 11. SEM images of fracture surfaces of (a) pure Ti, (b) diffusion bonded Ti using Ag at 1030°C for 10h , (c) diffusion bonded Ti using Cu interlayer at 1030°C for 10 h; (d), (e) and (f) are magnified image of (a), (b) and (c), respectively .



Figure 12. Fracture surface of tensile specimen, faying surfaces were polished by hand before bonding.

In addition to bonding time and interlayer composition, both the flatness of the bonding surfaces and surface roughness were found to influence the strength of the diffusion bonded joints. Initially, tensile specimens were polished by hand on a polishing wheel to a 600 grit finish. However, the bonding surface of these specimens was found to be somewhat curved, especially near the edges, and the outer surfaces did not bond well as shown in Fig. 12. The effect was not as pronounced on the smaller samples for microscopic analysis. Fig. 13 shows the SEM images of fracture surface of Ti-Ti bonded at 980°C for 10h; the bonding surface was polished by a) hand to 600 grit and b) grinding at 980°C for 10h; the bonding surface was polished by a) hand to 600 grit and b) grinding

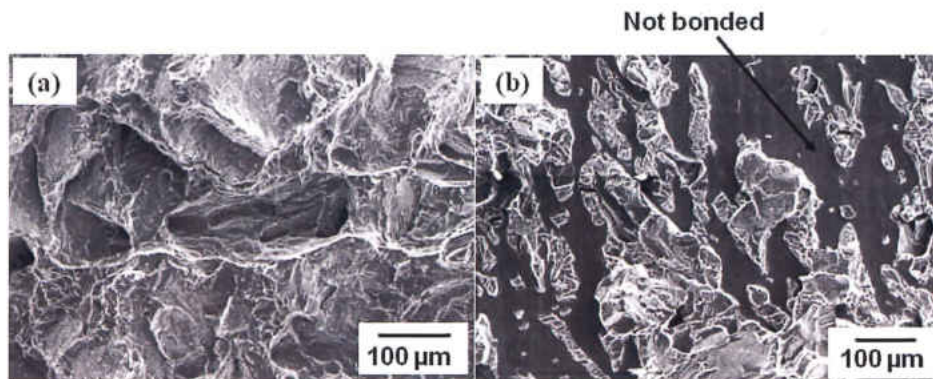


Figure 13. SEM images of fracture surface of Ti-Ti bonded at 980°C for 10h, the bonding surface was polished by a) hand (grit# 600) and b) wheel (grit#120) before bonding.

wheel to 120 grit before bonding. Due to the coarser grit, the wheel-polished specimen shows many unbonded regions compared to specimen polished by hand. However, the wheel-polished specimen surface is much flatter, resulting in a larger overall area of contact between specimen faces. This leads to higher joint strengths for the wheel-polished specimens. Only one grinding wheel grit was available for the current work. Additional study is needed to quantify the effect of surface roughness on the final joint strength. It is to be noted that during calculation of tensile strengths the nominal

diameters of the specimens were used (*i.e.* no correction was made for any unbonded area around the periphery).

Conclusions

This study investigated the diffusion bonding of commercially pure Ti using Ag, Cu and without any interlayer. The formation of brittle intermetallics could not be avoided for an Ag interlayer even for longer periods of bonding time. Hence, the strength of the joints was very low. On the other hand, formation of a continuous band of intermetallics was avoided using a Cu interlayer. The maximum strength obtained was 502 MPa using Cu interlayer and the joints reached ~98% of the strength of the base metal. The strength reached ~75% of the parent metal when no interlayer was used. Further investigations are necessary to check the effects of surface finish and surface flatness on the tensile strengths of the diffusion bonded Ti.

Fe-Fe Bonding

Microstructures

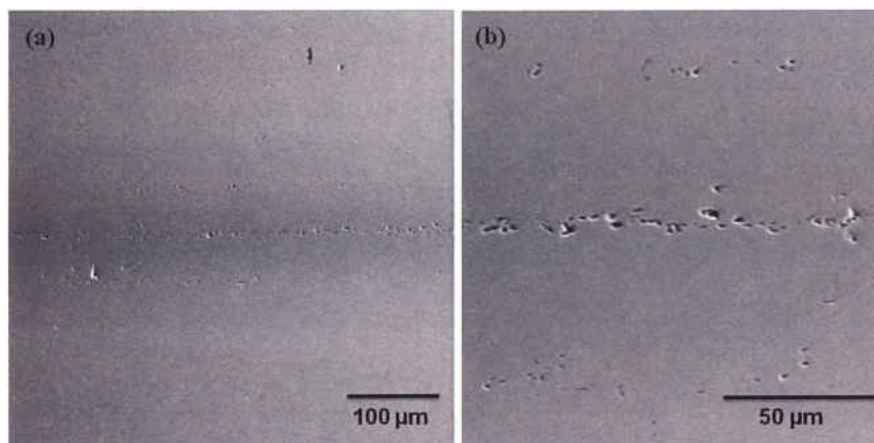


Figure 14. (a) SEM images of diffusion bonded Fe using Al interlayer (0.1 mm) at 900°C for 10 h (surface finish 600 μm) and (b) enlarged image of (a).

Figure 14 shows SEM images of diffusion bonded cp-Fe using Al interlayer (100 μm) at 900°C for 10 h and (b) enlarged image of (a). SEM images indicated that porous microstructures appeared along the bond centerline. The bond centerline had a

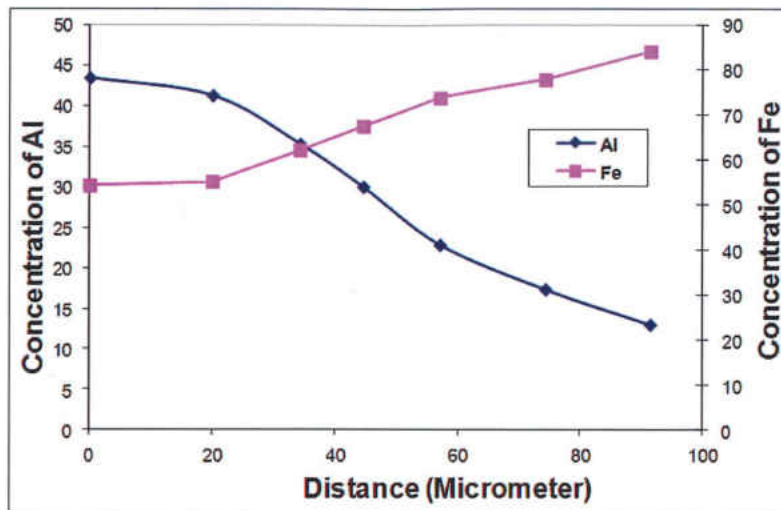


Figure 15. Concentration profiles of Al and Fe in diffusion bonded Fe using Al interlayer (0.1 mm) at 900°C for 10 h.

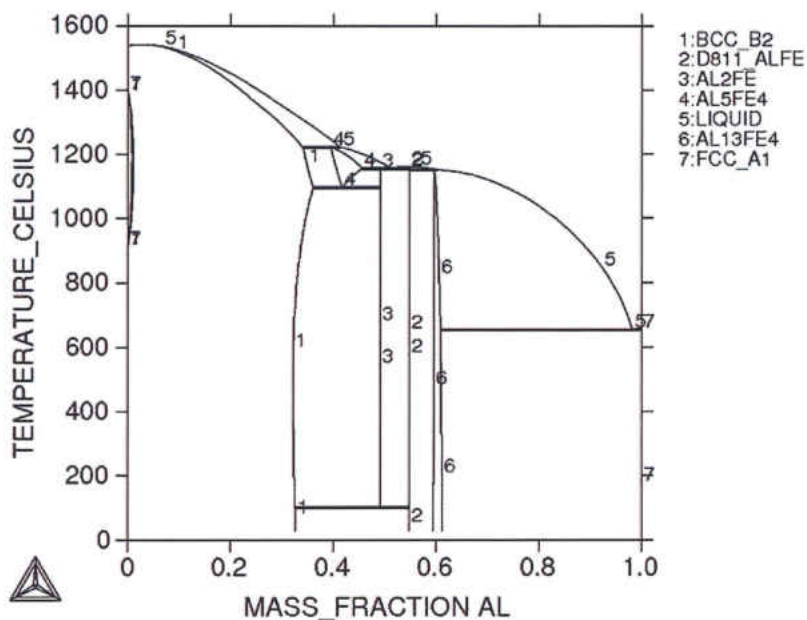


Figure 16. Fe-Al phase diagram generated in ThermoCalc version TCW5.

composition of 43.4 wt. % Al and 54.3 wt. % Fe. The percentage of Al gradually decreased into the interior of the base metal. Figure 15 shows the composition profiles of

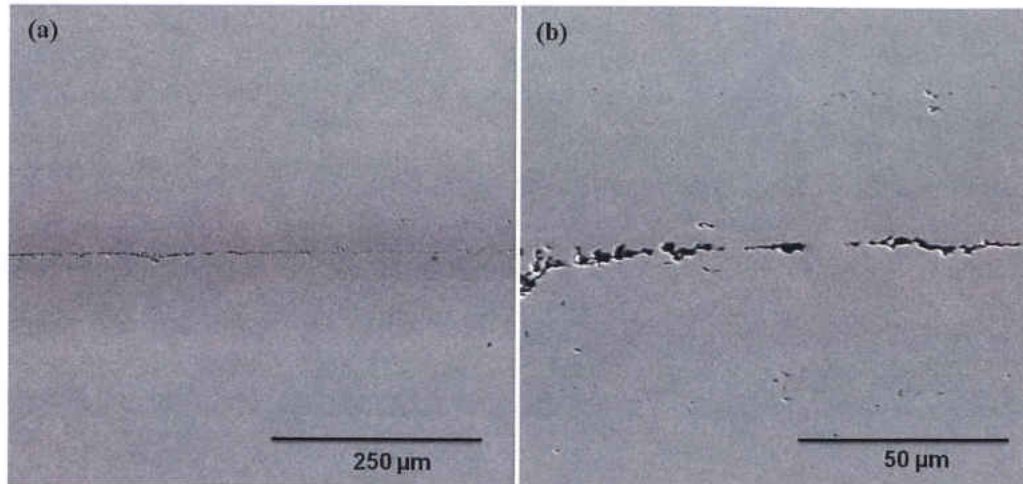


Figure 17. Diffusion bonded cp-Fe at 900°C for 20 h using Al interlayer (100 μm).

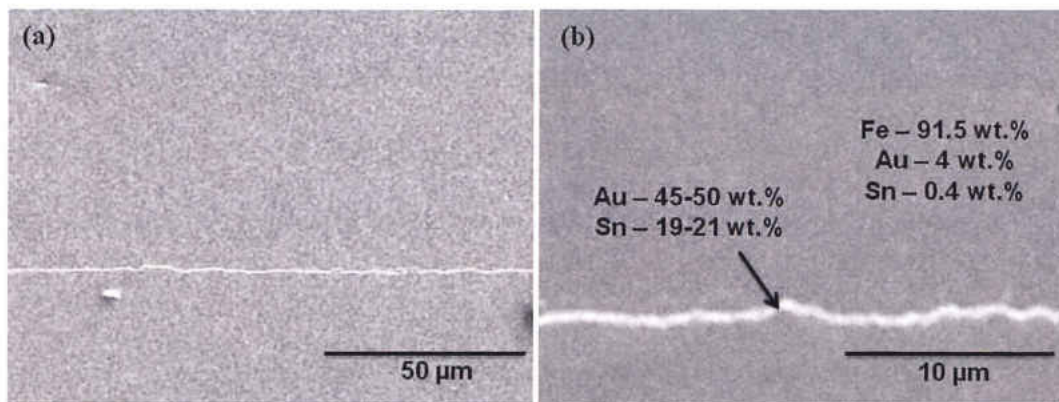


Figure 18. SEM images of diffusion bonded Fe using Au-20Sn interlayer (100 μm) at 600°C for 10 h.

Al and Fe from the bond centerline to the interior of base metal. The compositions of intermetallics between Al and Fe range from 37.7 wt. % to 61.1 wt. % Al (Figure 16). Although the composition of the bond centerline falls within this range, a continuous thickness of intermetallics (as seen in Ti joint using Ag) was absent. The bonding time was then increased to 20 h. Figure 17 shows diffusion bonded cp-Fe at 900°C for 20 h

using Al interlayer (100 μm). The composition of bond centerline was 30.5 wt. % Al which decreases with increasing distance from the bondline. Although intermetallic formation was avoided, the porous microstructure appeared in the bond centerline as seen in the previous bonding conditions.

Figure 18 shows SEM images of diffusion bonded Fe using Au-20Sn eutectic interlayer (100 μm thick) (a) at 600°C for 10h, and (b) magnified image of (a). After holding at 600°C for 10 h, almost all interlayer material has been diffused into the base metal. The thickness of the residual interlayer was less than a micrometer with a composition of 40-45 wt.% Au and 19-21 wt.% Sn. The joint area away from the residual interlayer contains a maximum of 4 wt.% Au and 0.2 wt.% Sn and decreased gradually. No intermetallics were found in the joint area. After increasing the bonding temperature to 650°C, the residual interlayer disappeared. Figure 19 shows SEM image of diffusion bonded Fe using Au-20Sn eutectic alloy interlayer (100 μm) at 650°C for 10 h. Fast diffusion occurred at such a low temperature because the Au-20Sn eutectic alloy has a melting temperature of 278°C (Figure 20).

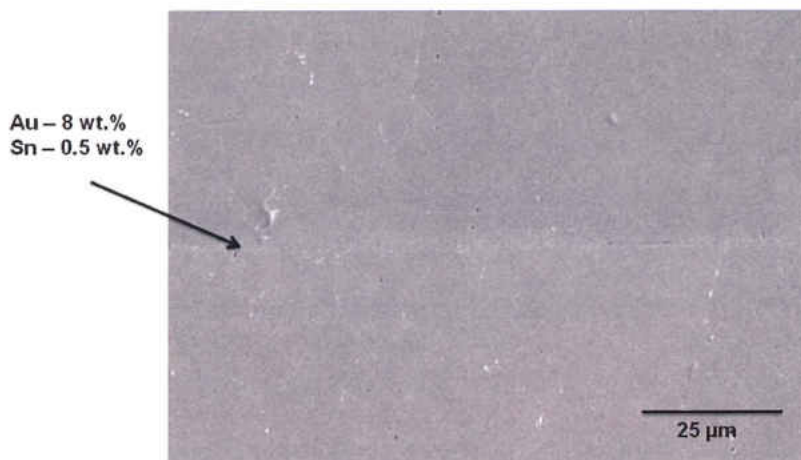


Figure 19. SEM image of diffusion bonded Fe using Au-20Sn eutectic alloy interlayer (100 μm) at 650°C for 10 h.

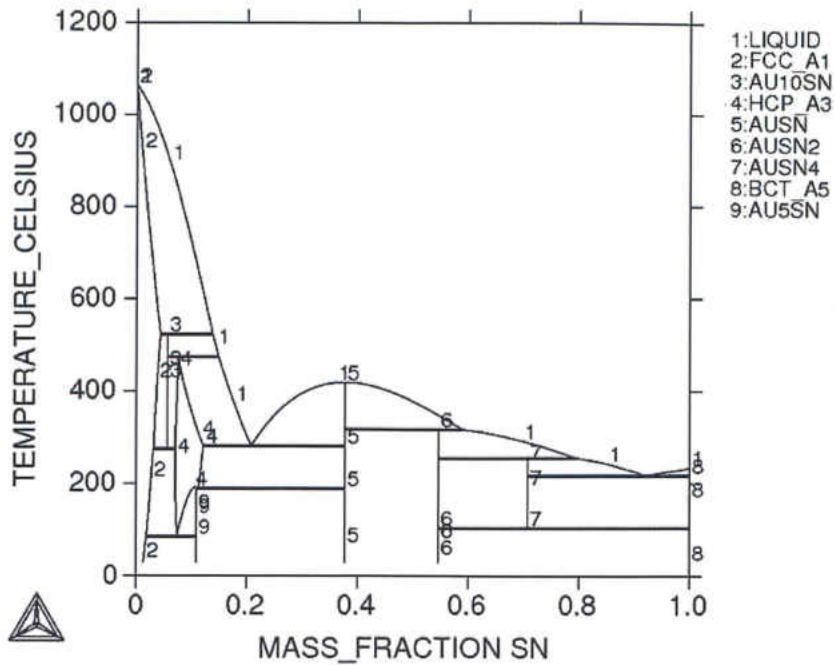


Figure 20. Au-Sn phase diagram generated in ThermoCalc version TCW5.

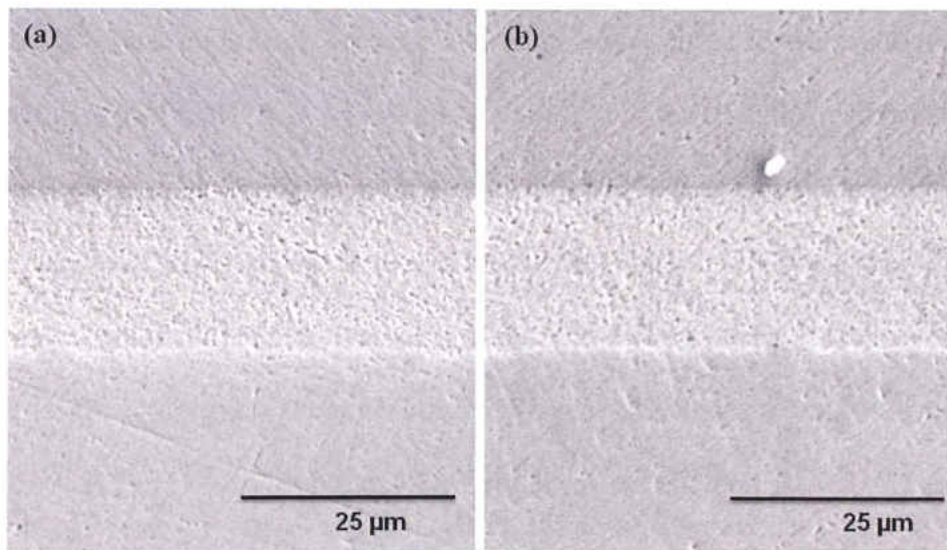


Figure 21. SEM images of diffusion bonded Fe using Cu interlayer (25 μm) at (a) 1070°C for 10 h and (b) 1085°C for 30 h.

Figure 21 shows SEM images of diffusion bonded Fe using a Cu interlayer (25 μm) at (a) 1070°C for 10 h and (b) 1085°C for 30 h. As can be seen from the pictures, the interlayer

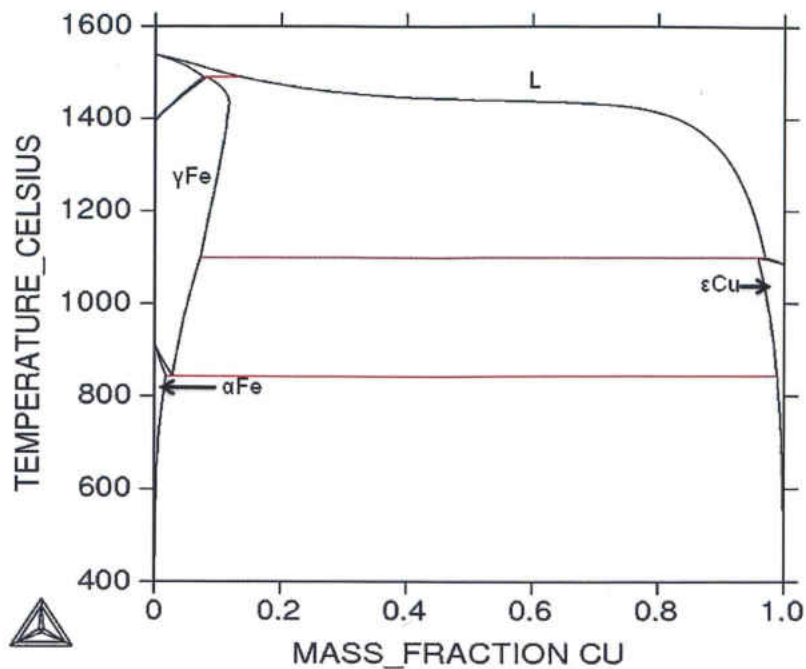


Figure 22. Fe-Cu phase diagram generated in ThermoCalc version TCW5.

did not diffuse completely into the base metal under either set of conditions. The residual interlayer had a thickness of $\sim 19 \mu\text{m}$. After 1070°C for 10 h, the residual interlayer contained 2.7–3.2 wt. % Fe. Fe at the interlayer/base metal interface contained ~ 7.6 wt % Cu with the Cu content gradually decreasing into the interior of the base metal. No pores were observed in the joint area at the bonding conditions mentioned above. According to the Fe-Cu equilibrium diagram (Figure 18), γ -Fe dissolves 6.5 wt. % Cu and Cu dissolves 3.5 wt. % Fe (Cu solid solution with Fe is known as ϵ -Cu) at 1070°C . There are discrepancies between the observed compositions and the compositions for solubility limits. This might be due to the fact that EDS measurements are semi-quantitative in nature. Nevertheless, it can be said that the compositions of Fe and residual Cu at the joint interface indicated that Fe and Cu formed solid solutions in the base metal and in the residual Cu, respectively. The bonding temperature was then increased to 1085°C , which

is very close to the melting temperature of pure Cu (1084.85°C). At 1085°C for 30 h, the microstructure of the bonded area was similar to that for the first conditions. The residual interlayer was ~19 µm and contained 3.8-6.8 wt. % Fe. As Cu starts dissolving Fe, its melting temperature increases which, in turn, slows the diffusion process.

Figure 23 shows SEM image of diffusion bonded Fe using Cu interlayer (25 µm) at 1090°C for 10 h. The interdiffusion of Fe and Cu was not enhanced appreciably over the conditions in Figure 21. The thickness of the residual interlayer was ~19 µm. There were no pores at the interface between base metal and residual interlayer. The residual interlayer contained 3.9-5.2 wt. % Fe. The composition at the interface in the base metal

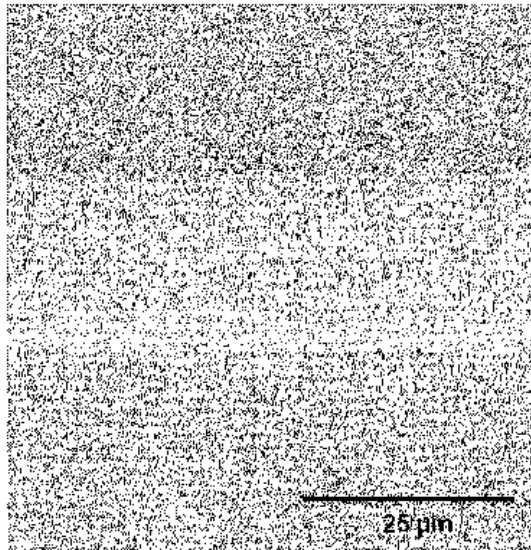


Figure 23. SEM image of diffusion bonded Fe using Cu interlayer (25 µm) at 1090°C for 10 h.

side was 9.5 wt. % Cu with the Cu content gradually decreasing into the base metal. The compositions of the interface on both the base metal and interlayer sides were slightly more than the solubility limits. It appeared that the interdiffusion of Fe and Cu in the temperature range 1070°C to 1090°C was limited by their mutual solubilities.

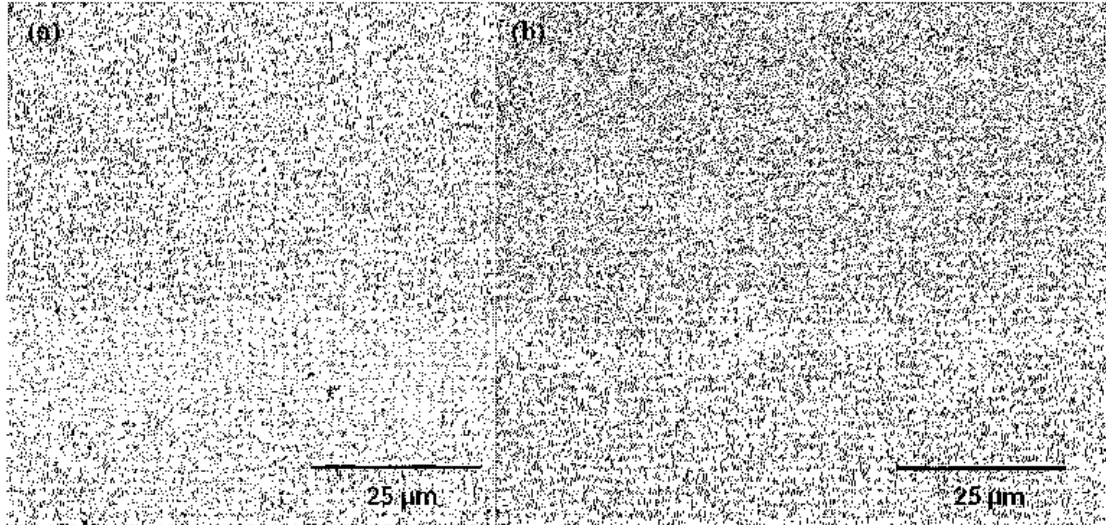


Figure 24. SEM images of diffusion bonded Fe using Cu interlayer (25 μm) at 1100°C for (a) 3 h and (b) 4 h.

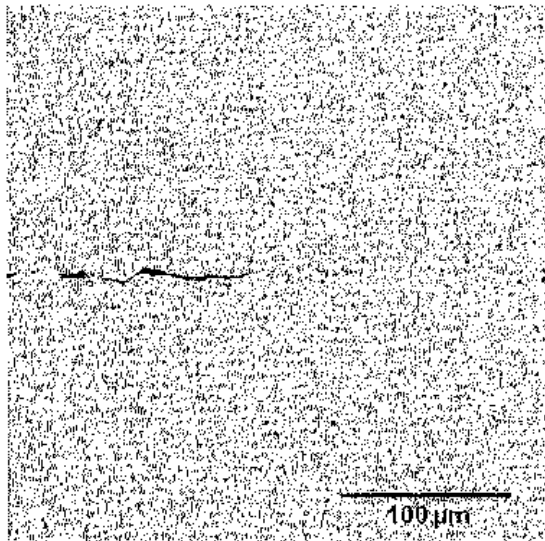


Figure 25. (a) SEM image of diffusion bonded Fe using Cu interlayer (25 μm) at 1100°C for 5 h.

The bonding temperature was increased to 1100°C to enhance the interdiffusion between Fe and Cu. This was $\sim 15^\circ\text{C}$ above the melting point of pure Cu. Figure 24 shows SEM images of diffusion bonded Fe using Cu interlayer (25 μm) at 1100°C for (a) 3 h and (b) 4 h. The residual interlayer was $\sim 13.9 \mu\text{m}$ and 3.3-3.5 μm after 3 h and 4 h bonding

times, respectively. After 4 h bonding time the residual interlayer diffused completely in some areas (not shown in the image) and in some areas it formed a trail of interlayer material, possibly along the grain boundaries. The residual interlayer contained 3.9-5 and ~4.8 wt. % Fe after 3 and 4 h bonding time, respectively. The solubility limit for Cu in γ -Fe is 7.22 wt. % and for Fe in ϵ -Cu is 4.15 wt. % at 1100°C. Figure 25 shows SEM images of diffusion bonded Fe using Cu interlayer (25 μm) at 1100°C for 5 h. After 5 h bonding time, no residual interlayer was found in the joint area. However, a porous microstructure appeared across the joint centerline. The bond centerline contained maximum 7.5 wt. % Cu with Cu content decreasing away from the centerline. The composition of the bond centerline and the base metal near the bond centerline are comparable to the solubility ranges for γ -Fe and ϵ -Cu.

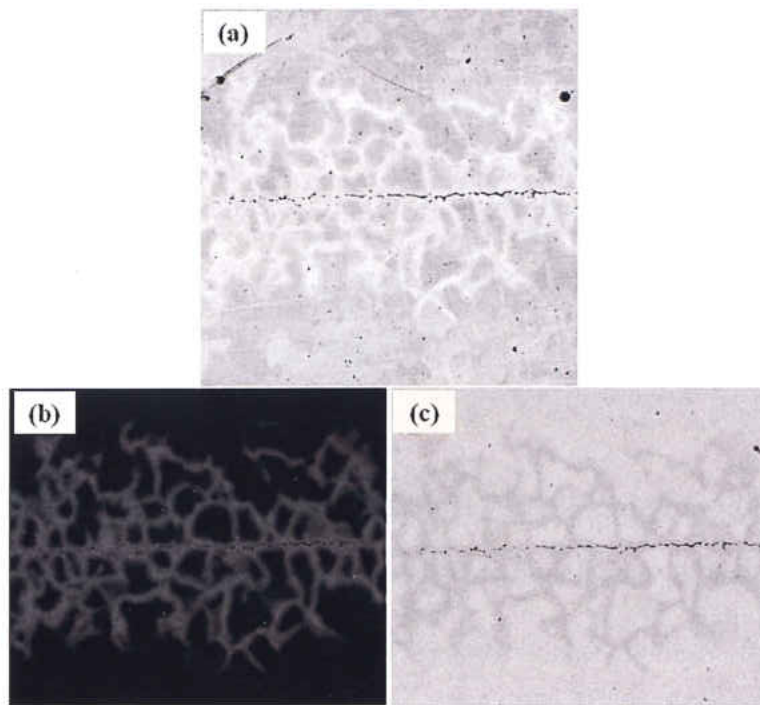


Figure 26. (a) BSE mode image of diffusion bonded Fe using Cu interlayer (25 μm) at 1100°C for 10 h, element mapping of (b) Cu and (c) Fe taken from the joint area.

Figure 26 shows (a) back-scattered electron (BSE) mode image of diffusion bonded Fe using Cu interlayer (25 μm) at 1100°C for 10 h, and element mapping of (b) Cu and (c) Fe taken from the joint area. Cu and Fe were shown with different contrast in the BSE mode image. The element mapping of Cu and Fe indicated that Cu has diffused along the grain boundaries of Fe. The same diffusion pattern of Cu in Fe has been observed at 1070°C. Speich et al. [37] also observed low lattice diffusivity of Cu in γ -Fe and rapid diffusion of Cu along austenite grain boundaries. The porous microstructure obtained was probably due to dominant grain boundary diffusion.

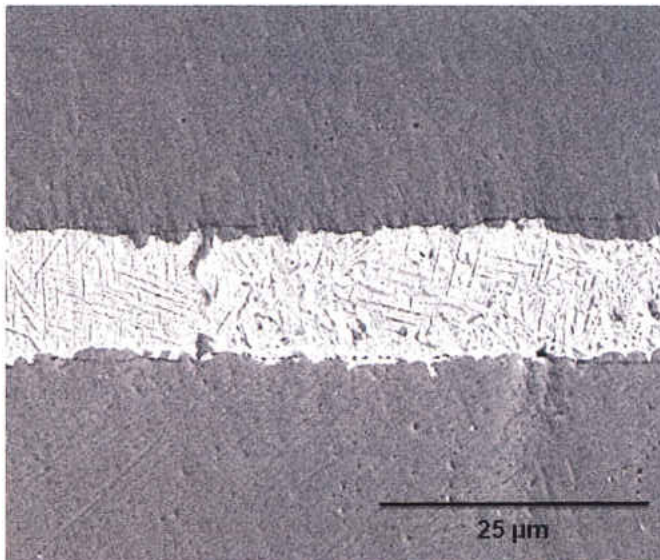


Figure 27. (a) SEM image of diffusion bonded Fe using Au-12Ge interlayer (100 μm) at 900°C for 1 h.

Figure 27 shows SEM images of diffusion bonded Fe using Au-12Ge interlayer (100 μm) at (a) 900°C for 1 h. The thickness of the residual interlayer was \sim 12.6 μm . The composition of the residual interlayer was 15.5-28.9 wt. % Fe, 61-77 wt. % Au and no Ge. The composition of the base metal at the interface was 78-79 wt. % Fe, 11-11.4 wt. % Au and 4.4 wt. % Ge. The amount of Ge and Au decreased gradually away from the

interface. The microstructure of the residual interlayer appeared to be an irregular fingerprint structure. The melting point of Au-12Ge eutectic interlayer is 361°C but it increases as the percentage of Ge decreases. The interlayer did not diffuse completely due to the faster diffusion of Ge in the base metal as no Ge was found in the residual

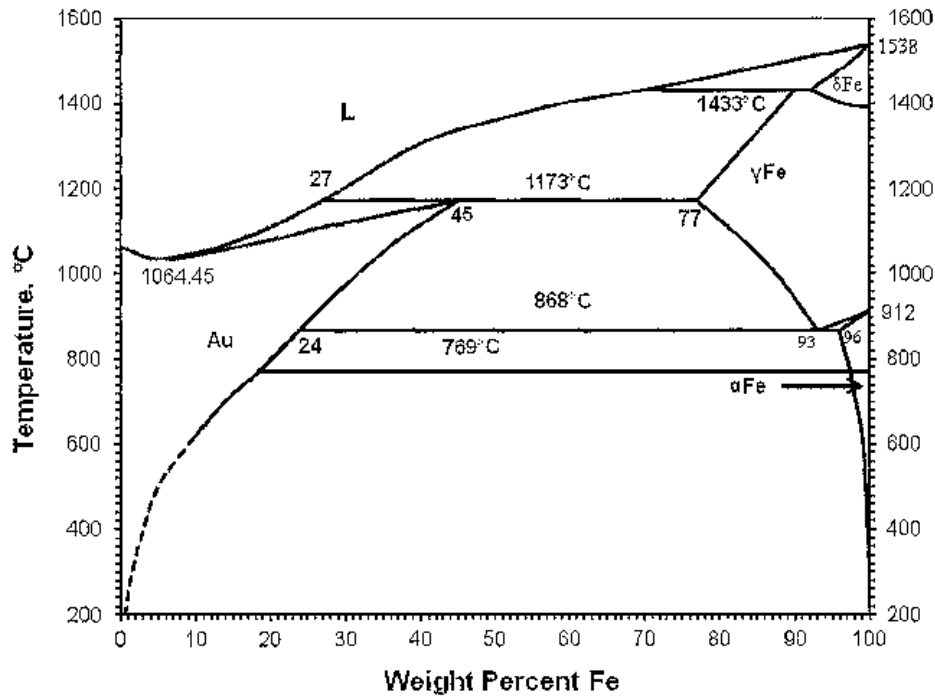


Figure 28. Au-Fe Phase diagram [38].

interlayer. According to the Au-Fe phase diagram (Figure 28), Au can dissolve 26 wt. % Fe at 900°C. However, the percentage of Fe in the residual interlayer was not uniform. The black lines in the residual interlayer contained more Fe than the white area did. Element mapping of Fe was obtained from the residual interlayer. Figure 29 shows element mapping of Fe and Au of diffusion bonded Fe using Au-12Ge interlayer (100 μm) at 900°C for 1 h taken from the bond centerline. The element mapping indicated that the black lines were Fe-rich areas. The evolution of this microstructure can be explained

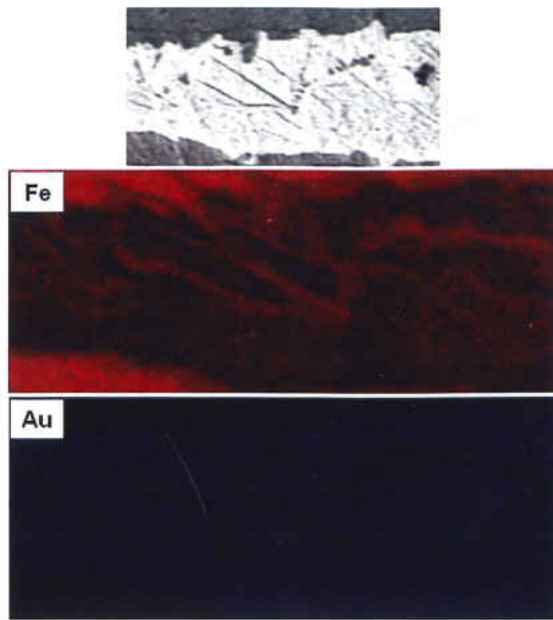


Figure 29. Element mapping of Fe and Au of diffusion bonded Fe using Au-12Ge interlayer (100 μm) at 900°C for 1 h taken from the bond centerline.

by referring to the Au-Fe equilibrium diagram (Figure 28). The solubility of Fe in Au decreases as the temperature decreases. As a result, a solid solution of Fe in Au becomes supersaturated and the excess Fe comes out as another solid solution of Au in Fe ($\alpha\text{-Fe}$).

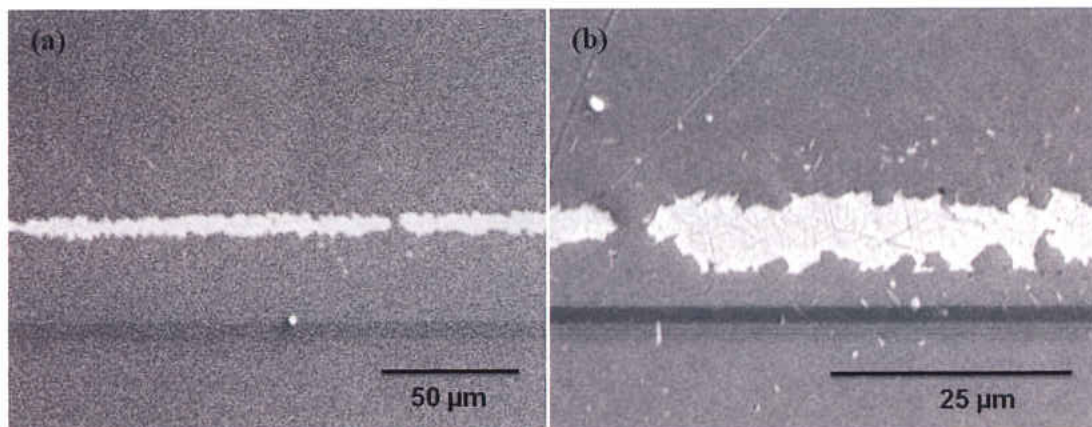


Figure 30. SEM image of diffusion bonded Fe using Au-12Ge interlayer (100 μm) (a) at 900°C for 10 h and (b) enlarged image of (a).

Figure 30 shows SEM images of diffusion bonded Fe using Au-12Ge interlayer (100 μm) (a) at 900°C for 10 h and (b) enlarged image of (a). The interlayer completely diffused into the base metal in few areas. In most areas the interlayer did not diffuse completely and the average thickness of the residual interlayer was $\sim 6.3 \mu\text{m}$. The microstructure of the residual interlayer was similar to that of the previous conditions – irregular fingerprint type. The residual interlayer contained $\sim 18.5 \text{ wt. \% Fe}$, $\sim 75.6 \text{ wt. \% Au}$ and no Ge. Base metal at the interface contained 85 wt. % Fe, 7.6 wt. % Au and 2.1 wt. % Ge. White particles near the interface were formed possibly during the cooling process. EDS analysis confirmed these particles were Au-rich particles. The solubilities of Au in Fe and Fe in Au decrease as the temperature decreases; the solubilities are almost zero at room temperature. During the cooling process, solid solutions of Au in Fe become supersaturated and excess Au comes out of the solution and forms solid solutions of Fe in Au.

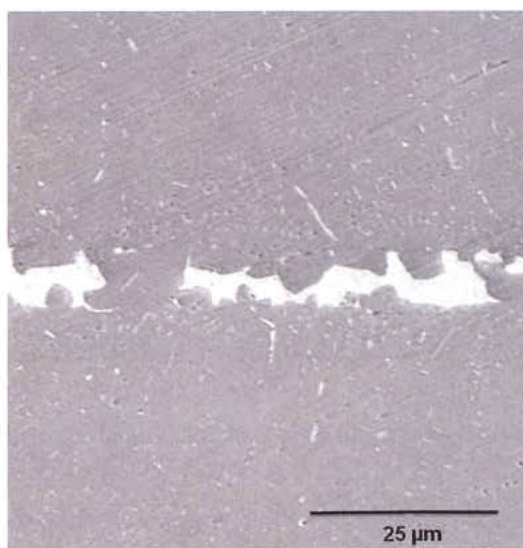


Figure 31. SEM image of diffusion bonded Fe using Au-12Ge interlayer (100 μm) at 920°C for 15 h.

Figure 31 shows a SEM image of diffusion bonded Fe using Au-12Ge interlayer (100 μm) at 920°C for 15 h. At this bonding condition the interlayer completely diffused into the base metal in some areas while it retained in some areas. The thickness of the residual interlayer varied from 1.25 to 3.8 μm . The residual interlayer contained 11.9 wt. % Fe, 78.9 wt. % Au and no Ge. Base metal near the interface contained 73 wt. % Fe, 14.6 wt. % Au and 3 wt. % Ge. No residual pores were observed in the bonded area. More Au-rich particles formed in the base metal near the interface than formed in the previous conditions. Ge forms several intermetallics with Fe according to the Fe-Ge phase diagram. However, no intermetallics were found at any bonding conditions. The percentages of Ge were within the solubility range throughout the joint (4.4 wt. % Ge in $\gamma\text{-Fe}$).

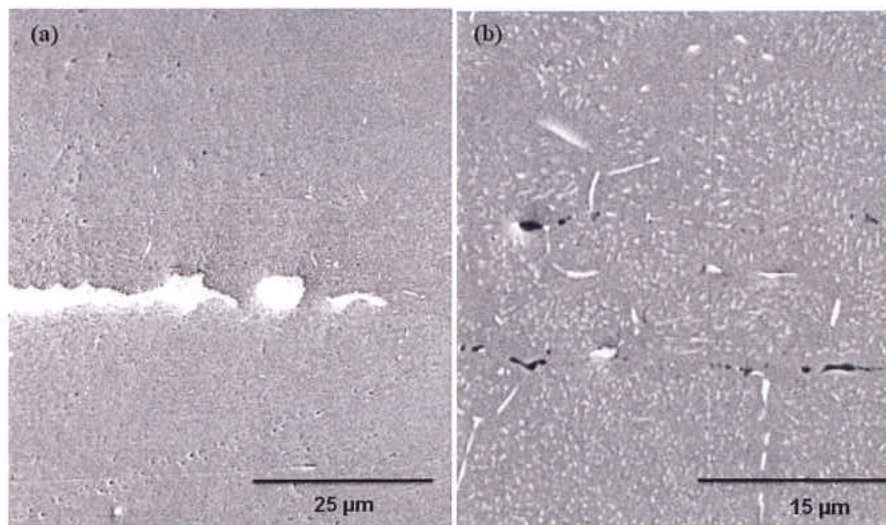


Figure 32. SEM images of diffusion bonded Fe using Au-12Ge interlayer (100 μm) at (a) 950°C and (b) 990°C for 15 h.

Figure 32 shows SEM images of diffusion bonded Fe using Au-12Ge interlayer (100 μm) at (a) 950°C and (b) 990°C for 15 h. At 950°C, the composition of the residual interlayer

and base metal near interface obtained were similar to those at 920°C. The thickness of the residual interlayer was also in the similar range. The amount of residual interlayer found was less than at previous conditions. At 990°C for 15 h, the interlayer completely diffused into the metal in most areas while it retained in a few areas. Au-rich particles were found with some pores in the bond centerline where interlayer diffused completely. The bond centerline microstructures of diffusion bonded cp-Fe were summarized in Table 3 and Table 4.

Table 3. Summary of the microstructure of TLP bonded Fe using Al, Au-20Sn and Cu interlayer.

Interlayer	Interlayer Thickness (μm)	Bonding Temp. ($^{\circ}\text{C}$)	Bonding Time	Bond Centerline Microstructure
Al	100	900	10	Intermetallics and pores appeared
Al	100	900	20	Intermetallics and pores appeared, pores increased in size
Au-20Sn	100	600	10	Residual interlayer (less than 1 μm)
Au-20Sn	100	650	10	No intermetallics nor residual interlayer
Cu	25	1085	30	Residual interlayer (~19 μm)
Cu	25	1100	3	Residual interlayer (~13.9 μm)
Cu	25	1100	4	Residual interlayer diffused completely in some areas and retained in some areas (~3.5 μm)
Cu	25	1100	5	No residual interlayer but porous microstructure appeared

Table 4. Summary of the microstructure of TLP bonded Fe using Au-12Ge interlayer

Interlayer	Interlayer Thickness (μm)	Bonding Temp. ($^{\circ}\text{C}$)	Bonding Time	Bond Centerline Microstructure
Au-12Ge	100	900	1	12.6 μm interlayer with irregular finger print structure
Au-12Ge	100	900	10	Interlayer diffused completely in a few areas but in most areas it retained (thickness – 6.3 μm)
Au-12Ge	100	920	15	Interlayer completely diffused in some areas and retained in some areas (thickness – 1.25 – 3.8 μm)
Au-12Ge	100	950	15	The amount of residual interlayer decreased to some extent but similar otherwise
Au-12Ge	100	990	15	Interlayer diffused completely into the base metal in most areas while retained in a few areas. Au-rich particles were observed in the bond centerline

Mechanical Properties

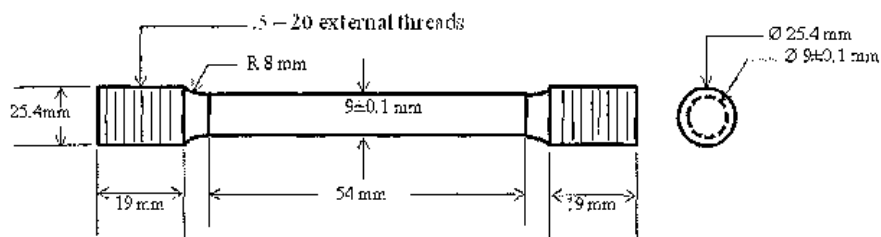


Figure 33. Schematic of the test geometry of tensile specimen.

Uniaxial tension tests were performed to investigate the tensile strength of the diffusion bonded joints. Fig. 33 shows schematic of the test geometry of tensile specimen. Table 5 shows tensile strengths of diffusion bonded Fe using Cu interlayers. For each data point three tensile specimen were tested. The maximum strength obtained for diffusion bonded

Table 5. Ultimate tensile strengths (UTS) of diffusion bonded Fe using Cu (25 μm) interlayer.

Bonding Temp. °C	Interlayer	Time (h)	UTS (MPa)
Normalized cp-Fe (965°C, 1 h)			316±2
Annealed cp-Fe (920°C, 15 h)			282±2
1000	Cu	10	279±3
1030	Cu	10	291±2
1050	Cu	10	287±1.5
1070	Cu	10	245±3
1085	Cu	10	237±1
1100	Cu	4	147±3

Fe using Cu interlayers was 291±2 MPa at 1030°C for 10 h. This falls between the strength values obtained for unbonded annealed or normalized specimens. All diffusion bonded tensile specimens using Cu interlayers failed in the joint line. In comparison, annealed commercially pure Cu has an ultimate tensile strength of 250 MPa [39]. As the bonding temperature increased beyond 1030°C, the strength decreased to 245±3 MPa and 237±1 MPa for samples bonded at 1070°C and 1085°C, respectively. Samples bonded at 1100°C for 4 h or more failed under a very low tensile load. Samples bonded at 1100°C for 5 h or more did not show any strength because a porous microstructure appeared in the bond centerline.

Table 6 shows tensile strengths of diffusion bonded Fe using Au-12Ge interlayers. The strength of bonded Fe using Au-12Ge at 920°C for 15 h was 284±1 MPa. These samples failed away from the joint area. The strengths obtained for annealed and normalized cp-Fe were 282±2 and 316±2 MPa, respectively. The strength of the diffusion bonded Fe at 920°C was almost same as the annealed cp-Fe. To determine the strength of the joint diffusion bonded Fe was normalized (air cooled from the bonding temperature). The

Table 6. Ultimate tensile strengths (UTS) of diffusion bonded Fe using Au-12Ge (100 μm) interlayer

Bonding Temp. $^{\circ}\text{C}$	Interlayer	Time (h)	UTS (MPa)
Normalized cp-Fe (965 $^{\circ}\text{C}$, 1 h)			316 \pm 2
Annealed cp-Fe (920 $^{\circ}\text{C}$, 15 h)			282 \pm 2
920	Au-12Ge	15	*284 \pm 1
890 (normalized)	Au-12Ge	15	287 \pm 2
920 (normalized)	Au-12Ge	15	302 \pm 1
950 (normalized)	Au-12Ge	15	315 \pm 4
970 (normalized)	Au-12Ge	15	314 \pm 4
990 (normalized)	Au-12Ge	15	302 \pm 3

* Specimen failed away from bondline

normalized diffusion bonded Fe had maximum ultimate tensile strengths of 315 \pm 4 MPa at 950 $^{\circ}\text{C}$ for 15 h and they failed in the bonded area. Normalized diffusion bonded Fe did not fail in the base metal area because the grains of base metal became finer by

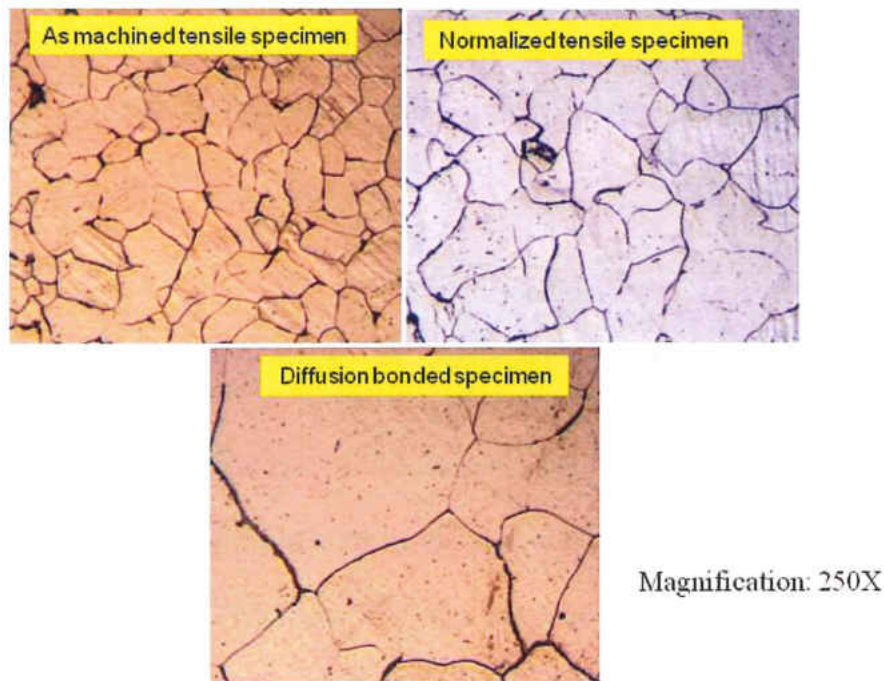


Figure 34. Optical micrographs of raw, normalized and diffusion bonded tensile specimen.

normalization as can be seen in Figure 34. The yield strength of metals is inversely related to grain size. The tensile strengths for the samples bonded at 970°C for 15 h were almost same as for samples bonded at 950°C for 15 h. However, strengths decreased to 302 ± 3 MPa for the samples bonded at 990°C for 15 h. The lower strength at this bonding condition was due to the porous microstructure in the joint centerline.

Conclusions

Diffusion bonding of cp-Fe using Cu interlayers showed a residual Cu interlayer from 1000-1100°C for most bonding times. At 1100°C for 5h, no residual Cu was obtained; however, a porous microstructure appeared along the bond centerline. The highest tensile strength was obtained at 1030°C for 10 h and the strength decreased as the bonding temperature increased. Fingerprint-like microstructure appeared in the residual interlayer when Fe was bonded with a Au-12Ge interlayer. The microstructure of the base metal near bond centerline contained dispersed Au-rich particles. The highest strength observed was 315 ± 4 MPa for the sample bonded at 950°C for 15 h and normalized. This is almost the same strength as normalized Fe.

Ni-Ni Bonding

Microstructures

Figure 35 shows a SEM image of diffusion bonded Ni using Al interlayer (100 μm) at 800°C for 10 h. The microstructure of the joint centerline consisted of three different layers with different Al contents. The layer at the center consisted of 43-47 wt. % Al and then the next two layers consisted of 32 and 17 wt. % Al, respectively. Also, a porous microstructure appeared in the joint centerline. The Ni-Al equilibrium phase diagram

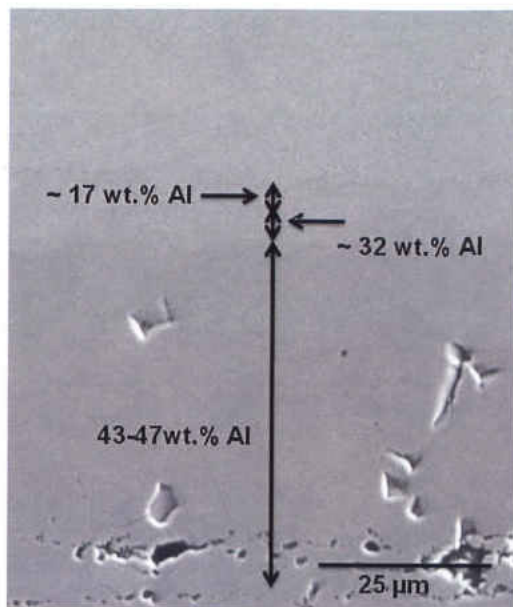


Figure 35. SEM image of diffusion bonded Ni using Al interlayer (100 μm) at 800°C for 10 h.

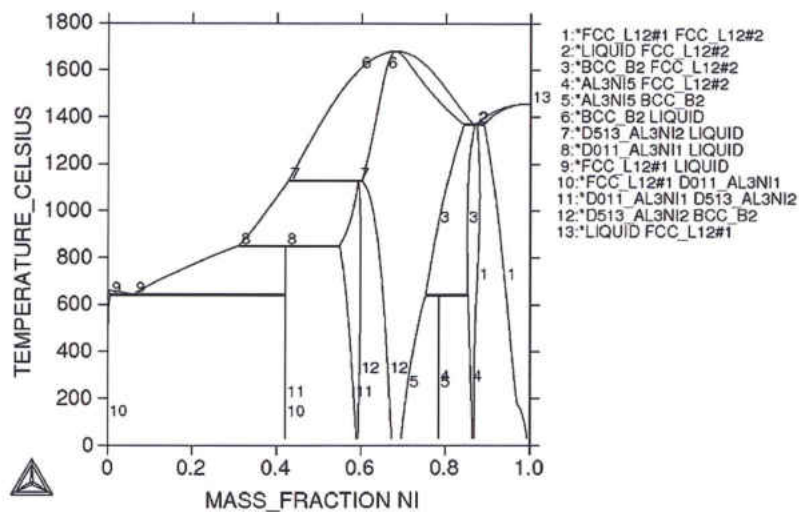


Figure 36. Ni-Al equilibrium diagram generated in ThermoCalc version TCW5.

(Figure 36) indicated that Al and Ni form a number of intermetallics depending composition. The bond centerline microstructure consisted of probably a mixture of Al and Al_3Ni_5 , the next layer was AlNi and the last layer was Al_3Ni_5 . Then the Al percentage decreased sharply to trace amount. The composition of Al from bond centerline to the

interior of base metal decreased step-wise because of the formation of intermetallics.

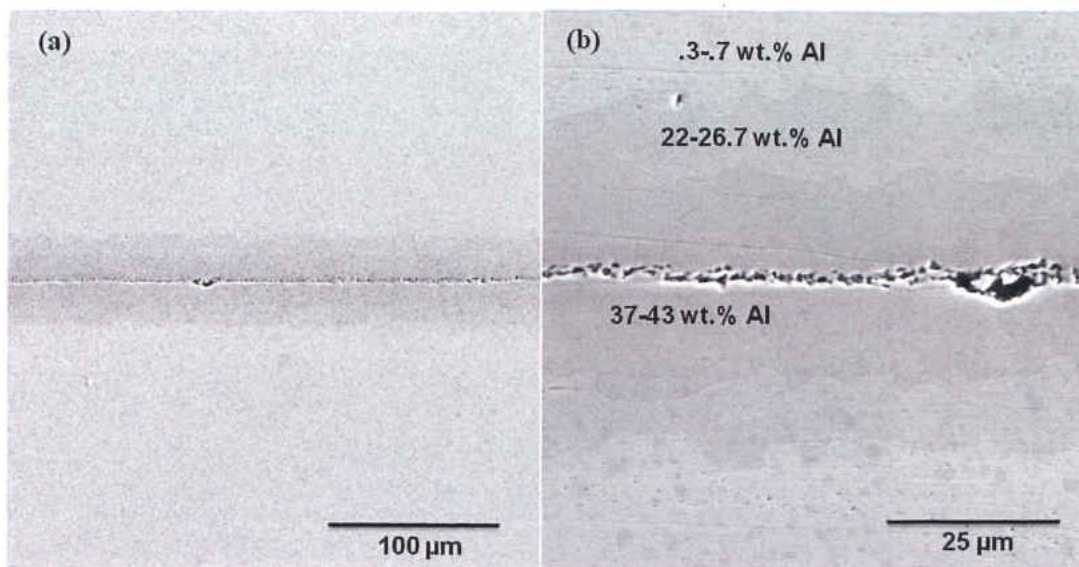


Figure 37. (a) SEM image of diffusion bonded Ni using Al interlayer (100 μm) at 800°C for 30 h and (b) magnified image of (a).

Figure 37 shows (a) SEM image of diffusion bonded Ni using Al interlayer (100 μm) at 800°C for 30 h and (b) magnified image of (a). In this case, the microstructure of the joint area consisted of two layers. The composition of the layer just at the center was 37-43 wt. % Al and for the next layer it was 22-26.7 wt. % Al and then abruptly decreased to .3-.7 wt. % Al. The porous microstructure in the bond centerline increased to some extent. According to the composition, the microstructure of the centerline was either Al_3Ni or Al_3Ni_2 . The next layer was probably AlNi or Al_3Ni_5 or a mixture of both. The intermetallics formed in the joint line were stable phases at the joining temperature.

Figure 38 shows (a) SEM image of diffusion bonded Ni using Al interlayer (25 μm) at 800°C for 10 h and (b) magnified image of (a). The concentration profile of Al from the bond centerline to the interior of the metal is shown on Figure 39. The SEM images

indicated that the microstructure of the bonded area consisted of three different zones.

According to the EDS analysis, the centerline microstructure was either Al_3Ni or AlNi or

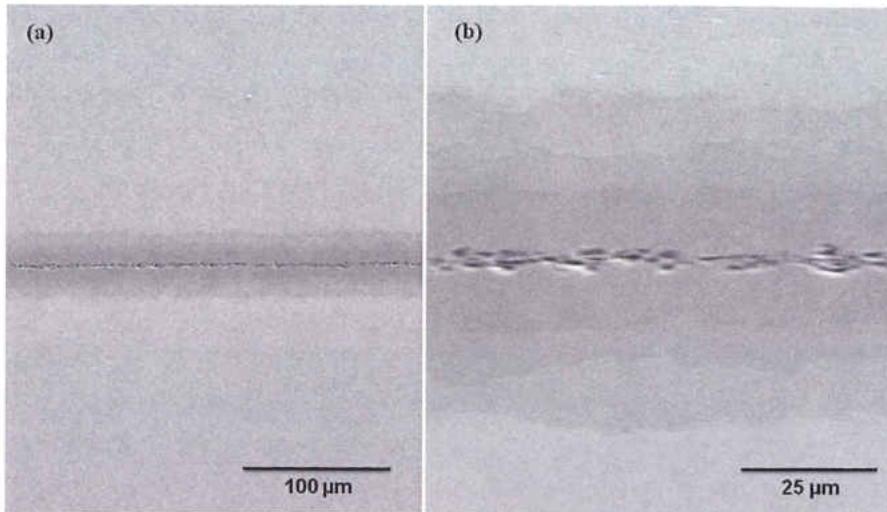


Figure 38. (a) SEM image of diffusion bonded Ni using Al interlayer (25 μm) at 800°C for 10 h and (b) magnified image of (a).

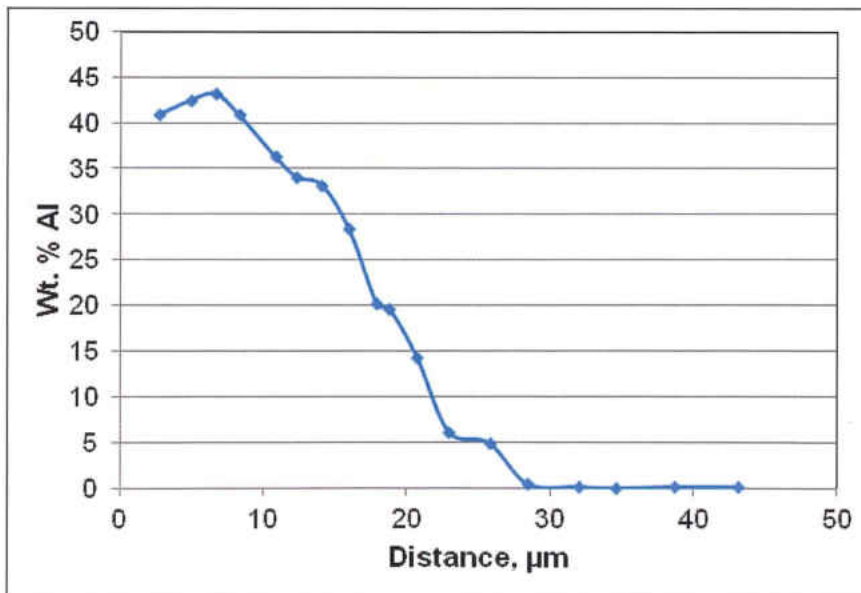


Figure 39. Concentration profiles of Al in diffusion bonded Ni using Al interlayer (25 μm) at 800°C for 10 h.

a mixture of these two. The next regions were AlNi and Al₃Ni₅, respectively. Trace amounts of Al were found after these regions of intermetallics. The formation of intermetallics was unavoidable in the joint area for diffusion bonded Ni using Al interlayers. This would potentially provide very low strength of the joint.

Figure 40 shows (a) SEM image of diffusion bonded Ni using Au-12Ge interlayer (100 μm) at 900°C for 1 h and (b) magnified image of (a). Although the melting temperature

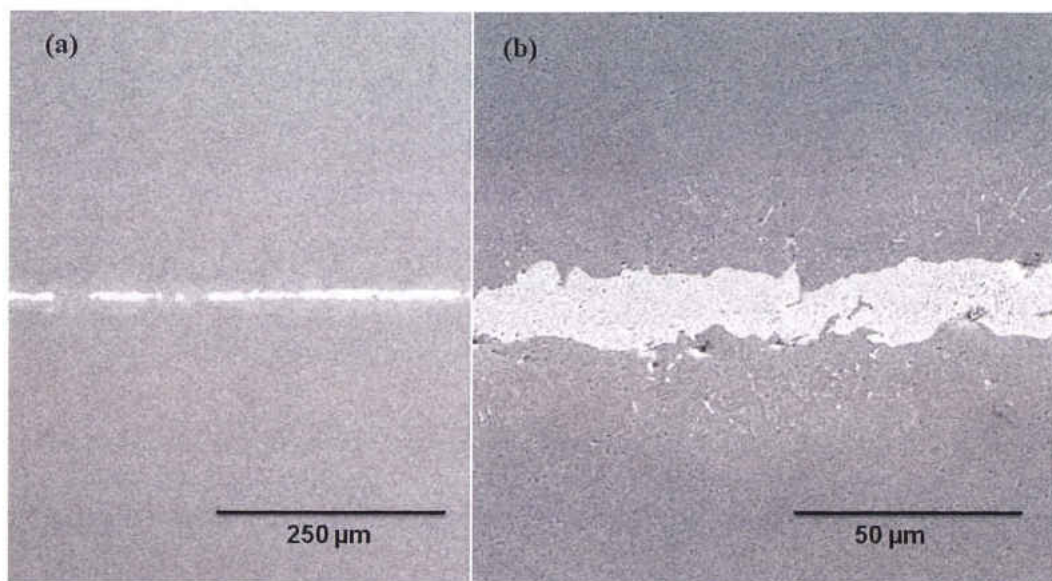


Figure 40. (a) SEM image of diffusion bonded Ni using Au-12Ge interlayer (100 μm) at 900°C for 1 h and (b) magnified image of (a).

of eutectic Au-12Ge alloy is only 361°C, residual interlayer was found in the bond centerline after bonding at 900°C for 1 h. The thickness of the residual interlayer was 12.6-17.7 μm, though the interlayer diffused completely in few places. The composition of the residual interlayer was ~78 wt.% Au, ~16 wt. % Ni with no Ge. The interface in the base metal side contained 56 wt.% Ni, 36 wt.% Au and 2.9 wt.% Ge. Then the amount of Ni was increased, and the amount of Au and Ge were decreased into the base

metal.

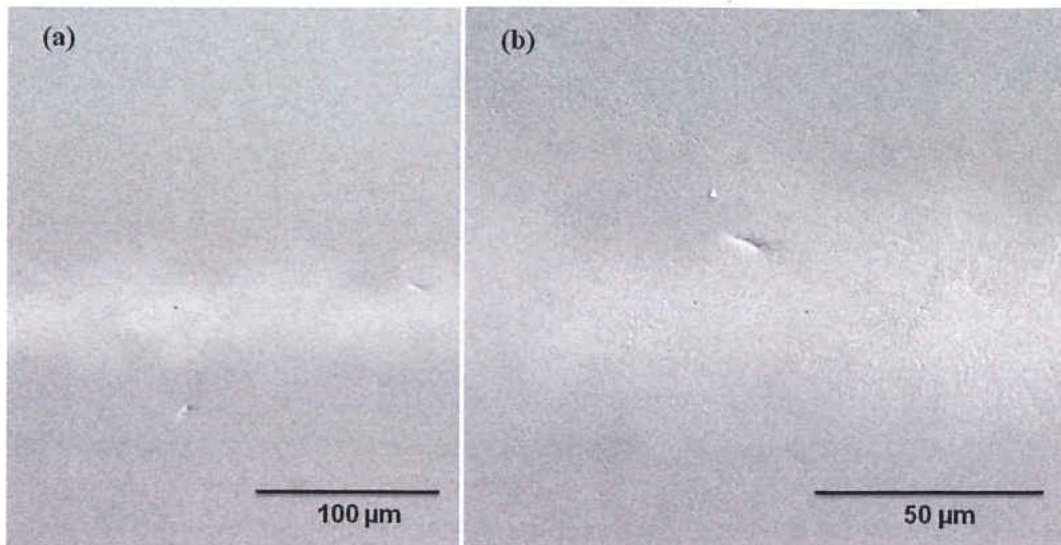


Figure 41. (a) SEM image of diffusion bonded Ni using Au-12Ge interlayer (100 μm) at 900°C for 15 h and (b) magnified image of (a).

As the residual interlayers are undesirable in the bond centerline, the joining time was increased to enhance interdiffusion, keeping the joining temperature at 900°C. Figure 41 shows (a) SEM image of diffusion bonded Ni using Au-12Ge interlayer (100 μm) at 900°C for 15 h and (b) magnified image of (a). No residual interlayer found at these bonding conditions. The joint centerline microstructure consisted of 62 wt.% Ni and 34 wt.% Au with no Ge. Then the amount of Au and Ge decreased gradually from the centerline to the interior of the base metal.

Figure 42 shows (a) SEM image of diffusion bonded Ni using Au-12Ge interlayer (100 μm) at 960°C for 10 h and (b) magnified image of (a). No residual interlayer was found

at these bonding conditions either. The composition of the bond centerline consisted of

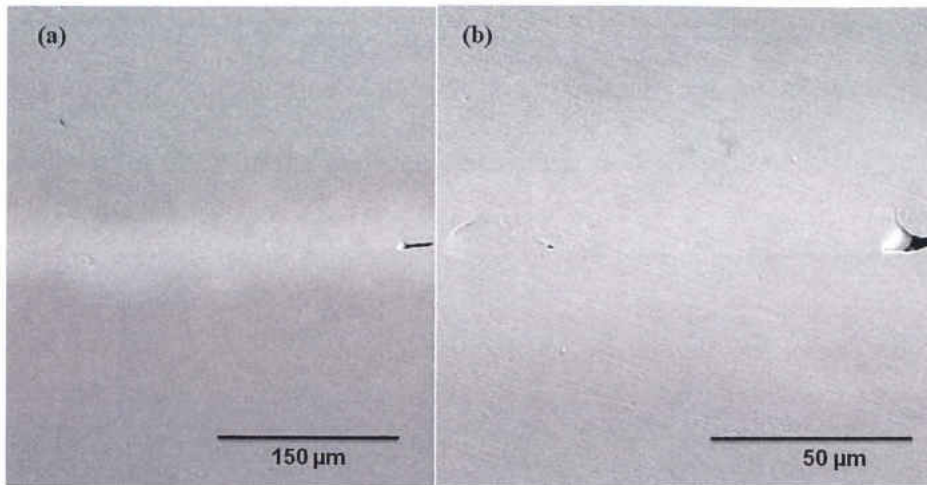


Figure 42. (a) SEM image of diffusion bonded Ni using Au-12Ge interlayer (100 μm) at 960°C for 10 h and (b) magnified image of (a).

62 wt.% Ni, 30 wt.% Au and 4.9 wt.% Ge. Few pores appeared in the joint area. It is apparent that the higher bonding time and temperatures increase the interdiffusion.

According to the Au-Ni phase diagram, no intermetallics form for this binary system.

Accordingly, no intermetallics were found in the bonded area for any bonding conditions.

Although Ni and Au form complete solid solution at any compositions range, the microstructure in the bonded area consisted of Ni, Au and Ge were easily distinguishable from unbonded area.

Figure 43 shows SEM images of diffusion bonded Ni using Cu interlayer (25 μm) at 1070°C for (a) 10 h and (b) 15 h. According to the EDS analysis, the maximum Cu found in the bond centerline was 38 wt.% with 60 wt. % Ni for 10 h bonding time. For 15 h bonding time, the amount of Cu and Ni obtained in the bond centerline were 34 wt.% and 64 wt.%, respectively. The microstructure of bonded area was similar to the unbonded

area for both cases. This could be due to the formation of complete solid solution for Ni-Cu system at any composition range. There were a few small pores found in the bonded area for 15 h bonding time. As Cu does not form any intermetallics with Ni, no such phases were found in the joint microstructure.

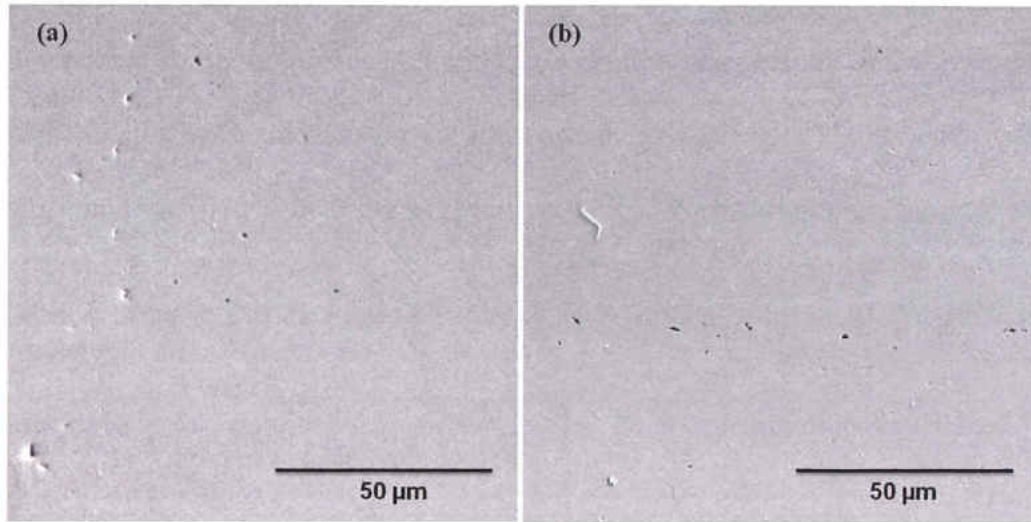


Figure 43. SEM images of diffusion bonded Ni using Cu interlayer (25 μm) at 1070°C for (a) 10 h and (b) 15 h.

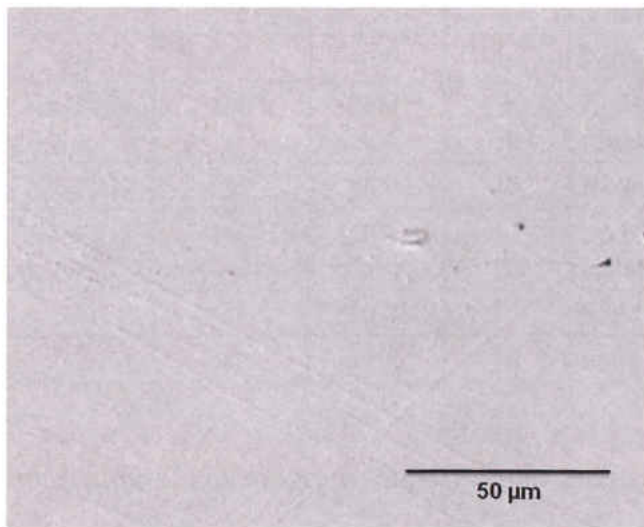


Figure 44. SEM images of diffusion bonded Ni using Cu interlayer (25 μm) at 1100°C for 10 h.

Figure 44 shows SEM images of diffusion bonded Ni using Cu interlayer (25 μm) at 1100°C for 10 h. The microstructure of the bond centerline consisted of 34 wt.% Cu and 63 wt. % Ni. The amount of Cu decreased gradually away from the joint centerline. In this case also the bonded microstructure was not distinguishable from the unbonded microstructure. The amount of pores in the bonded area was decreased. The bonding temperature for this case was higher than the melting temperature of Cu. However, the interdiffusion of Cu and Ni was not enhanced significantly as a similar microstructure was found for 1070°C bonding temperature with 15 h bonding time. During the bonding

Table 7. Summary of the microstructure of TLP bonded Ni using Al, Au-12Ge and Cu interlayer

Interlayer	Interlayer Thickness (μm)	Bonding Temp. ($^{\circ}\text{C}$)	Bonding Time	Bond Centerline Microstructure
Al	100	800	10	Porous microstructure in the joint centerline, different intermetallics with different Al content
Al	100	800	30	Same as previous conditions, only porosity increased
Al	25	800	10	Porosity and intermetallics
Au-12Ge	100	900	1	Residual interlayer observed (thickness 16.6-17.7 μm)
Au-12Ge	100	900	15	No residual interlayer
Au-12Ge	100	960	10	No residual interlayer, few pores appeared
Cu	25	1070	15	Solid solution of Cu and Ni
Cu	25	1100	10	Solid solution of Cu and Ni

process, the Cu interlayer is initially liquid and its composition changes as interdiffusion occurs. Cu-10Ni alloy has an approximately 1100°C solidus temperature. As isothermal solidification completes, the interdiffusion becomes sluggish. Moreover, Cu and Ni both have very compact crystal structure (FCC) which is also responsible for slow diffusion in

each other. The microstructures of the joint centerline of diffusion bonded Ni is summarized in Table 7.

Mechanical Properties

Since intermetallics were formed in the bonded area for all bonding conditions with Al interlayer, no appreciable joining strengths were obtained in this case. On the other hand, no intermetallics were found in the joining area with Cu interlayer; yet, surprisingly, no appreciable joining strengths were obtained with this interlayer. The joining strength obtained with Au-12Ge interlayer was 77 ± 15 MPa at 960°C for 10 h. However, this strength is much lower than the strength of base metal (558 ± 4 MPa).

Conclusions

TLP joining of cp-Ni using Al interlayer was not useful because of the formation of intermetallics at any bonding conditions. Although no intermetallics were found when bonded using Cu interlayer, also no appreciable strength was obtained. The tensile strength obtained for the joint with Au-12Ge interlayer was very low compared to the strength of base alloy.

CHAPTER III

MODELING OF TRANSIENT LIQUID PHASE DIFFUSION BONDING

Introduction

Transient liquid phase (TLP) diffusion bonding is applied to those materials for which other bonding methods are not feasible. However, commercial utilization of this process is relatively limited because the incomplete understanding of this process does not allow optimization of various process parameters. Nevertheless, there have been many analytical studies of TLP diffusion bonding. Since the TLP bonding process is a diffusion process, Fick's laws of diffusion are the basis of the modeling of the TLP bonding method. Appropriate boundary conditions are required to solve these equations.

Equilibrium phase diagrams are used to obtain solute concentrations at the bonding temperature, which are then used to calculate the isothermal solidification time and homogenization time. However, the migrating solid/liquid interface in TLP bonding process complicates the problem. Some models are approximate models which calculate the solidification and homogenization time considering a fixed boundary problem; other models attempt to account for the moving boundary problem.

TLP Modeling

TLP diffusion bonding is a diffusion process involving both solid and liquid phases.

Therefore, it is expected to follow Fick's 1st and 2nd laws:

$$J = -D \frac{\partial C}{\partial x} \quad (\text{Fick's 1}^{\text{st}} \text{ law}) \quad (1)$$

$$\frac{\partial C}{\partial t} = D \frac{\partial^2 C}{\partial x^2} \quad (\text{Fick's 2}^{\text{nd}} \text{ law}) \quad (2)$$

F is the rate of transfer per unit area of section, C the concentration of the diffusing substance, x the distance normal to the section, D the diffusivity and t is the time.

T. Padron et al. [40] have investigated the TLP bonding of duplex stainless steel (DSS) using Cu interlayer. Two models have been proposed based on Fick's 2nd law: a half semi-infinite base metal with a stationary interface and two semi-infinite phases with a coupled diffusion-controlled migrating solid/liquid interface.

Model 1 (Stationary Interface)

The concentration of solute atoms in the base material is C_M throughout and at the interface the solute concentration is maintained as $C_{\alpha L}$, so the solute concentration is given by Eq. 3 and 4,

$$\frac{C - C_{\alpha L}}{C_M - C_{\alpha L}} = \text{erf} \left[\frac{x}{\sqrt{4Dt}} \right] \quad (3)$$

$$C(x, t) = C_{\alpha L} + (C_M - C_{\alpha L}) \text{erf} \left[\frac{x}{\sqrt{4Dt}} \right] \quad (4)$$

Thus, the total solute flux that has entered the base material at time, t , is calculated using Fick's 1st law:

$$F(t) = (C_{\alpha L} - C_M) \sqrt{\frac{D}{\pi t}} \quad (5)$$

The total amount of solute, M_t , is given by integrating Eq. 5 between $t=0$ and $t=t_{IS}$ (time for isothermal solidification):

$$M_t = 2(C_{\alpha L} - C_M) \sqrt{\frac{Dt_{IS}}{\pi}} \quad (6)$$

At the end of the isothermal solidification stage all the solute in the interlayer controlling the solidification process has diffused into the base material, thus:

$$\frac{c_0 W_0}{2} = 2(C_{\alpha L} - C_M) \sqrt{\frac{Dt_{IS}}{\pi}} \quad (7)$$

and

$$t_{IS} = \left(\frac{\pi}{16D} \right) \frac{c_0^2 W_0^2}{(C_{\alpha L} - C_M)^2} \quad (8)$$

where C_0 and W_0 are the initial solute concentration and initial width of the interlayer, respectively.

Model 2 (Moving Solid/Liquid Interface)

This model considers two semi-infinite phases with a coupled diffusion-controlled migrating solid/liquid interface. In this case, the solute concentration is expressed in the general form:

$$C(x, t) = A_1 + A_2 \operatorname{erf} \left[\frac{x}{\sqrt{4Dt}} \right] \quad (9)$$

where A_1 and A_2 are constants and the boundary conditions are $C(\infty, t) = C_M$ and $C(x(t), t) = C_u$. As the interface displaces the distance x at time t , the concentration of solute is equal to $C_{\alpha L}$ and is given by:

$$C(x, t) = A_1 + A_2 \operatorname{erf} \left[\frac{x}{\sqrt{4Dt}} \right] = C_{\alpha L} \quad (10)$$

Since Eq. 10 has to be satisfied for all values of t , x must be proportional to $t^{1/2}$, thus:

$$\left[\frac{x}{\sqrt{4Dt}} \right] = K = \text{constant} \quad (11)$$

Considering that the displacement of the interface (x) during isothermal solidification is equal to $W_{\max}/2$ (W_{\max} is the maximum width of the liquid interlayer), t_{IS} is given by:

$$t_{IS} = \frac{W_{\max}^2}{16K^2 D} \quad (12)$$

Applying mass balance method, Tuah-Poku et al. [41] showed that: $W_{\max} =$

$$W_0 \left[1 + \left(\frac{\rho_b}{\rho_a} \right) \left(\frac{C_0 - C_{L\alpha}}{C_{L\alpha}} \right) \right] \quad (13)$$

where $C_{L\alpha}$ is the solute concentration at which the liquid interlayer homogenizes, ρ_b is the density of the interlayer material, and ρ_a the density of the base material.

Zhou et al. [42] indicated that K in Eq. 12 has to be numerically calculated using Eq. 14

$$\frac{K(1+\operatorname{erf}(K)\sqrt{\pi})}{\exp(-K^2)} = \frac{C_{\alpha L}-C_M}{C_{L\alpha}-C_M} \quad (14)$$

Time for isothermal solidification can be calculated using Model 1 or Model 2. Zhou [43] concluded that Model 2 provides a better approximation for the completion time of the isothermal solidification stage but Model 1 is a good approximation of Model 2 when C_M and $C_{\alpha L}$ are very small and $C_{L\alpha}$ is relatively large. Zhou et al. [43] indicated that the homogenization stage time can be estimated assuming that initially there is a solidified region on either side of the bond centre-line ($x + h, x - h$) with a solute concentration equal to $C_{\alpha L}$, and the initial solute concentration in the base metal is equal to C_M . The solute concentration is then given by [43]:

$$C(x, t) = C_M + \frac{1}{2}(C_{\alpha L} - C_M) \times \left[\operatorname{erf} \left[\frac{x+h}{\sqrt{4Dt}} \right] - \operatorname{erf} \left[\frac{x-h}{\sqrt{4Dt}} \right] \right] \quad (15)$$

where h is half the maximum liquid width at the end of the dissolution stage ($W_{\max}/2$).

At the end of the homogenization stage, the maximum solute concentration is attained in the center line ($x = 0$), thus at homogenization time (t_H) the solute concentration is given by:

$$C_{\max}(x = 0, t_H) = C_M + \frac{1}{2}(C_{\alpha L} - C_M) \times \left[\operatorname{erf} \left[\frac{h}{\sqrt{4Dt_H}} \right] - \operatorname{erf} \left[\frac{-h}{\sqrt{4Dt_H}} \right] \right] \quad (16)$$

Since $\operatorname{erf}(-x) = -\operatorname{erf}(x)$, Eq. (16) can be written:

$$C_{\max}(x = 0, t_H) = C_M + \frac{1}{2}(C_{\alpha L} - C_M) \times \left[2\operatorname{erf} \left[\frac{h}{\sqrt{4Dt_H}} \right] \right] \quad (17)$$

Hence:

$$C_{max}(x = 0, t_H) = C_M + (C_{\alpha L} - C_M) \times \left[\text{erf} \left[\frac{h}{\sqrt{4Dt_H}} \right] \right] \quad (18)$$

Knowing the maximum concentration in the bond centre line, t_H can be estimated using Eq. 18.

Experimental results for the DSS/Cu/DSS were compared with the results of the models above. Since Fe is the main element in DSS, the Fe-Cu phase diagram is used to identify the concentration limits. When the diffusivity used in the calculations was a geometric mean of lattice diffusion of Cu in ferrite ($D_{lattice-\alpha}^{Cu}$) and grain boundary diffusion of Cu in ferrite ($D_{gb-\alpha}^{Cu}$), a good agreement was achieved between the calculated and experimentally observed results. According to these results, the lattice and grain boundary diffusion through the α -phase in the steel plays a dominant role during the TLP bonding process. The calculated homogenization rate deviates significantly from the experimental value. However, the time estimations for isothermal solidification stage are a good approximation of the time for the whole process.

M. A. Arafin et al. [44] proposed a modified model (named as “random walk” model) for isothermal solidification time because the uncertainties associated with experiment are not considered in either of the above models. For example, complexity in measuring the exact eutectic width poses a big challenge and is typically based on the assumption of a linear relationship between the eutectic width and square root of holding time. The isothermal solidification time is predicted by the following equation:

$$t_{i,j} = \frac{w^2}{\left(2 \times \text{erf}^{-1}(C_s/C_0) \times \sqrt{R_{D_j}} \right)^2} \quad (19)$$

where w is half of the initial joint gap, R_{D_j} is a random number based on the statistical distribution profile of D_j , the diffusion coefficient at a specified temperature, C_s is the solute concentration of the solid phase at the solid/liquid interface and C_0 is the initial solute concentration in the interlayer.

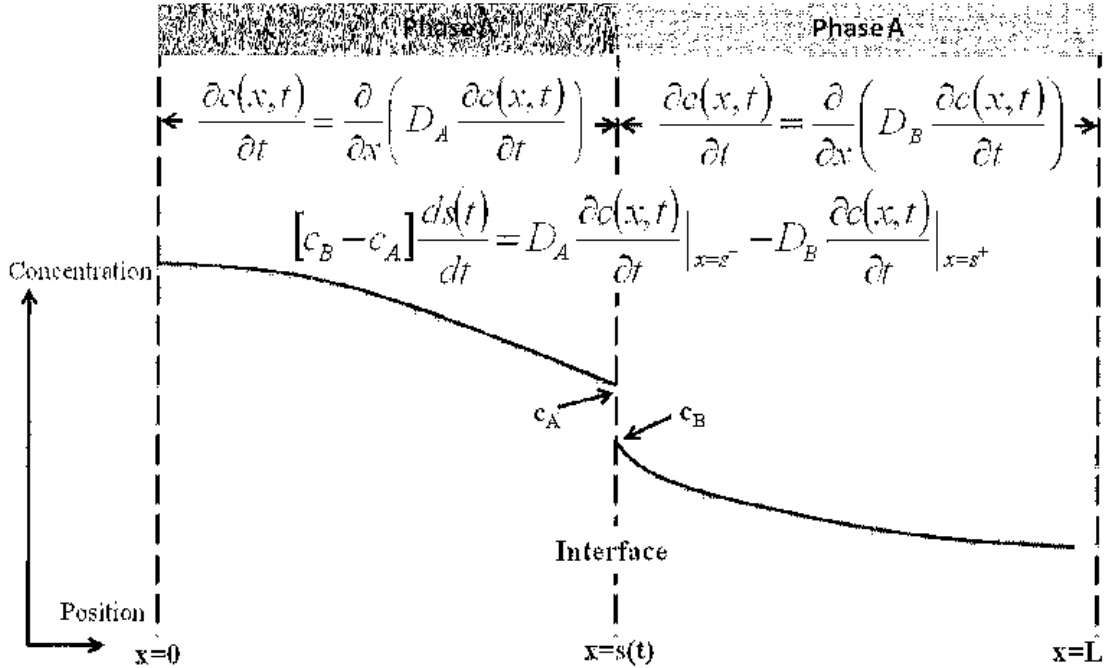


Figure 45. Schematic diagram showing the concentration profile across a TLP bond at one instant in time. Only half of the joint is shown; the other half (from $x = -L$ to $x = 0$) will be symmetrical [45].

T. C. Illingworth et al. [45] introduced a new variable, $s(t)$, to describe the position of a solid/liquid interface which is a function of time (Figure 45). The moving boundary problem can then be expressed as [46]:

$$\frac{\partial c(x,t)}{\partial t} = \frac{\partial}{\partial x} \left(D_A(c(x,t)) \frac{\partial c(x,t)}{\partial x} \right), \quad 0 < x < s(t) \quad (20)$$

$$\frac{\partial c(x,t)}{\partial t} = \frac{\partial}{\partial x} \left(D_B(c(x,t)) \frac{\partial c(x,t)}{\partial x} \right), \quad s(t) < x < L \quad (21)$$

$$D_A(c(x, t)) \frac{\partial c(x, t)}{\partial x} \Big|_{x=s(t)^-} - D_B(c(x, t)) \frac{\partial c(x, t)}{\partial x} \Big|_{x=s(t)^+} = [c_B - c_A] \frac{ds(t)}{dt},$$

$$x = s(t) \tag{22}$$

Instead of tracking the moving interface, a mesh is used that takes account of the moving interface. A variable space grid is achieved by introducing a wholesale coordinate transformation using two positional variables: $u = x/s(t)$ and $v = (x-s(t))/(L-s(t))$. These definitions mean that, for any time, the interval $0 < x < s(t)$ coincides with $0 < u < 1$, and that $s(t) < x < L$ coincides with $0 < v < 1$. Now the governing Eqs. 20-22 become:

$$s(t)^2 \frac{\partial p(u, t)}{\partial t} - us(t) \frac{ds(t)}{dt} \frac{\partial p(u, t)}{\partial u} = \frac{\partial}{\partial u} \left(D_A(p(u, t)) \frac{\partial p(u, t)}{\partial u} \right), \quad 0 < u < 1 \tag{23}$$

$$[L - s(t)]^2 \frac{\partial q(v, t)}{\partial t} - (1 - v)[L - s(t)] \frac{ds(t)}{dt} \frac{\partial q(v, t)}{\partial v} = \frac{\partial}{\partial v} \left(D_B(q(v, t)) \frac{\partial q(v, t)}{\partial v} \right),$$

$$0 < v < 1 \tag{24}$$

$$\frac{D_A(p(u, t)) \frac{\partial p(u, t)}{\partial u} \Big|_{u=1}}{s(t)} - \frac{D_B(q(v, t)) \frac{\partial q(v, t)}{\partial v} \Big|_{v=0}}{L-s(t)} = [c_B - c_A] \frac{ds(t)}{dt}, \quad u = 1; v = 0 \tag{25}$$

Eq. 23 can be written as

$$\frac{\partial (ps)}{\partial t} = \frac{ds}{dt} \frac{\partial (pu)}{\partial u} + \frac{1}{s} \frac{\partial}{\partial u} \left(D_A \frac{\partial p}{\partial u} \right), \quad 0 < u < 1 \tag{26}$$

Similarly, Eq. 24 can be written as

$$\frac{\partial (q[L-s])}{\partial t} = \frac{ds}{dt} \frac{\partial (q(1-v))}{\partial v} + \frac{1}{L-s} \frac{\partial}{\partial v} \left(D_B \frac{\partial q}{\partial v} \right), \quad 0 < v < 1 \tag{27}$$

Discretising the space coordinate u at N points ($u_0 \dots u_{N-1}$), writing $u_{i\pm 1/2}$ as the position midway between u_i and $u_{i\pm 1}$ and introducing the time-step δt such that $t^{j+1} = t^j + \delta t$, the finite volume technique [47] is used to integrate the divergent form Eq. 26 over one spacestep and one timestep; and introducing $p_i^{j+\sigma}$ (and $s^{j+\sigma}$) to represent the concentration at u_i (and the interface position) after a proportion, σ , of the time-step has elapsed, Eq. 26 leads to the approximation:

$$\begin{aligned}
& (p_i^{j+1} s^{j+1} - p_i^j s^j) \left(u_{i+\frac{1}{2}} - u_{i-\frac{1}{2}} \right) = \frac{\delta t}{s^{j+\sigma}} \left((D_A)_{i+\frac{1}{2}}^{j+\sigma} \frac{p_{i+1}^{j+\sigma} - p_{i-1}^{j+\sigma}}{u_{i+1} - u_i} - (D_A)_{i-\frac{1}{2}}^{j+\sigma} \frac{p_i^{j+\sigma} - p_{i-1}^{j+\sigma}}{u_i - u_{i-1}} \right) + \\
& (s^{j+1} - s^j) \times \left(p_{i+\frac{1}{2}}^{j+\sigma} u_{i+\frac{1}{2}} - p_{i-\frac{1}{2}}^{j+\sigma} u_{i-\frac{1}{2}} \right) \tag{28}
\end{aligned}$$

where $(D_A)_{i\pm 1/2}^{j+\sigma}$ correspond to the diffusion coefficients for the concentrations mid-way between discretisation points.

Eq. 27 can be rewritten for future compositions in B:

$$\begin{aligned}
& \left(q_i^{j+1} (L-s^{j+1}) - q_i^j (L-s^j) \right) \left(v_{i+1/2} - v_{i-1/2} \right) = \frac{\delta t}{L-s^{j+\sigma}} \left(D_B \frac{q_{i+1}^{j+\sigma} - q_{i-1}^{j+\sigma}}{v_{i+1} - v_i} - D_B \frac{q_i^{j+\sigma} - q_{i-1}^{j+\sigma}}{v_i - v_{i-1}} \right) + \\
& (s^{j+1} - s^j) \times \left(q_{i+1/2}^{j+\sigma} (1-v_{i+1/2}) - q_{i-1/2}^{j+\sigma} (1-v_{i-1/2}) \right) \tag{29}
\end{aligned}$$

A finite difference form of Eq. 25 can be derived in the same way. If v is discretised at $M-1$ points, the total amount of solute in the system at time t^{j+1} is

$$\begin{aligned}
& s^{j+1} \left[p_0^{j+1} \frac{u_1 - u_0}{2} + \sum_{i=1}^{N-2} p_i^{j+1} \frac{u_{i+1} - u_{i-1}}{2} + p_{N-1}^{j+1} \frac{u_N - u_{N-1}}{2} \right] + (L - s^{j+1}) \left[q_0^{j+1} \frac{v_1 - v_0}{2} + \right. \\
& \left. \sum_{i=1}^{M-2} q_i^{j+1} \frac{v_{i+1} - v_{i-1}}{2} + q_{M-1}^{j+1} \frac{v_M - v_{M-1}}{2} \right] \tag{30}
\end{aligned}$$

A similar expression gives the total amount of solute at time t^j . For the model to be conservative, the difference between these two values must be zero. Subtracting one from the other, and using Eqs. 28 and 29, Eq. 31 can be obtained which describes the motion of the interface:

$$\begin{aligned}
& \frac{D_B \delta t}{L-s^{j+\sigma}} \left(\frac{q_1^{j+\sigma}}{v_1} \right) - \frac{D_A \delta t}{s^{j+\sigma}} \frac{c_A - p_{N-2}^{j+\sigma}}{1-u_{N-2}} = (s^{j+1} - s^j) \left[\frac{1+u_{N-2}}{2} p_{N-1-1/2}^{j+\sigma} + \frac{1-u_{N-2}}{2} c_A - \right. \\
& \left. \left(1 - \frac{v_1}{2} \right) q_{1/2}^{j+\sigma} - \frac{v_1}{2} c_B \right] \tag{31}
\end{aligned}$$

Eqs. 28, 29, and 31 form a finite difference formulation of Eqs.16-18. An iterative solution method is used to solve the above equations. The model has been validated for a

variety of systems including Ni-(Ni-P)-Ni and diffusion of Zn in α - β brass and agreed very well with the experimental results [45].

The model proposed by T. Padron et al. fits well for a DSS/Cu/DSS combination considering lattice diffusion and grain boundary diffusion only in α -iron for solidification time. The homogenization time found from this model did not match with the experimental time. The model proposed by T. C. Illingworth et al. is a general model for TLP bonding. It has been validated for Ni-(Ni-P)-Ni TLP bonding and diffusion of Zn in α - β brass. This model can predict the position of solid/liquid interface more accurately. However, it has not been reported how it accounts for the diffusion of solute when there is a propensity for the formation of intermetallics.

Modeling of Diffusion Controlled Transformation Using Thermodynamic and Kinetic Database

Diffusion bonding processes are dictated by solid or liquid phase diffusion-controlled transformation. These processes are suitable for mathematical modeling. Although there are many analytical studies of diffusion-controlled transformation [2,48-49], the presence of a moving-interface boundary makes them complicated. To simulate diffusion-controlled transformations, tools to calculate the thermodynamic quantities and to treat the kinetics of the transformation are required. Thermocalc, developed at the Royal Institute of Technology in Stockholm, can predict the correct equilibrium state in multi-component alloys containing more than ten alloying elements [50]. DICTRA (Diffusion Controlled TRAnsformation) can simulate the concentration profiles of diffusing species in multi-component systems [51]. It is a finite difference code and uses a Newton-Raphson iteration technique to solve the multi-component diffusion equation. DICTRA

uses kinetic databases and recalls thermodynamic quantities from Thermocalc in solving the diffusion equations. The accuracy of prediction of concentration profiles in a diffusion couple using DICTRA depends on the accuracy of the thermodynamic and kinetic data and can be verified by comparison with experimental results.

Multicomponent Diffusion Model

For an isothermal, isobaric, one-phase binary alloy with diffusion of species k in one direction, z , Fick's 1st law is given by

$$J_k = -D_k \frac{\partial c_k}{\partial z} \quad (32)$$

where J_k is the interdiffusion flux (the amount of diffusing substance that passes per unit time and unit area of a plane perpendicular to the z -axis, defined with the volume-fixed frame of reference), c_k is the concentration of k (the amount of diffusing substance per unit volume), and D_k is the interdiffusion coefficient of species k and depends generally on concentration and temperature. Fick's 1st law is more useful when combined with the continuity equation:

$$\frac{\partial c_k}{\partial t} = \frac{\partial}{\partial z} (-J_k) \quad (33)$$

$$\frac{\partial c_k}{\partial t} = \frac{\partial}{\partial z} \left(D_k \frac{\partial c_k}{\partial z} \right) \quad (34)$$

Eq. 34 is another form of Fick's 2nd law. In multicomponent systems diffusivities do not depend only on concentration but also on concentration gradients. Onsager [52-53] extended Fick's 1st law to a multicomponent system by postulating that each thermodynamic flux was linearly related to every thermodynamic force. The Fick-Onsager law for multicomponent diffusion equation is given by:

$$J_k = -\sum_{i=1}^n L'_{ki} \frac{\partial \mu_i}{\partial z} \quad (35)$$

The μ_i terms are the chemical potentials for various species and, L'_{ki} are the proportionality factors that depend on the mobility of the individual species and will be discussed later. The expression for flux can be extended to Eq. 36 using the chain rule of derivation:

$$J_k = -\sum_{i=1}^n L'_{ki} \sum_{j=1}^n \frac{\partial \mu_i}{\partial c_j} \frac{\partial c_j}{\partial z} \quad (36)$$

If we introduce the unreduced diffusivities, D_{kj} , into Eq. 36 we obtain:

$$J_k = -\sum_{j=1}^n D_{kj} \frac{\partial c_j}{\partial z} \quad (37)$$

where

$$D_{kj} = \sum_{i=1}^n L'_{ki} \frac{\partial \mu_i}{\partial c_j} \quad (38)$$

The $\partial \mu_i / \partial c_j$ values are pure thermodynamic quantities referred to as thermodynamic factors. Eq. 38 indicates that the diffusivities consist of two separate parts, one purely thermodynamic and one kinetic. Assuming that all the substitutional species have the same partial molar volumes and only the substitutional species contribute to the volume, the reduced diffusivities in a volume-fixed frame of reference is expressed as

$$\bar{D}_{kj}^n = D_{kj}^V - D_{kn}^V \quad (39)$$

where n is the solvent and D_{kj}^V is given by Eq. 38 where V stands for volume fixed frame of reference and the concentration gradient of n has been eliminated. Eq. 37 now can be written using Eq. 39 as:

$$J_k = -\sum_{j=1}^{n-1} D_{kj}^n \frac{\partial c_j}{\partial z} \quad (40)$$

If Eq. 40 is combined with Eq. 33, we finally obtain a system of partial differential equations (PDEs) which is suitable for practical calculations of concentration profiles in multicomponent alloys.

Atomic Mobility

From absolute-reaction rate theory arguments, Anderson and Ågren [54] divided the mobility coefficient for element i , M_i , into a frequency factor, M_i^0 , and an activation enthalpy, Q_i :

$$M_i = \frac{M_i^0}{RT} \exp\left(\frac{-Q_i}{RT}\right) \quad (41)$$

where R is the gas constant and T is the absolute temperature. Both M_i^0 and Q_i depend on composition, temperature, and pressure. They expressed the composition and temperature dependency of M_i^0 and Q_i in terms of a Redlich-Kister polynomial,

$$Q_i = \sum_j x_j Q_i^j + \sum_p \sum_{j>p} x_p x_j \sum_k {}^k A_i^{pj} (x_p - x_j)^k \quad (42)$$

where Q_i^j and ${}^k A_i^{pj}$ are linear functions of temperatures. The mobilities are related to the interdiffusion coefficients by Eqs. 38, 39 and:

$$L'_{kj} = \sum_{i=1}^n (\delta_{ik} - c_k V_i) c_i y_{va} M_i \quad (43)$$

where δ_{ik} is the Kronecker delta; $\delta_{ik} = 1$ when $j = k$ and $\delta_{ik} = 0$ when otherwise. The terms c_k and c_i are the amounts of k and i per unit volume, respectively, V_i is the partial molar volume of element i , and y_{va} is the fraction vacant lattice sites on the sublattice where i is dissolved. M_i is the mobility of i when i is an interstitial solute and M_i should be divided by y_{va} when i is a substitutional solute. Tracer or self-diffusivity, D_i^* , is related to the atomic mobility by Einstein's relation:

$$D_i^* = RT M_i \quad (44)$$

Optimization of Mobility Parameter

The kinetic databases used in DICTRA are mobility parameters instead diffusivities to model diffusion controlled transformation. There are a few advantages of using mobility parameters in the kinetic database instead of diffusivity. Mobility parameters can be expressed as a linear function of temperature and the volume of the database to be handled and stored is decreased significantly. However, to obtain these parameters we do need either intrinsic coefficient or interdiffusion coefficient along with self-diffusion and tracer diffusion coefficient. These diffusion coefficients should be determined experimentally. The PARROT module in DICTRA uses experimental values of interdiffusion, self-diffusion, tracer diffusion and thermodynamic factors to calculate mobility parameter. The optimization begins with initial estimation of mobility parameters. The diffusion coefficients are calculated corresponding to the experimental data using these estimated parameters. Based on the comparison of the calculated and experimental diffusivities, the mobility parameters are optimized to achieve the best agreement possible. The problem setup and experimental interdiffusion coefficients used for optimization are shown in Appendix A.

Determination of Interdiffusion Coefficient

To optimize mobility parameter in PARROT module in DICTRA the interdiffusions coefficient are required which have to be determined experimentally. Interdiffusion coefficient is a function of concentration. For a binary diffusion system in which the partial molar volumes of the components are constant, Fick's 2nd law holds:

$$\left(\frac{\partial c_i}{\partial t}\right)_x = \left\{ \frac{\partial}{\partial x} \left(D \frac{\partial c_i}{\partial x} \right) \right\}_t \quad (45)$$

Boundary conditions:

$$t = 0: \quad x < x_0 \quad c_B = c_{B1}$$

$$x > x_0 \quad c_B = c_{B2}$$

$$t > 0: \quad x = -\infty \quad c_B = c_{B1}$$

$$x = +\infty \quad c_B = c_{B2}$$

Using the Matano-Boltzmann variable [55-56], D can be determined by:

$$D_{c_B^*} = \frac{-1}{2t \left(\frac{\partial c_B}{\partial x} \right)_{x^*}} \int_{c_{B1}}^{c_B^*} (x - x_0) dc_B \quad (46)$$

after location of the Matano-interface $x = x_0$, which is defined by:

$$\int_{c_{B1}}^{c_{B2}} (x - x_0) dc_B = 0 \quad (47)$$

For the constant molar volume case, the Matano-interface (the origin of the coordinate system) coincides with the geometrical interface which separated the two semi-infinite spaces of the diffusion couple at the beginning of the experiment. So, Eq. 46 can be written as [57]:

$$D_{c_B^*} = \frac{-1}{2t \left(\frac{\partial c_B}{\partial x} \right)_{x^*}} \int_{c_{B1}}^{c_B^*} x dc_B \quad (48)$$

The inter-diffusion coefficient can be calculated without the necessity of determining the position of the Matano-interface [58]:

$$D_{c_B^*} = \frac{1}{2t \left(\frac{\partial c_B}{\partial x} \right)_{x^*}} \left\{ (1 - y_c^*) \int_{-\infty}^{x^*} (c_B - c_{B1}) dx + y_c^* \int_{x^*}^{+\infty} (c_{B2} - c_B) dx \right\} \quad (49)$$

where, $y_c = \frac{c_B - c_{B1}}{c_{B2} - c_{B1}}$ and y_c^* is at x^* .

If the molar volume is not constant then the inter-diffusion coefficient can be calculated without the necessity of determining the position of the Matano-interface [58-60]:

$$D_{N_B^*} = \frac{(N_{B2} - N_{B1})V_m}{2t \left(\frac{\partial c_B}{\partial x}\right)_{x^*}} \left\{ (1 - y_N^*) \int_{-\infty}^{x^*} \frac{y_N}{V_m} dx + y_N^* \int_{x^*}^{+\infty} \frac{1 - y_N}{V_m} dx \right\} \quad (50)$$

where, $y_N = \frac{N_B - N_{B1}}{N_{B2} - N_{B1}}$ and y_N^* is at x^* and V_m is the molar volume of species B.

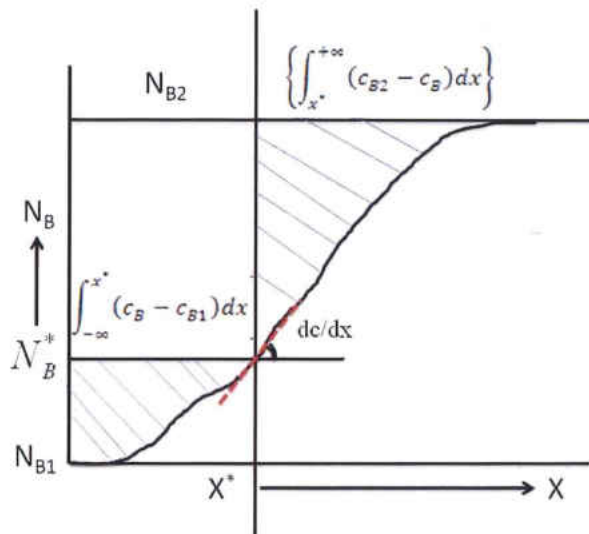


Figure 46. Schematic of concentration-distance profile.

It should be noted that the integrals in Eq. 48, 49 and 50 should be determined by graphical method from experimental data.

Moving Boundary Model

The modeling of a TLP bonding is treated as a moving boundary models. In the moving boundary models diffusion causes a phase transformation, *e. g.*, either growth or dissolution of individual particles in a matrix [61]. In this model, two different phases are

separated by a planar boundary (interface) and the migration of this interface is determined by the rate of interdiffusion across the interface. Let us consider the phase transformation between α and β phase (Figure 47). To conserve the mass (in moles) of a component k , a flux balance equation can be written as:

$$\frac{v^\alpha}{V_m^\alpha} [x_k^\alpha - x_k^\beta] = J_k^\alpha - J_k^\beta \quad k = 1, 2, \dots, n-1 \quad (51)$$

where v^α denotes the interface migration rate, x_k^α and x_k^β are the contents of component k in α and β close to the phase interface, J_k^α and J_k^β are the corresponding diffusional fluxes. The term V_m^α is the molar volume of the α phase.

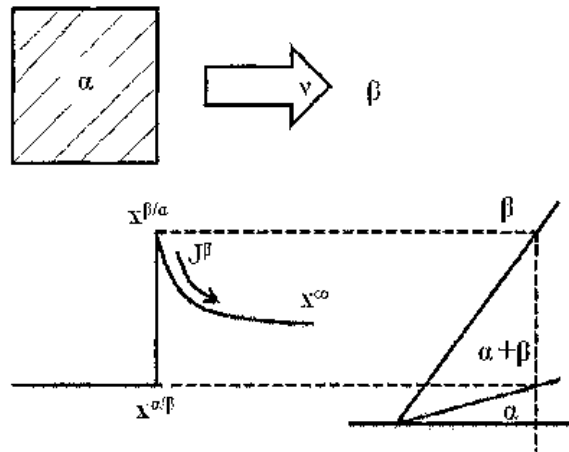


Figure 47. The α phase growing into β phase in a binary system under isothermal conditions. The corresponding concentration profile is shown in the lower left part of the figure and the phase diagram in the lower right part of the figure [62].

The integration in time is carried out by initially calculating the boundary conditions at the phase interface. In some cases, the interfacial reactions are faster than the migration of the phase interface. In those cases, the assumption is the thermodynamic equilibrium holds locally at the interface. This is referred to as the local equilibrium hypothesis, is

usually applied and allows the boundary conditions to be determined. The diffusion problem in each single-phase region can then be solved. The migration rate of the phase interface is determined by solving the flux-balance equation (Eq. 51). In the multicomponent system, this will generate a system of nonlinear equations, which have to be solved by an iterative procedure.

The local hypothesis implies that there is no difference in chemical potential on either side of the phase interface and that the concentration of the components can be determined from the equilibrium diagram. The rate of transformation is then only controlled by the transport of the components to and from the interface. This is an simplified assumption which may disregard many other possible effects present during a phase transformation, e.g., effects from curved interfaces, finite mobility of the interface, solute drag, and elastic stresses. These effects may cause a deviation from the local equilibrium.

In the present investigation, commercially pure Ni (cp-Ni) was diffusion bonded using a Cu, Al and Au-12Ge interlayers. The concentration profiles of the diffusing species were calculated using DICTRA. The calculated profiles obtained by the diffusion model were verified by comparing to corresponding experimental profiles.

Ni-Cu Binary System

Experimental Information

Three different types of diffusivity have been used for this investigation – self-diffusivity, tracer diffusivity and interdiffusivity. Self-diffusivity of Cu (Figure 48) was taken from

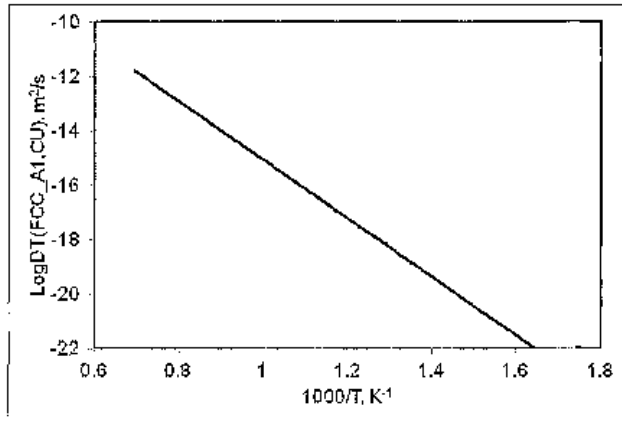


Figure 48. Temperature dependency of self-diffusion coefficient of Cu [63].

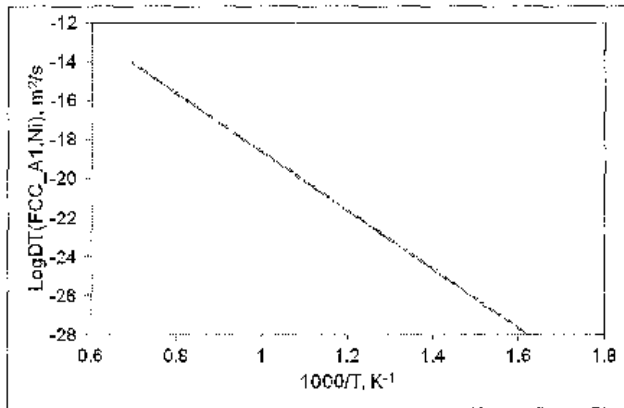


Figure 49. Temperature dependency of self-diffusion coefficient of Ni [64].

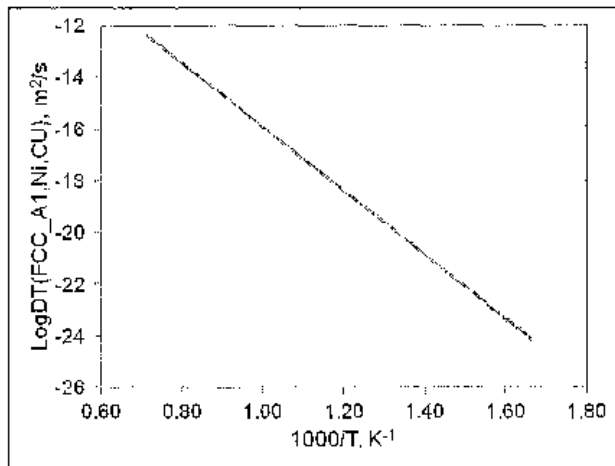


Figure 50. Temperature dependency of tracer diffusion coefficient of Ni in pure Cu [65].

Ghosh [63]. The self-diffusivity of Ni (Figure 49) determined by Jönsson [64] is widely accepted. Many researchers investigated the tracer diffusivity of Ni in Cu (Figure 50) using radioactive Ni over a wide range of temperatures. Among them, the tracer diffusion determined by Mackliet [65] has been considered as a benchmark. The tracer diffusion of

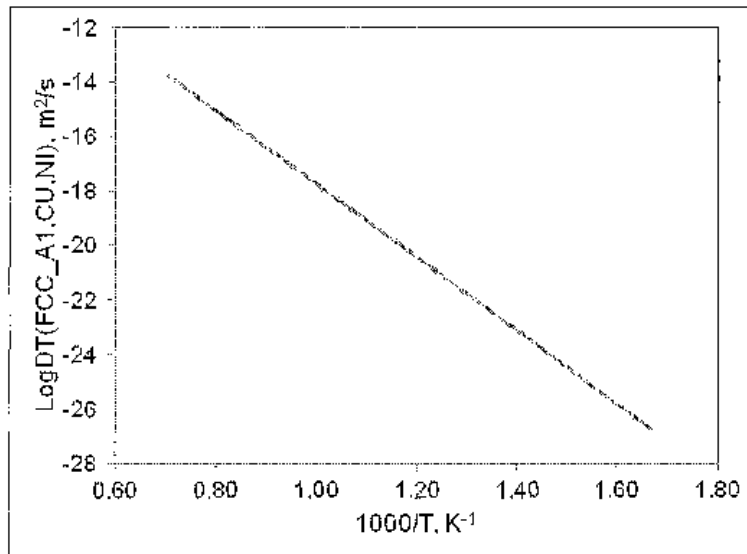


Figure 51. Temperature dependency of tracer diffusion coefficient of Cu in pure Ni [66].

Cu in Ni has been determined by two different groups [66-67]. Although their results agreed fairly well, the results from Monma et al. [66] (Figure 51) appear to be more reliable, because they carried out experiments at high temperatures (1054-1359°C) to avoid grain boundary diffusion contributions. A number of investigators have determined the interdiffusion coefficient in Ni-Cu alloys. The results from Grundhoff and Heumann [68] are in agreement with the results of Iijima et al. [69]. The diffusivities discussed above have been used for optimization of the mobility parameters.

Experimental Procedure

Commercially pure Ni (cp-Ni) was used as a base metal in this investigation. Cylindrical rods 6.35 mm in diameter and ~ 8 mm in length were used for diffusion bonding and subsequent microstructural investigation. The samples were polished to a 1200 grit finish and cleaned in an ultrasonic bath using isopropyl alcohol before bonding. The diffusion bonding was done using a 25 μm thick Cu (99.999 % pure, Alfa Aesar, USA) interlayers. The interlayer was inserted between two base metals to be bonded and held in a jig under a static pressure, and then the jig was put in a furnace. The applied clamping torque was 10 in-lb. The bonding temperature was 1050-1100°C and the bonding time was 10-15 h for a Cu interlayer. For microstructural observation, the bonded samples were mounted in resin and a longitudinal section was polished at approximately the midline of the piece. The microstructural observations were carried out using a Hitachi S-3400N scanning electron microscope (SEM). The compositions of the bonded area were analyzed by energy dispersive spectrometry (EDS).

Results and Discussion

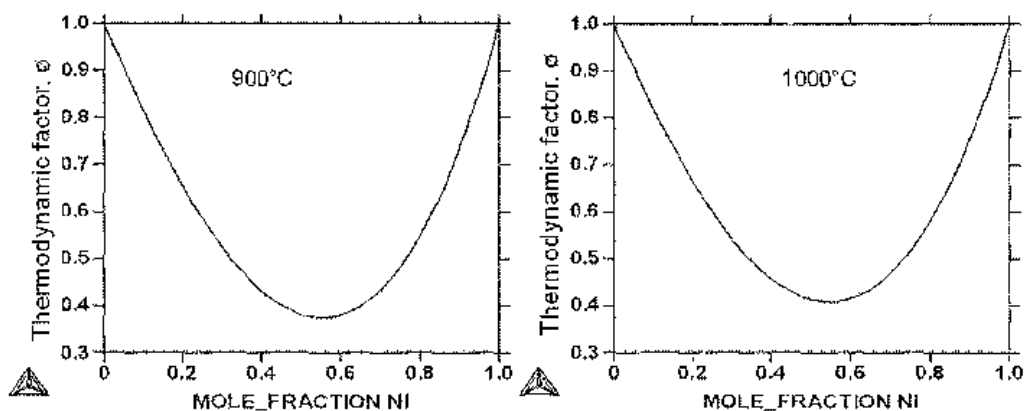


Figure 52. Calculated thermodynamic factor (ϕ) of the fcc phase of Ni-Cu alloy at 900°C and 1000°C (ThermoCalc/DICTRA database ssol4).

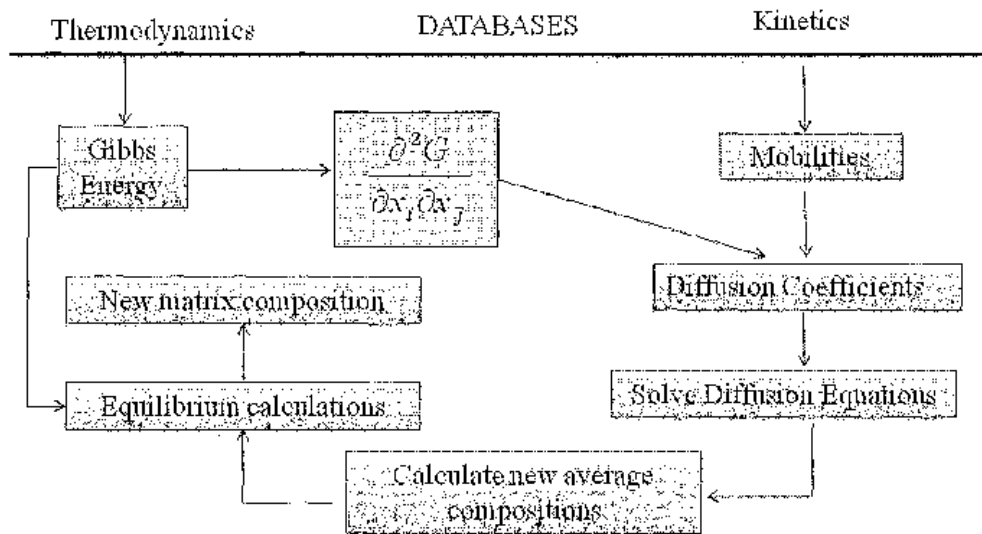


Figure 53. The calculation scheme in DICTRA for diffusion controlled transformation [62].

As mentioned above, kinetic data and thermodynamic data are required to calculate diffusivity in a multicomponent system. Figure 52 shows the calculated thermodynamic factor (ϕ) of the fcc phase of Ni-Cu alloy at 900°C and 1000°C using the ssol4 database in Thermocalc. DICTRA uses mobility parameters and thermodynamic factors to calculate interdiffusion coefficients. The calculation scheme in DICTRA is shown in Figure 53. DICTRA solves the PDEs of diffusion (Eqs. 40 and 33) and uses interdiffusion coefficients to obtain concentration profiles of the diffusing species. Hence, it is necessary to determine the appropriate mobility parameters. The PARROT module within DICTRA can be used to optimize mobility data. Experimentally obtained interdiffusivities or intrinsic diffusivities are used to optimize the mobility parameters. The self diffusion, tracer diffusion and interdiffusion coefficients discussed before were used in PARROT module to optimize the mobility parameters. The optimized parameters are shown in Table 8. DICTRA stores mobility parameters instead of diffusion

coefficients because it reduces the number of parameters to be stored. The mobility parameters shown in Table 8 were used in DICTRA as a kinetic database to simulate the concentration profiles of Ni-Cu diffusion couple. The kinetic database that can be read by DICTRA/ThermoCalc is shown in Appendix A.

Table 8. Assessed mobility parameter in the fcc Ni-Cu alloy

DICTRA notation	Mobility parameter	Parameter (J/mol)	Reference
Mobility of Ni			
MQ(FCC,Ni:Va;0)	Q_M^{Ni}	- 187000 - 69.8*T	[64]
MQ(FCC,Cu:Va;0)	Q_M^{Cu}	- 236400 - 68.32*T	[65]
MQ(FCC,Ni,Cu:Va;0)	$^0 A_M^{Ni,Cu}$	-114969 + 79.78*T	This work
Mobility of Cu			
MQ(FCC,Cu:Va;0)	Q_{Cu}^{Cu}	- 205872 - 82.51*T	[63]
MQ(FCC,Ni:Va;0)	Q_{Cu}^{Ni}	- 258153 - 81.25*T	[66]
MQ(FCC,Cu,Ni:Va;0)	$^c A_{Cu}^{Cu,Ni}$	- 101869 + 87.8*T	This work

The optimized mobility parameters (Table 8) were used in DICTRA to obtain interdiffusion coefficients and were compared with the experimental results. Figure 54 shows the schematic of the diffusion bonding setup in DICTRA. The problem setup file used in DICTRA is shown in Appendix A. The interlayer is placed in between two base metals to be bonded (top image). Only half of the joint was modeled because of the symmetry of the joint (bottom image). The integration points in each region were assumed to be linearly distributed. The input parameters were temperature, time, heating and cooling rate, composition and phase of the Ni-Cu diffusion couple. To initiate the calculation, the interlayer region was set with a 'seed' of .1 wt. % base metal in it and the base metal was set with a 'seed' of .001 wt. % of interlayer. This seed is sometimes helpful to allow for numerical convergence. Figure 55 shows the comparison of the

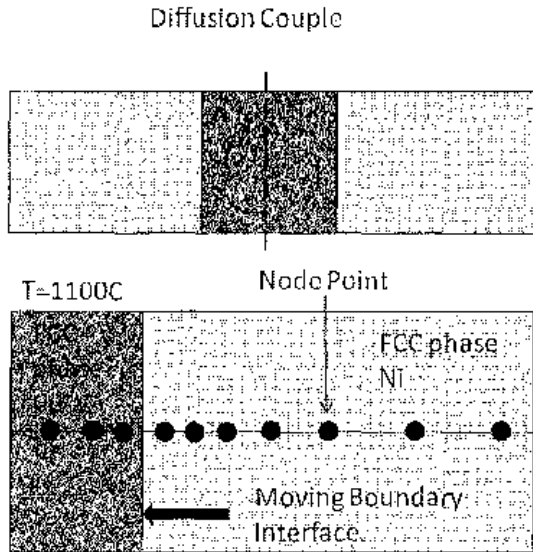


Figure 54. Schematic of problem setup in DICTRA.

calculated and experimental [68] interdiffusion coefficient of Ni-Cu alloy at 1000°C. The calculated data matched with the experimental values quite well.

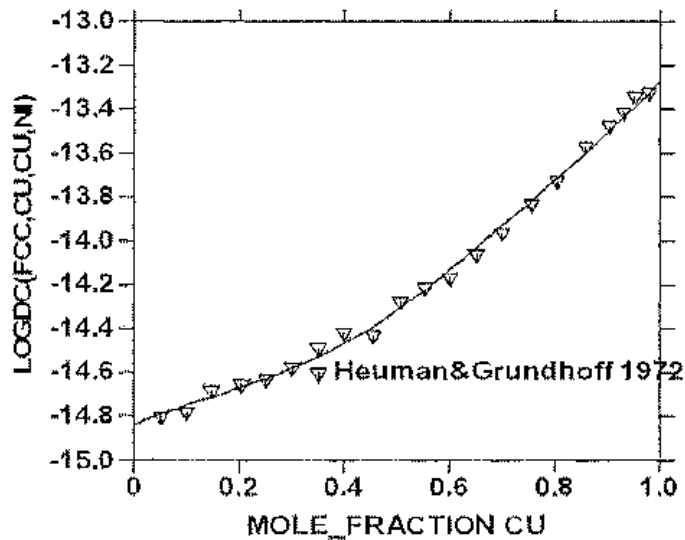


Figure 55. Experimental [68] and calculated interdiffusion coefficient of Ni-Cu system at 1000°C.

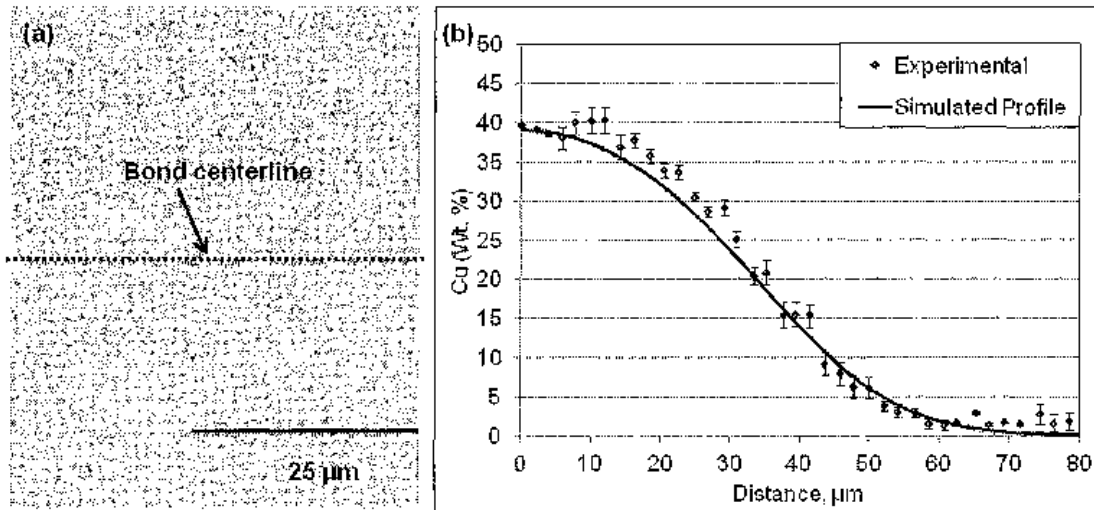


Figure 56. (a) SEM image of diffusion bonded Ni using Cu interlayer (25µm) at 1050°C for 15h and (b) concentration profile of Cu from the bond centerline to the interior of base metal.

Figure 56 shows (a) SEM image of diffusion bonded Ni using Cu interlayer (25 µm) at 1050°C for 15 h and (b) concentration profiles of Cu from the bond centerline to the interior of the base metal. The microstructure of the joint is not distinguishable from the base metal. This is because Ni and Cu form a solid solution in any composition range. The experimental concentration profile indicated that the joint centerline contained approximately 39 wt. % Cu after 15 h bonding time and gradually decreased to the interior of the base metal. The calculated and the experimental concentration profiles of Cu agree well with each other. However, DICTRA tends to predict slower diffusion rates than observed experimentally.

Figure 57 shows (a) SEM image of diffusion bonded Ni using Cu interlayer (25µm) at 1070°C for 10 h and concentration profile of Cu from the bond centerline to the interior of base metal. The microstructure of the bond centerline was similar to the microstructure

obtained for previous conditions. The joint centerline contained 40 wt. % Cu with Cu content gradually decreasing away from joint centerline. The calculated and the experimental concentration profiles of Cu agreed quite well with each other, showing better agreement between experimental and calculated profiles than at 1050°C.

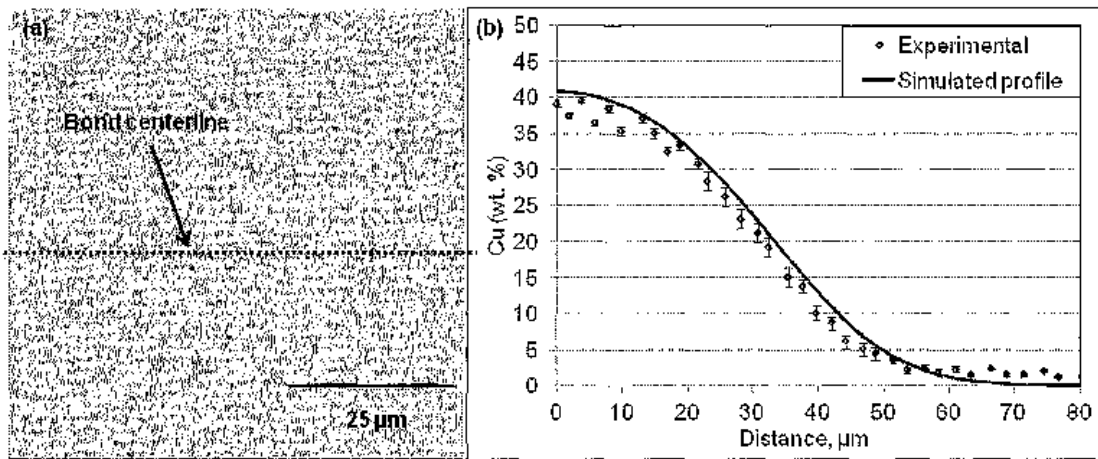


Figure 57. (a) SEM image of diffusion bonded Ni using Cu interlayer (25µm) at 1070°C for 10 h and (b) concentration profile of Cu from the bond centerline to the interior of base metal.

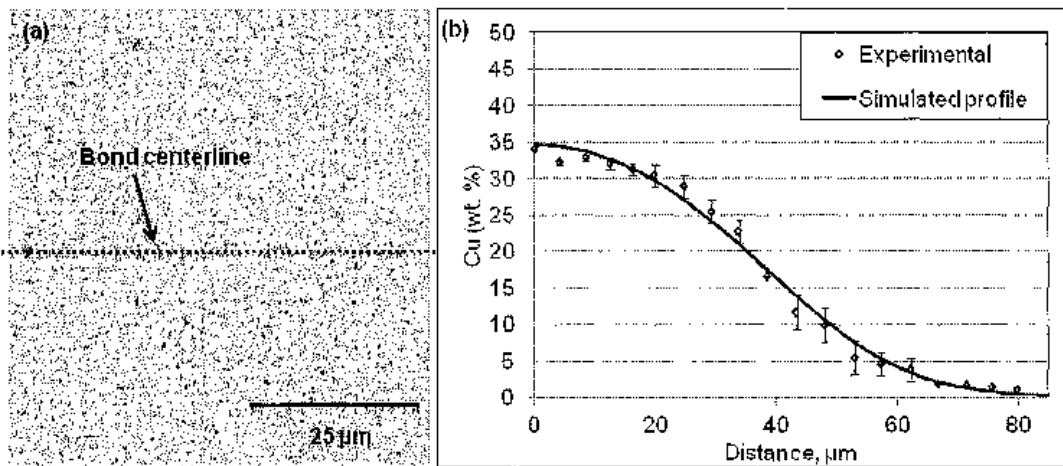


Figure 58. SEM image of diffusion bonded Ni using Cu interlayer (25µm) at 1100°C for 10 h and concentration profile of Cu from the bond centerline to the interior of base metal.

Figure 58 shows (a) the SEM image of diffusion bonded Ni using Cu interlayer (25 μm) at 1100°C for 10 h and (b) concentration profiles of Cu from the bond centerline to the interior of the base metal. The microstructure of the joint centerline contained ~ 34 wt. % Cu with Cu content gradually decreasing into the base metal. By increasing the bonding temperature from 1050 to 1100°C, the Cu content in the bond centerline after 10 h decreased from 39 to 34 wt. %. The calculated concentration profile matched very well with the experimental profile at these conditions. Improved agreement from 1050°C to 1100°C is likely due to the suppression of grain boundary contribution to the overall diffusion. Grain boundary diffusion is observed in Cu-Ni system below 1054°C [66]. Hence, there is a mismatch between calculated and experimental profiles at 1050°C; however, the mismatch has been minimized at higher temperature (1100°C). The mass conservation in DICTRA has been verified and it was found out that DICTRA overestimated by about 0.713 wt. % the starting amount of Cu (8.458 wt. %).

Ni-Al Binary System

Ni-Al binary system has several intermetallics such as AlNi, Al₃Ni, Al₃Ni₂, and Al₃Ni₅. Al₃Ni₅ does not exist above 700°C, Al₃Ni and Al₃Ni₂ do not exist above 852°C and 1227°C, respectively. AlNi exists at high temperature and its melting point is higher than both Al and Ni. The diffusion mobilities in those intermetallics are not available except AlNi which is used as a diffusion barrier. AlNi has two different crystalline structures such as disordered BCC (DICTRA notation - BCC_DIS) and ordered BCC (DICTRA notation - B2_ORD). The diffusion mobility parameter of Al and Ni in fcc phase Ni-Al alloy (Ni-20 at.% Al) has been taken from DICTRA example g2 [70]. In this example, the mobility parameters have been optimized using the interdiffusion coefficient

determined by Yamamoto et al. [71]. The diffusion in B2-BCC phase has been optimized by Helander et al. [72]. The thermodynamic database has been obtained from DICTRA example il [70].

Figure 59 shows the concentration profile of Al from the bond centerline of diffusion bonded Ni using Al interlayer (100 μm) at 800°C for 10 h. The centerline consists of 35 wt. % Al which is closed to the composition of AlNi (31.5 wt. % Al). Then it sharply decreased to 30 wt.% Al and gradually decreased to base metal composition. However, experimental information provided slightly different results. Figure 35 from Chapter 2

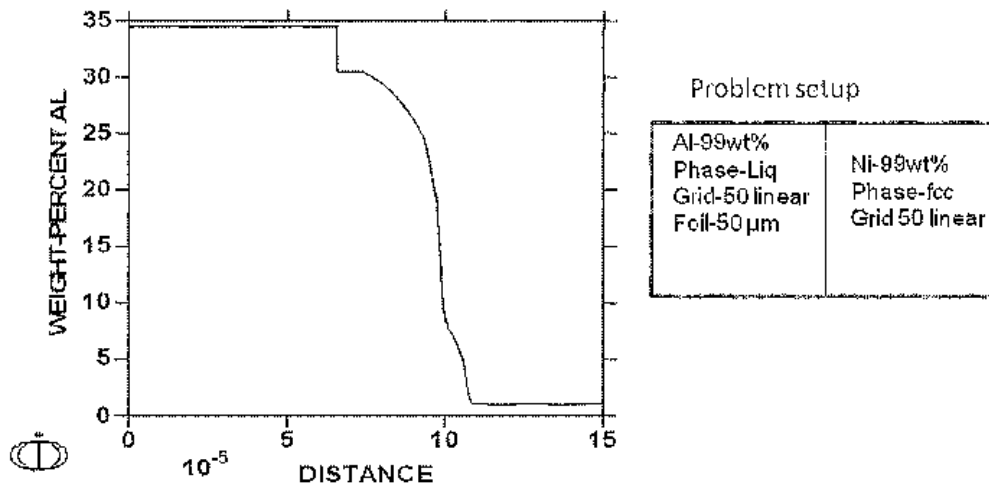


Figure 59. Concentration profile of Al in Ni-Al diffusion couple at 800°C for 10h, interlayer thickness: 100 μm .

shows the SEM image of diffusion bonded Ni using Al interlayer. The bond centerline contained 42-47 wt% Al which extended to a distance of 45 μm from the centerline. The composition of this region is closest to that of Al_3Ni_2 (40 wt. % Al). Then it decreased sharply to 32 wt% Al (closest to the composition of NiAl), 17 wt% Al and trace amount

of Al, respectively. The next modeling was done using thinner foil (25 μm) keeping all other parameters fixed. The concentration profile of Al in Al-Ni diffusion couple is

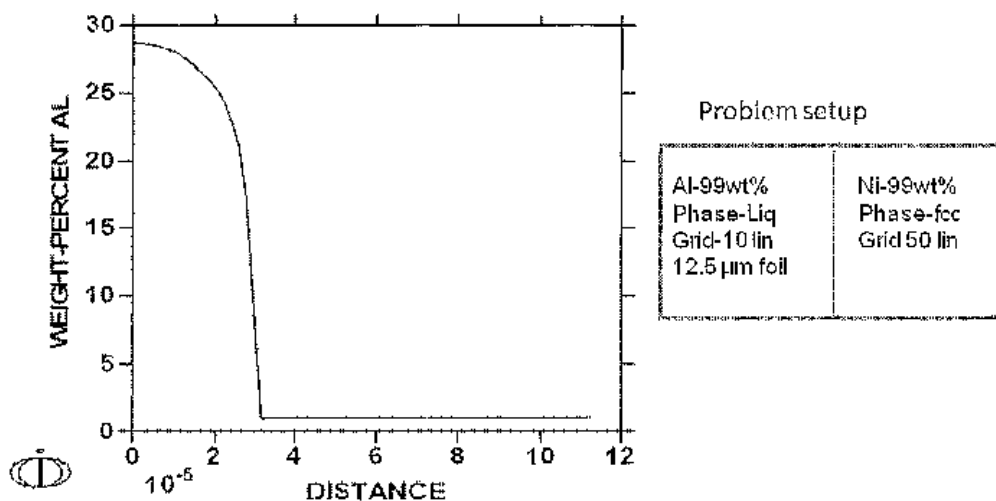


Figure 60. Concentration profile of Al in Ni-Al diffusion couple at 800°C for 10h, interlayer thickness 25 μm .

shown in Figure 60. The joint centerline consists of ~ 28 wt. % of Al and then gradually decreased. The B2-BCC phase in Al-Ni system contains approximately 31.5 wt% Al at room temperature. This phase occurs over a composition range depending on the temperature. This profile indicates that the B2-BCC phase and other intermetallics can be disappeared as diffusion progresses. However, concentration profile from the experiment (Figure 39) did not match the simulated profile.

Ni-(Au-12Ge) Ternary System

Diffusion bonding of Ni was performed using Au-12Ge interlayer. The calculated concentration profiles of Au and Ge in Ni-(Au-12Ge) diffusion couple obtained at 900°C for 10 h are shown in Fig. 61. SSOL4 thermodynamic database and Mob2 kinetic

database were used for this calculation. However, the calculated profiles are significantly different than their experimental counterparts. The reason is that the Mob2 database does not have the proper mobility data for this system. The mobility data for this Ni-Au-Ge ternary system needs to be optimized.

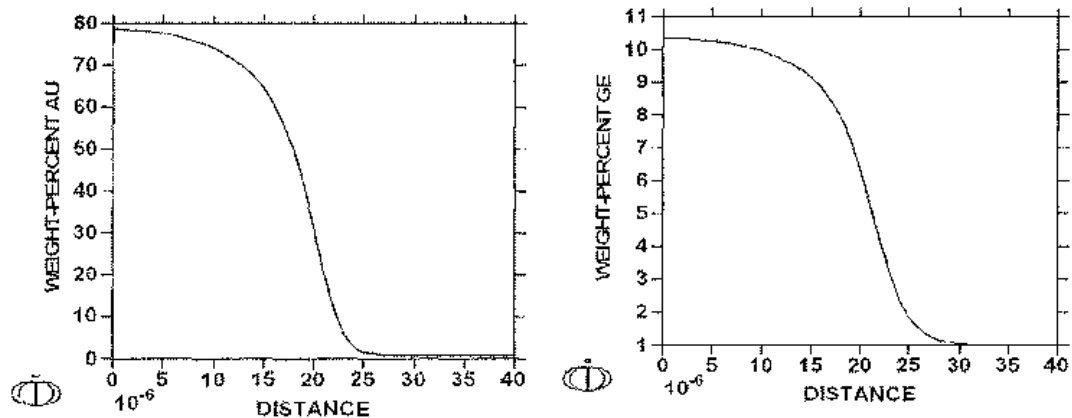


Figure 61. Concentration profiles of Au and Ge in Ni-(Au-Ge) diffusion couple at 900°C for 10h, interlayer thickness: 100 μm .

Conclusions

DICTRA/Thermocalc software has been successfully used to simulate the concentration profiles of Cu and Ni in a Cu-Ni diffusion joint. DICTRA also can optimize the mobility parameters from experimental diffusion data. The interdiffusion coefficient calculated from the optimized mobility parameter agreed well with the experimental data. The simulated profile obtained at 1100°C agreed very well with experimental profile. Some discrepancies were observed between simulated and experimental profile obtained at 1050°C. This is probably due to grain boundary diffusion occurred at this temperature. This problem may be able to be overcome by introducing the grain boundary diffusion into the database or introducing an effective diffusivity. For Ni-Al binary and Ni-(Au-

12Ge) ternary system the simulated profiles did not match with the simulated profiles because of the lack of proper mobility and thermodynamic database.

CHAPTER IV

TLP BONDING OF INDUSTRIALLY-IMPORTANT ALLOYS

Specimen Fabrication

SS 321 Joints

Stainless steel 321(SS 321) rods 6.35 mm in diameter and ~8 mm in length were used for transient liquid phase diffusion bonding and subsequent microstructural examination. The samples were polished to a 1200 grit finish and the surfaces were cleaned in an ultrasonic bath using isopropyl alcohol and stored in alcohol before bonding. The samples for tensile testing had a gauge length of 59 ± 0.5 mm and a diameter of 9.0 ± 0.1 mm in the gauge section. The diffusion bonding was done with commercially pure copper (99.999% pure, Alfa Aesar, USA), Au-20Sn or Au-12Ge (Alfa Aesar, USA) interlayers. The samples to be bonded were held in a jig made of Kovar under static pressure and placed in a tube furnace. Schematics of the diffusion bond geometry and diffusion bonded samples are shown in Fig. 1. The heating chamber was repeatedly evacuated and filled with argon gas 10 times to make it oxygen-free. The bonding was performed under either vacuum or argon atmosphere. An oxygen trap was used in the line of argon flow into the heating furnace. SS 321 joints with Au-12Ge interlayers (100 μm) were bonded at 900-1050°C for 1-20 h, with Au-20Sn (100 μm) interlayers at 750-800°C for 10 h and with Cu (25 μm) interlayers at 1100°C for 10 h. The joining temperatures were chosen based on the interlayer melting temperature and binary phase diagrams between major

alloying elements and interlayer elements. Metallographic samples were mounted in epoxy resin. Longitudinal sections were polished down to approximately half of the diameter for microstructural observation.

Inconel 718 Joints

Inconel 718 was diffusion bonded using Cu (25 μm) or Au-12Ge (100 μm) interlayers. The bonding temperatures and time used were 1050-1150°C and 5-15 h for Cu interlayers. For the Au-12Ge interlayers, the bonding conditions were 950-1050°C temperature and 15-20 h time. The bonding was done under vacuum. Bonding conditions were chosen based on the interlayer melting temperature and phase diagrams between main alloying elements in the interlayer and base alloy. Kovar jigs were used to bond both tensile specimens and specimens for microstructural analysis. Metallographic samples were mounted in epoxy resin then polished down to approximately half of the sample diameter for microstructural observation. The tensile specimen had a gauge length of 30 ± 0.1 mm and a diameter of 6 ± 0.1 mm.

Ti-6Al-4V Joints

Ti-6Al-4V (grade 5 Ti alloy, named as Ti-5) was diffusion bonded using Cu interlayers (25 μm). The bonding surfaces were polished to a 600 grit finish. Joining was performed in argon or under vacuum. Grade 2 Ti alloy jigs were used to keep the thermal expansion mismatch to a minimum. Metallographic samples were mounted in epoxy resin before polishing. Then the samples were polished down to approximately half of the diameter for microstructural observation. The tensile specimen had a gauge length of 30 ± 0.1 mm and a diameter of 6 ± 0.1 mm.

Microstructural Characterization

Scanning electron microscopy (SEM) observations of bonded samples were carried out using a Hitachi S-3400N scanning electron microscope (SEM) and the compositions and different phases in the bonded zone were analyzed by energy dispersive spectrometry (EDS).

Mechanical Properties

To determine the mechanical properties of the bonded specimen, uniaxial tensile tests were performed using a screw-driven AG-IS 50 kN universal testing machine (Shimadzu) with a cross head speed of 1 mm/min. Cylindrical tensile specimens were prepared according to the ASTM standard E 8M-99. For each data point the average of three specimens were used.

Results and Discussion

TLP Bonding of SS 321

Microstructure

The alloy Au-12 wt. % Ge (Au-12Ge) is a high temperature solder alloy [13]. The melting temperature of this alloy is 361°C. The foil of this alloy was used as an interlayer to bond SS 321. The compositions of the base alloy (SS 321) are shown in Table 9.

Table 9. Compositions (wt. %) of AISI type stainless steel 321 (SS 321).

Fe	Cr	Ni	Mn	Si	Ti	C	S	P
Bal.	17-19	9-12	2	1	5x % (C+N) - .7	.08	.03	.045

Figure 62 shows SEM images of diffusion bonded SS 321 using Au-12Ge interlayer (100 μm) at 900°C for 1 h in vacuum with slow cooling (4°C/min or slower). Most of the interlayer diffused into the base material at these joining conditions. The thickness of the residual interlayer obtained was $\sim 5.8 \mu\text{m}$. The compositions found in the residual interlayer were 78.4 wt. % Au, 6.4 wt. % Fe, 1.6 wt. % Ni, 6 wt. % Cr and no Ge with small amount of other alloying elements. The composition found at the interface on the base metal side was 25.3 wt. % Au, 4.1 wt. % Ge, 44.7 % Fe, 7.4 % Ni and 14.7 wt. % Cr.

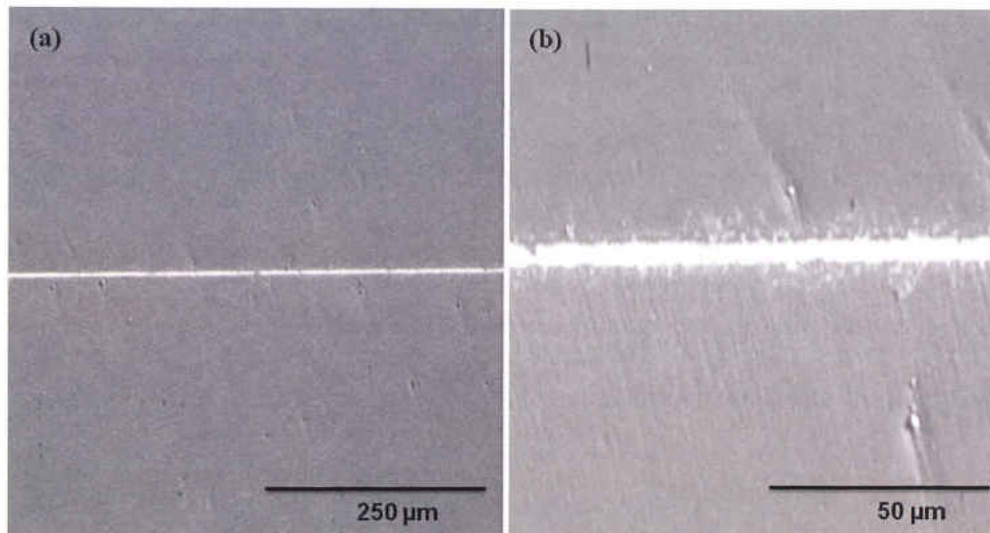


Figure 62. (a) SEM image of diffusion bonded SS 321 using Au-12Ge interlayer (100 μm) at 900°C for 1 h and (b) magnified image of (a).

Figure 63 shows SEM images of diffusion bonded SS 321 using Au-12Ge interlayer (100 μm) at 950°C for 10 h in vacuum with slow cooling (4°C/min or slower). The joint centerline microstructure consisted of residual interlayer and Au-rich particles near the interlayer/base metal interface. The thickness of the residual interlayer found was $\sim 5.5 \mu\text{m}$ with a composition of 79.3 wt. % Au, 5.3 wt. % Fe, 1.5 wt. % Ni, 4.2 wt. % Cr, 3 wt.

Figure 62 shows SEM images of diffusion bonded SS 321 using Au-12Ge interlayer (100 μm) at 900°C for 1 h in vacuum with slow cooling (4°C/min or slower). Most of the interlayer diffused into the base material at these joining conditions. The thickness of the residual interlayer obtained was $\sim 5.8 \mu\text{m}$. The compositions found in the residual interlayer were 78.4 wt. % Au, 6.4 wt. % Fe, 1.6 wt. % Ni, 6 wt. % Cr and no Ge with small amount of other alloying elements. The composition found at the interface on the base metal side was 25.3 wt. % Au, 4.1 wt. % Ge, 44.7 % Fe, 7.4 % Ni and 14.7 wt. % Cr.

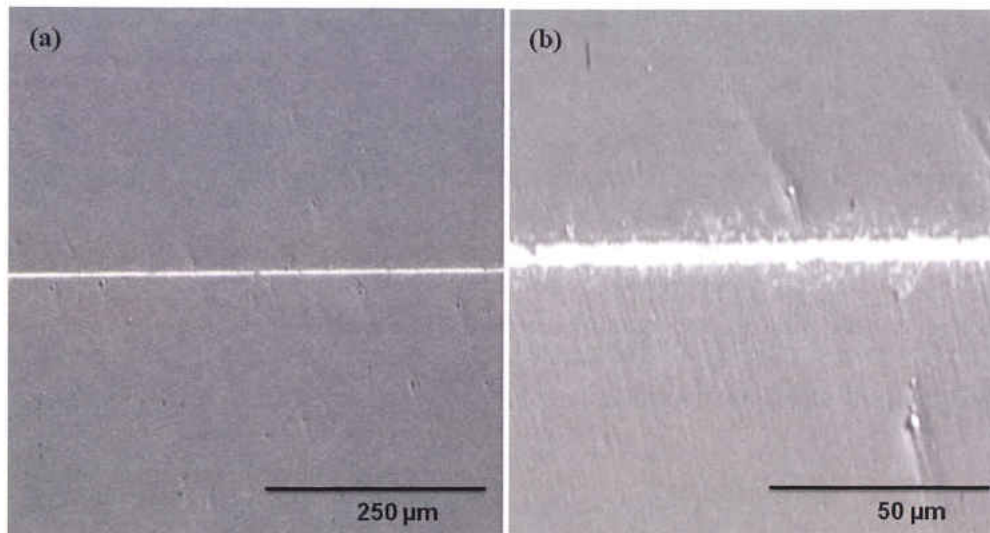


Figure 62. (a) SEM image of diffusion bonded SS 321 using Au-12Ge interlayer (100 μm) at 900°C for 1 h and (b) magnified image of (a).

Figure 63 shows SEM images of diffusion bonded SS 321 using Au-12Ge interlayer (100 μm) at 950°C for 10 h in vacuum with slow cooling (4°C/min or slower). The joint centerline microstructure consisted of residual interlayer and Au-rich particles near the interlayer/base metal interface. The thickness of the residual interlayer found was $\sim 5.5 \mu\text{m}$ with a composition of 79.3 wt. % Au, 5.3 wt. % Fe, 1.5 wt. % Ni, 4.2 wt. % Cr, 3 wt.

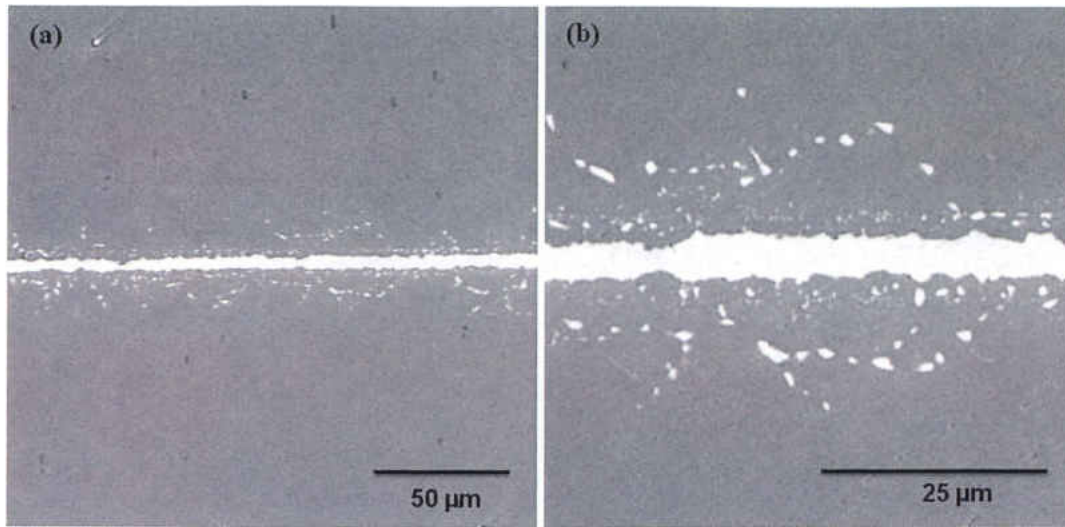


Figure 63. (a) SEM image of diffusion bonded SS 321 using Au-12Ge interlayer (100 μm) at 950°C for 10 h and (b) magnified image of (a).

% Mn and no Ge. According to the SEM image, the Au-rich particles seemed to be aligned along the grain boundaries of the base alloy. It is noticeable that even though the bonding temperature and time were increased the overall interdiffusion was not increased appreciably. The residual interlayer ($\sim 5.5 \mu\text{m}$) obtained was little thinner than obtained with previous bonding conditions.

Figure 64 shows SEM images of diffusion bonded SS 321 using Au-12Ge interlayer at 1010°C for 15 h in vacuum with slow cooling. The bond centerline microstructure did not change appreciably compared to the previous conditions. The centerline microstructure consisted of residual interlayer and Au-rich particles near the interlayer/base metal interface. The thickness of the residual interlayer obtained was 3-3.5 μm . According to the SEM image, the Au-rich particles appeared to precipitate along the grain boundaries of base metal. The composition of the residual interlayer obtained was 83.9 wt. % Au, 3.5

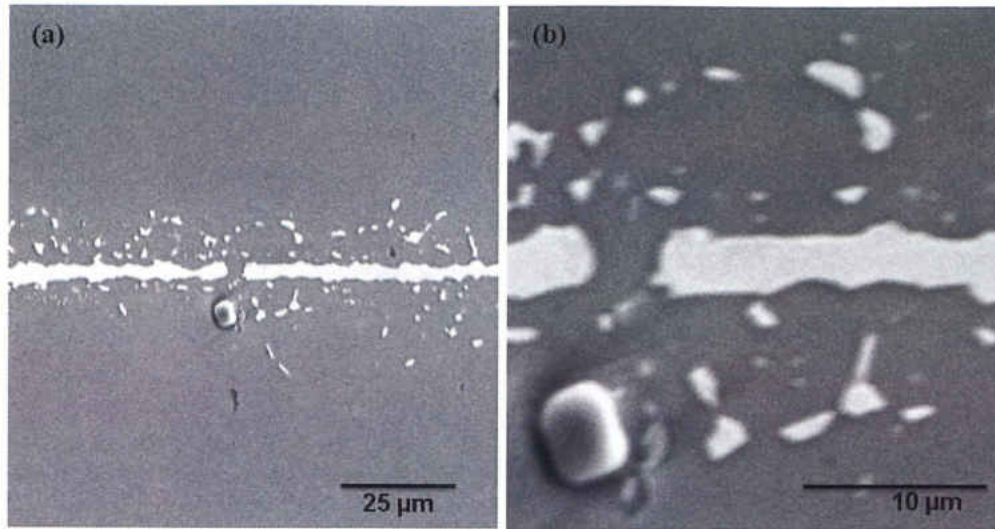


Figure 64. (a) SEM image of diffusion bonded SS 321 using Au-12Ge interlayer at 1010°C for 15 h and (b) magnified image of (a).

% Fe, 0.85 wt. % Ni, 3.25 wt. % Cr, 5.5 wt. % Mn and no Ge. The amount of Mn found in the residual interlayer was more than the Mn content in base alloy (2 wt. %).

Since the residual interlayer is not desirable in the joint centerline, the joining temperature was increased to 1050°C to enhance interdiffusion. Figure 65 shows SEM images of diffusion bonded SS 321 using Au-12Ge interlayer at 1050°C for 15 h in vacuum with slow cooling. The bond centerline consisted of residual interlayer and Au-rich particles. The residual interlayer had a composition of 78.3 wt. % Au, 3.1 wt. % Fe, 1.7 wt. % Ni, 3.3 wt. % Cr, 6.0 wt. % Mn and no Ge. The thickness of the residual interlayer found was ~3.8 μm which was 8.6 % thicker than the one that was obtained for previous bonding conditions. Some of the Au-rich particles grew bigger and precipitated away from the residual interlayer. Their number was also reduced compared to previous conditions. Changing the bonding temperature and time from 900 to 1050°C and 1h to 15 h, respectively, the residual interlayer decreased from 5.8 μm to 3.8 μm. The diffusion

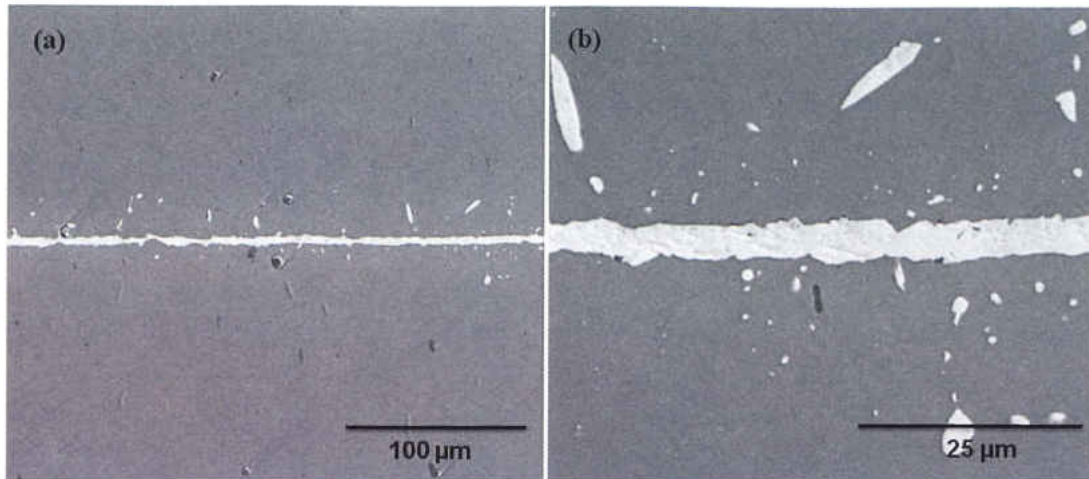


Figure 65. (a) SEM image of diffusion bonded SS 321 using Au-12Ge interlayer at 1050°C for 15 h and (b) magnified image of (a).

was not increased appreciably or the diffusing elements diffused back during cooling process. This idea of back-diffusion can be explained referring the Au-Fe phase diagram (Figure 28). The solubility of Fe in Au and Au in Fe is very small at room temperature compared to the bonding temperature. During cooling time both Fe and Au solid solutions become supersaturated. As a result, excess Au can come out of the solution and diffuse back preferentially at the centerline of the bonding area or precipitate at the grain boundary. A faster cooling rate might reduce or eliminate this back-diffusion because the atoms might not get enough time to diffuse. Other elements available in the system might also affect the interdiffusion and back-diffusion.

To prevent possible back-diffusion, a faster cooling process was applied. Figure 66 shows SEM images of diffusion bonded SS 321 using Au-12Ge interlayer at 1050°C for 15 h in vacuum, cooled in air. The interlayer was diffused completely in some areas and it was retained in some areas. The faster cooling seemed to prevent back diffusion. Spherical

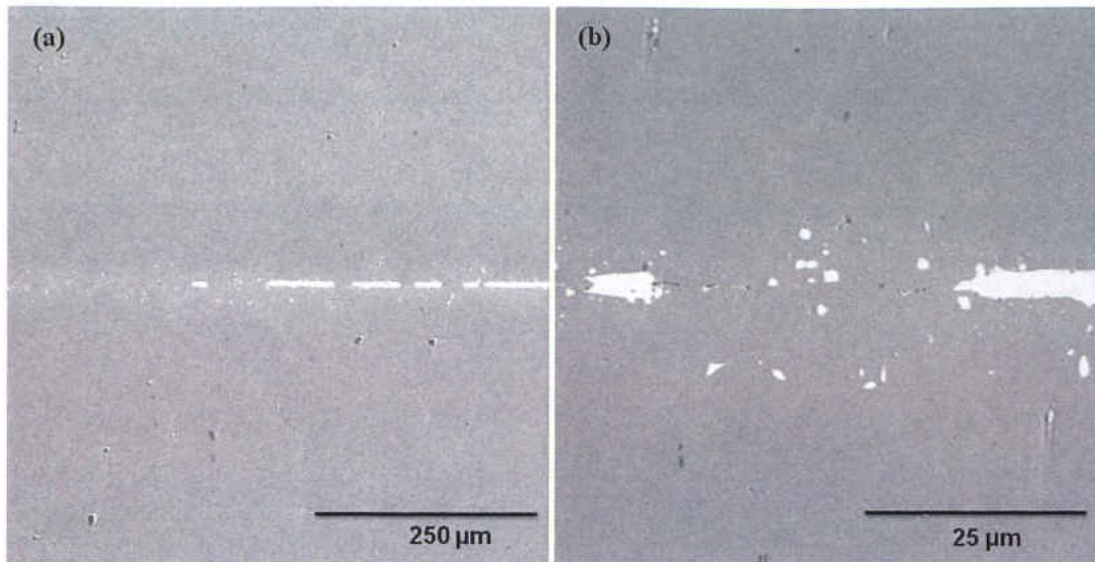


Figure 66. (a) SEM image of diffusion bonded SS 321 using Au-12Ge interlayer at 1050°C for 15 h in vacuum with cooling in air and (b) magnified image of (a).

Au-rich particles were observed near the bond centerline along the whole cross-section. The size of these particles was much smaller than was observed in previous conditions where a slower cooling process was applied. The coarsening of these particles was prevented by fast cooling. The composition of the residual interlayer was 75 wt. % Au, 5.4 wt. % Fe, 2.0 wt. % Ni, 3.9 wt. % Cr, 7.4 wt. % Mn and no Ge. The compositions in the bond centerline, where no residual interlayer was found, were ~10 wt. % Au, 62 wt. % Fe, 15.6 wt. % Cr, 8 wt. % Ni, 0.28 wt. % Mn and 1.9 wt. % Ge.

To get rid of residual interlayer from the joint centerline, the joining time was increased to 20 h and the cooling rate was increased by quenching in water. Figure 67 shows SEM images of diffusion bonded SS 321 at 1050°C for 20 h using Au-12Ge interlayer in vacuum, quenched in water. The bond centerline microstructure consisted of Au-rich

particles and near continuous microcracks which ran through the entire cross section.

EDS spot analysis on the black line in the joint centerline provided 8.7 wt. % C, 28.2 wt.

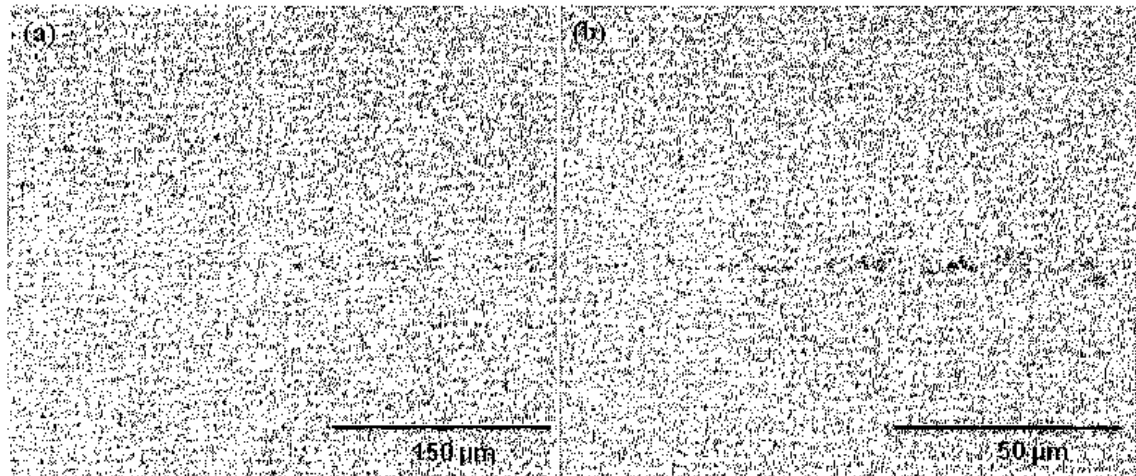


Figure 67. (a) SEM image of diffusion bonded SS 321 at 1050°C for 20 h using Au-12Ge interlayer in vacuum and quenched in water and (b) magnified image of (a).

% O, 43.1 wt. % Al, 8.9 wt. % Ti and small amounts of other alloying and interlayer elements while the base alloy had only .08 wt. % C, .4-.7 wt. % Ti and no Al. This analysis indicated that high percentages of Al, O and C appeared from polishing media such as diamond paste and γ -Al₂O₃; Ti appeared possibly from TiC. These polishing media might have been trapped in the microcracks during polishing. The microstructures in the joint centerline other than microcracks contained 59.5 wt. % Fe, 15.3 wt. % Cr, 8 wt. % Ni, 10 wt. % Au, 3.1 wt. % Ge and .3 wt. % Mn with trace amounts of other alloying elements.

Figure 68 shows SEM images of diffusion bonded SS 321 using Au-12Ge interlayer at 1050°C for 20 h in vacuum, cooled in flow of water. The microstructure of the bond centerline consisted of Au-rich particles in the matrix of base metal and discontinuous

microcracks. The black particles observed in the joint centerline microstructures were γ - Al_2O_3 , C or TiC which were confirmed by EDS analysis. Al_2O_3 and C were the

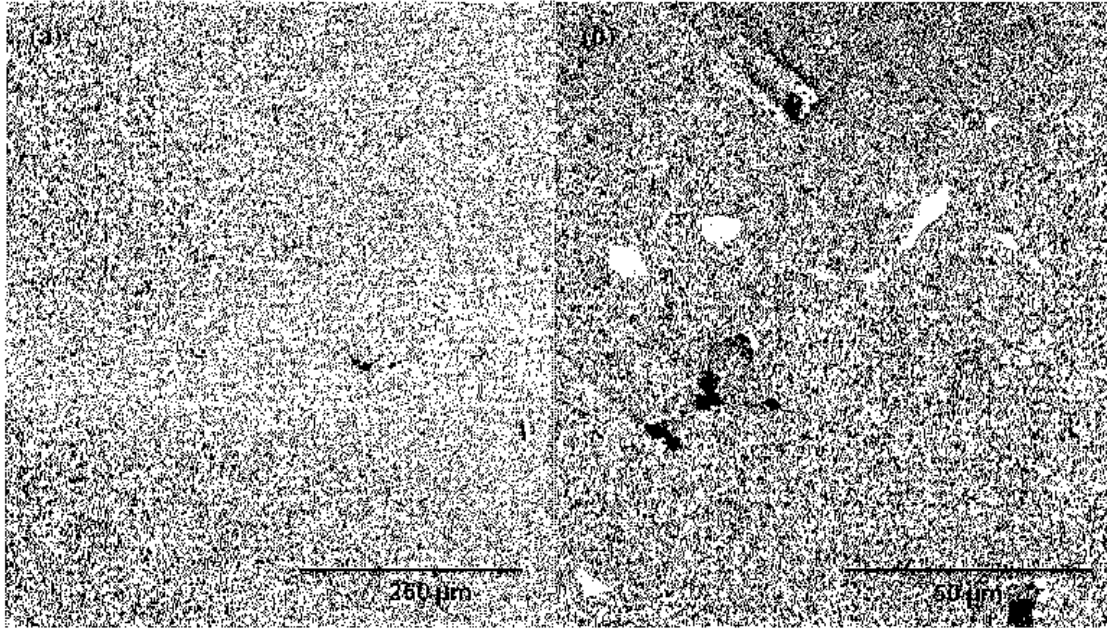


Figure 68. (a) SEM image of diffusion bonded SS 321 using Au-12Ge interlayer at 1050°C for 20 h in vacuum, cooled in flow of water and (b) magnified image of (a).

contaminations from polishing media (Al_2O_3 and diamond paste). TiC was formed during the heating process applied for diffusion bonding. Au-rich particles in the joint centerline were bigger and more numerous than were found with water-quenched sample. Also, the microcracks have been reduced significantly. Ti is added to SS 321 to prevent the formation of chromium carbide at elevated temperature. Formation of chromium carbide depletes Cr from the grain boundary, which, in turn, leads to grain boundary corrosion.

Figure 69 shows SEM images of diffusion bonded SS 321 using Au-12Ge interlayer at 1050°C for 20 h in vacuum, air-cooled. At these joining conditions no residual interlayer

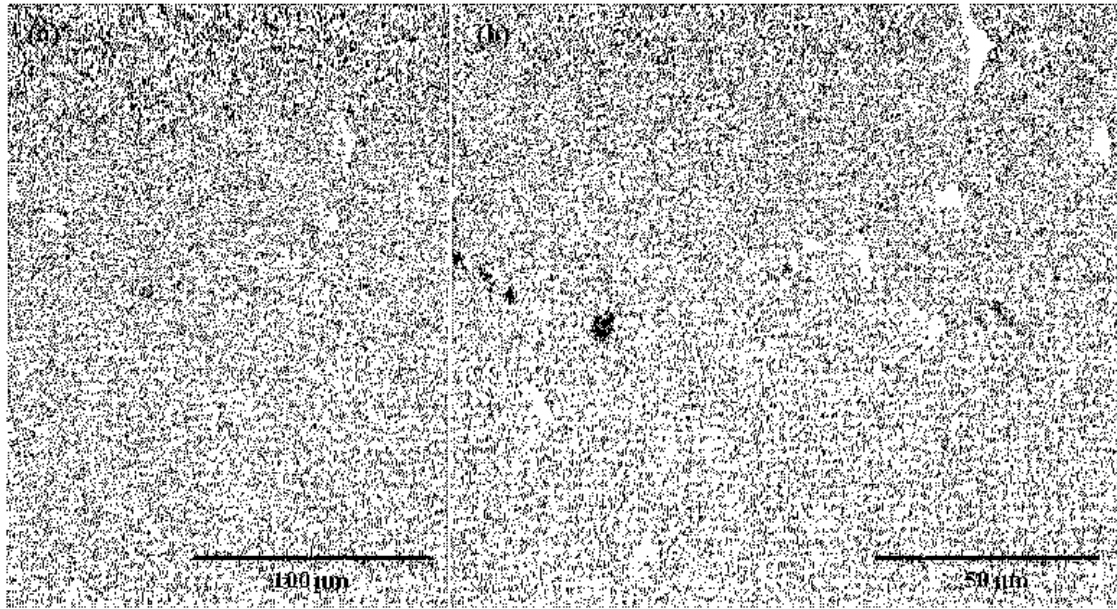


Figure 69. (a) SEM image of diffusion bonded SS 321 using Au-12Ge interlayer at 1050°C for 20 h in vacuum and air-cooled and (b) magnified image of (a). Image was taken from the center of the sample.

was found in the joint area. The microstructure of the joint centerline consisted of a matrix of base alloy with Au-rich particles along the grain boundaries as well as in the grain areas. No microcracks were found in the bonded area. The size of the Au-rich particles along the grain boundary was much bigger than the ones in the grain areas. The bond centerline microstructure consisted of 17 wt. % Au, 47 wt. % Fe, 16 wt. % Cr, 7 wt. % Ni, 3.8 wt. % Ge and 1.8 wt. % Mn. The Au-rich particles contained 70-72 wt. % Au, 8-11 wt. % Mn, 5 wt. % Fe, 2.5 wt. % Cr and 1.1 wt. % Ni. The black particles observed were Al_2O_3 , possibly contamination from polishing media.

Figure 70 shows a SEM image of diffusion bonded SS 321 using Au-12Ge interlayer at 1050°C for 20 h in vacuum, cooled in air (image was taken from the edge of the sample). Black oxide particles observed along the joint centerline. According to EDS analysis, the joint centerline contained 39.4 wt. % O, 11 wt. % Ti, 13 wt. % Mn and small percentages

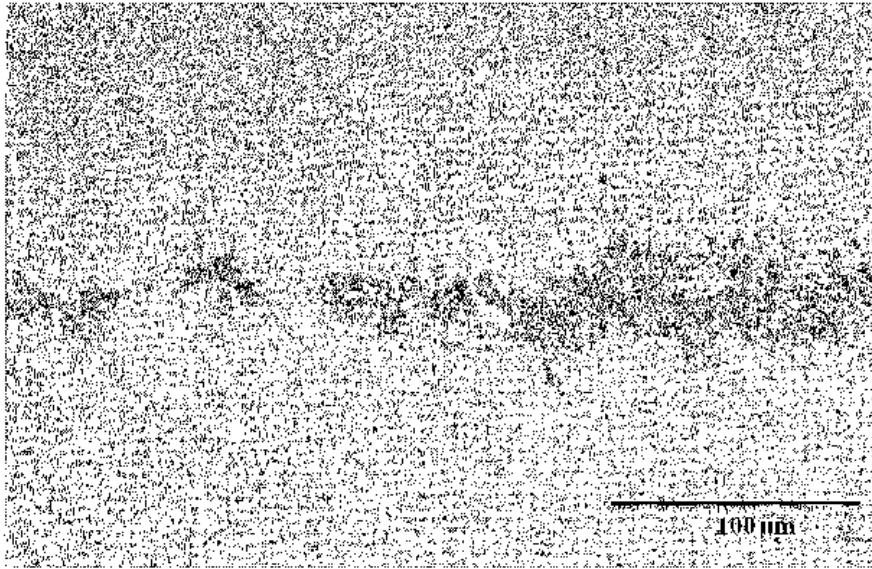


Figure 70. SEM image of diffusion bonded SS 321 using Au-12Ge interlayer at 1050°C for 20 h in vacuum and air-cooled, image taken from the edge of the sample.

of other alloying elements. These oxide particles extended over 200 to 400 μm from the surface to the interior. The oxidation occurred because the environment of the joining chamber possibly was not properly controlled.

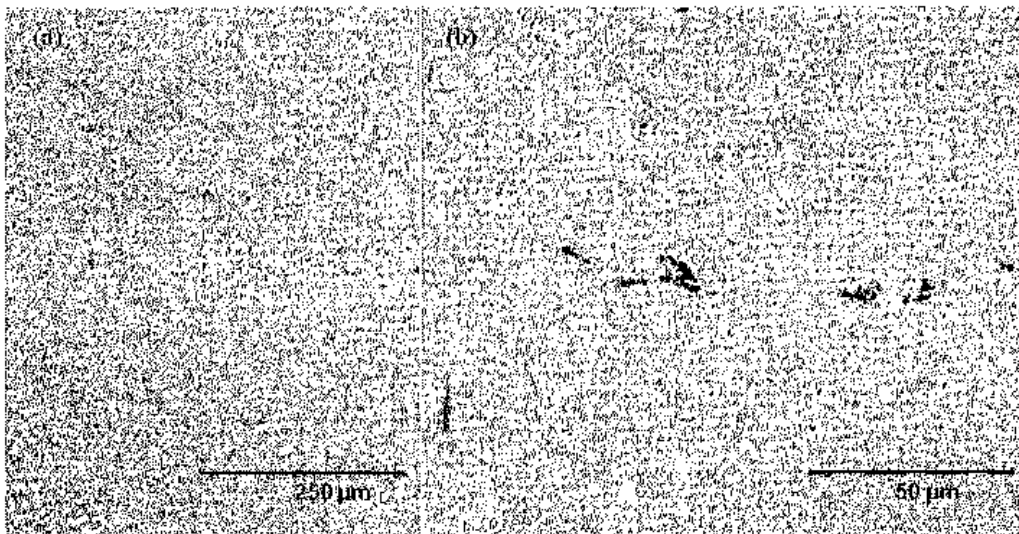


Figure 71. (a) SEM image of diffusion bonded SS 321 using Au-12Ge interlayer at 1050°C for 20 h in argon and cooled in air and (b) magnified image of (a).

Figure 71 shows SEM images of diffusion bonded SS 321 using Au-12Ge interlayer at 1050°C for 20 h in argon and cooled in air. The joint centerline microstructure consisted of Au-rich particles in matrix of base alloy and some black particles. The composition of the joint centerline was 62.3-63.4 wt. % Fe, 15.2-15.6 wt. % Cr, 8-8.6 wt. % Ni, 6.4-7.3 wt. % Au, 2.7-3.1 wt. % Ge, and .7 wt. % Mn. The Au-rich particles contained 68.1 wt. % Au and 14.3 wt. % Mn, 5.6 wt. % Fe, 3.3 wt. % Cr with other alloying elements. The composition of the black particles was varied from 22-59 wt. % Ti, 6.9-37.6 wt. % Al, 9-22 wt. % O, 6.4- 9 wt. % C, 4.8-11 wt. % Au, 1.4-2.5 wt. % Fe, .7-1.1 wt. % Cr and small amount of other alloying elements. These analyses indicated that the particles were possibly γ -Al₂O₃, TiC formed during diffusion joint and C from diamond paste and TiC.

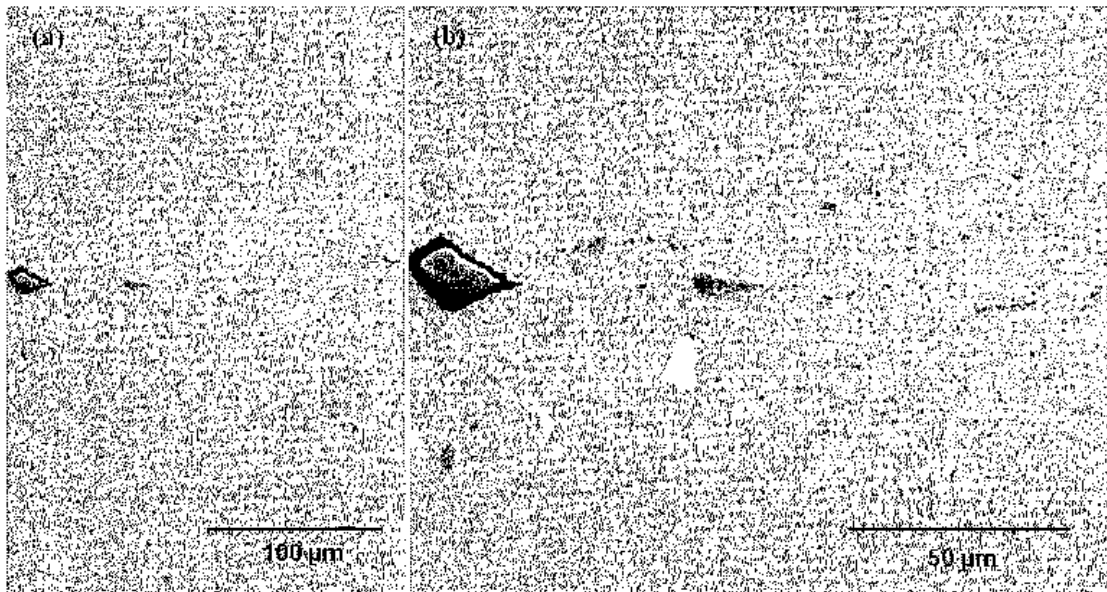


Figure 72. (a) SEM image of diffusion bonded SS 321 using Au-12Ge interlayer at 1050°C for 20 h, bonded in argon, cooled in flow of water and (b) magnified image of (a).

Figure 72 shows SEM images of diffusion bonded SS 321 using Au-12Ge interlayer at 1050°C for 20 h, bonded in argon, cooled in flow of water. The joint centerline

microstructure consisted of Au-rich particles in the matrix of base alloy, near continuous microcracks along the joint centerline and some black particles, possibly contamination from polishing media. The EDS analysis of these black particles provided 42-59 wt. % Al, 26.8-33.5 wt. % O, 1.3 wt. % C, 3.3 wt. % Au and small amount of other alloying elements. Few very small black spots had higher amount of Ti and C with other elements, these were possibly TiC.

Table 10. Summary of the microstructure of TLP bonded SS 321 using Au-12Ge bonded at 1050°C for 20 h with different environment and cooling method.

	Bonding Atmosphere	Cooling method	Microstructure
1	Vacuum	Quench in water	Almost continuous line of microcracks and Au-rich particles in the bond centerline
2	Vacuum	Flow of water	Discontinuous microcracks along the bond centerline and Au-rich particles in the joint centerline. The size and amount of the Au-rich particles increased
3	Vacuum	Air	No microcracks. Au-rich particles seemed to precipitate along the grain boundary in the joint centerline. The size and amount of the Au-rich particles increased more than previous two cases
4	Argon	Flow of water	Near continuous microcracks along the joint centerline. Au-rich particles in the joint centerline area
5	Argon	Air	No microcracks with Au-rich particles in the joint centerline

Table 10 shows the summary of the microstructure of TLP bonded SS 321 using Au-12Ge, bonding environment and cooling method. For all joining environments and cooling methods Au-rich particles appeared in the joint centerline. The size and amount of Au-rich particles seemed to increase as the cooling method changed from quenching in water to air-cooling. However, the size of the Au-rich particles was decreased as bonding atmosphere changed from air to argon. The faster the cooling method the lesser the time

Au atoms have to precipitate. However, with quenching in water and cooling with water flow microcracks appeared in the joint centerline. The Au-12Ge interlayer had a thickness of 100 μm . A thinner foil may have eliminated or significantly reduced the precipitation of Au-rich particles in the joint centerline.

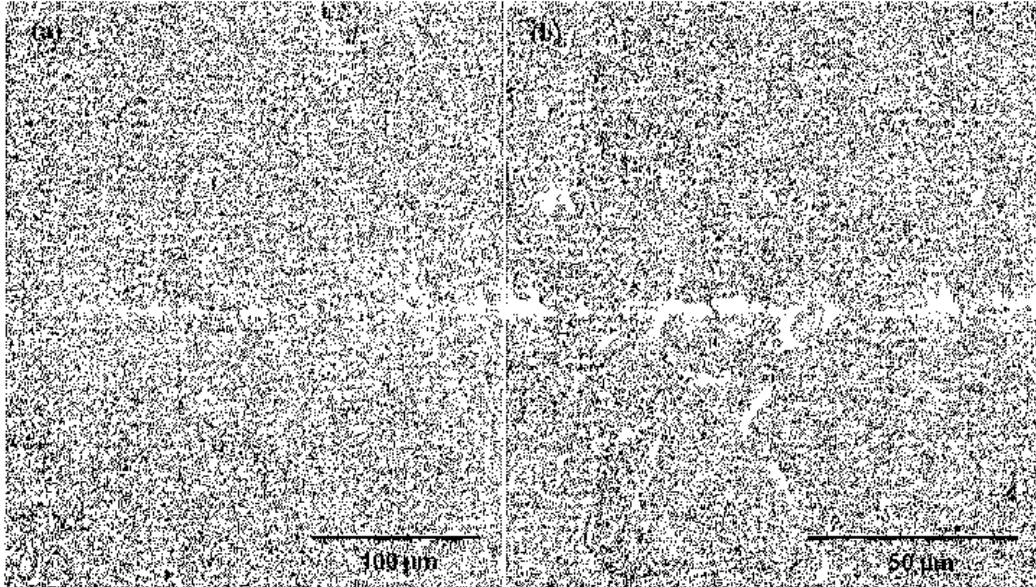


Figure 73. (a) SEM image of diffusion bonded SS 321 using Au-20Sn interlayer (100 μm) at 750°C for 10 h and (b) magnified image of (a).

Figure 73 shows SEM images of diffusion bonded SS 321 using Au-20Sn interlayer (100 μm) at 750°C for 10 h and. The interlayer did not diffuse completely into the base alloy. The microstructure of the joint centerline consisted of residual interlayer and Au-rich particles. The residual interlayer was not continuous. The composition of the residual interlayer was 76.2 wt. % Au, 5 wt. % Sn, 3.8 wt. % Fe, 6.2 wt. % Cr, 1 wt. % Ni, 2 wt. % Mn and small amount of other alloying elements. The composition in the base alloy side near base alloy/residual layer interface was 62 wt. % Fe, 8 wt. % Au, 0.7 wt. % Sn, 8 wt. % Ni, 16.5 wt. % Cr and 0.2 wt. % Mn. Figure 74 shows SEM image of diffusion

bonded SS 321 using Au-20Sn interlayer (100 μ m) at 800°C for 10 h. Although residual interlayer did not appear in the joint centerline there were many Au-rich particles.

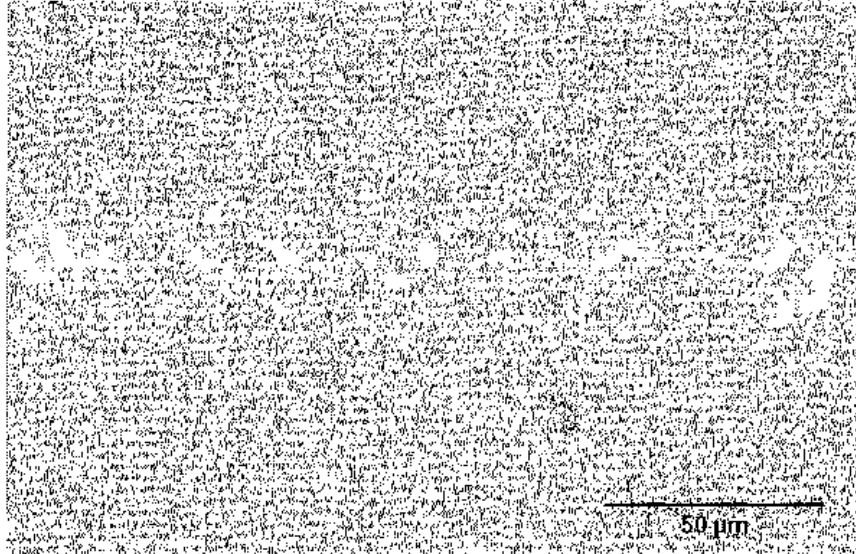


Figure 74. SEM image of diffusion bonded SS 321 using Au-20Sn interlayer (100 μ m) at 800°C for 10 h.

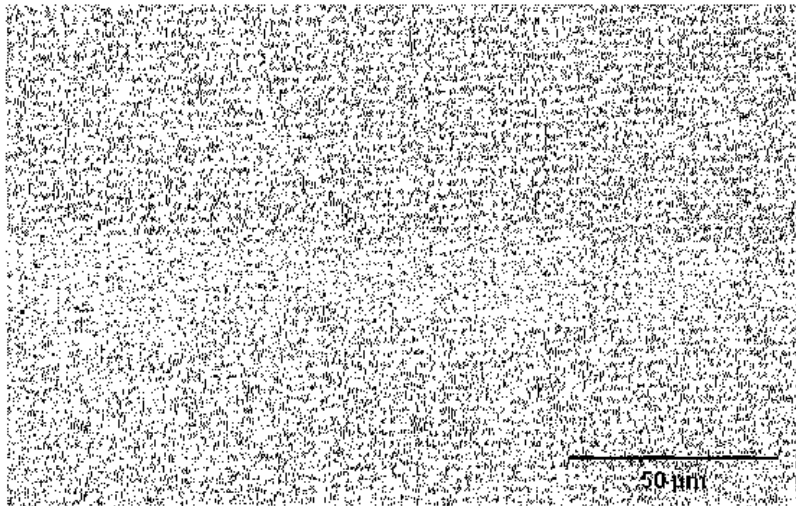


Figure 75. SEM image of diffusion bonded SS 321 at 1100°C for 10 h using Cu interlayer (25 μ m).

Figure 75 shows SEM image of diffusion bonded SS 321 at 1100°C for 10 h using Cu interlayer (25 μm). The interlayer did not diffuse completely into the base alloy. The joining interface contains 84.7 wt. % Cu, 2.1 % Ni, 1.2 % Cr, 1.8 % Fe and 2.2 % Mn in the interlayer side; and 65 wt. % Fe, 5.9 % Cu, 7.7 % Ni, 15.7 % Cr and 2.4 % Mn in the base metal side. SS 321 alloy has 69 wt. % Fe; the interdiffusion between Cu and SS 321 was much slower than between Cu and cp-Fe. The joining temperature was increased to 1120°C which is well above the melting temperature of pure Cu. Figure 76 shows SEM image of diffusion bonded SS 321 at 1120°C for 10 h using Cu interlayer (25 μm). Interdiffusion was not significantly increased by increasing joining temperature.

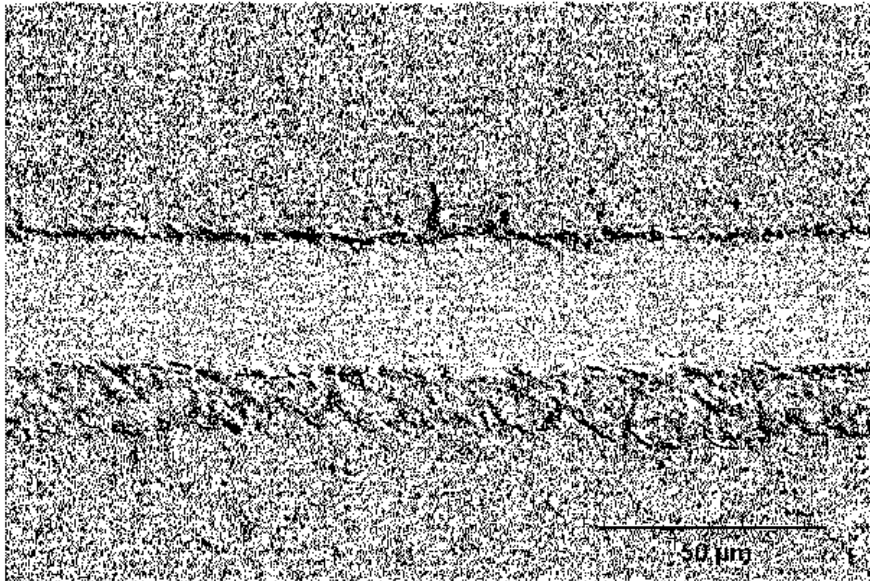


Figure 76. SEM image of diffusion bonded SS 321 at 1120°C for 10 h using Cu interlayer (25 μm).

Mechanical Properties

Table 11 shows tensile strengths of TLP bonded SS 321 using Au-12Ge or Au-20Sn interlayer. The maximum strength obtained for bonded SS 321 was 387 \pm 4 MPa with Au-

12Ge interlayer. This sample was bonded at 1050°C for 20 h in vacuum and cooled in air.

Table 11. Tensile strengths of TLP bonded SS 321 using Au-12Ge interlayer.

Interlayer	Temp. C	Time h	Surface Finish (grit#)	Clamping Torque	UTS (MPa)	Environment	Cooling
Base material (as machined specimen)					672±3		
Au-12Ge	950	10	1200	40 in-lb	272±3	Vacuum	Furnace
Au-12Ge	1050	15	1200	50 in-lb	254±5	Vacuum	Furnace
Au-12Ge	1050	15	1200	35 in-lb	278±4	Vacuum	Furnace
Au-12Ge	1050	20	1200	40 in-lb	222±3	Argon	Air
Au-12Ge	1050	20	1200	35 in-lb	371	Argon	Air
Au-12Ge	1050	20	1200	35 in-lb	360±6	Argon	Water Flow
Au-12Ge	1050	20	1200	35 in-lb	387±4	Vacuum	Air
Base Alloy	1050	20			550	Vacuum	Air
Au-20Sn	800	10	1200	50 in-lb	66	Argon	Furnace

This maximum strength is 57.6 % of the tensile strength of as-machined SS 321 and 70.4 % of the tensile strength of the base alloy that went through similar heat treatment process as diffusion bonded sample. There are several factors that are believed to affect the strength of the joint including the microstructure of the joint, the clamping load applied to the sample during bonding, the bonding temperature, the bonding time and the cooling rate. As the coefficients of thermal expansions of the jig, base alloy and mild steel bolts at bonding temperature were not available, it was not possible to calculate the exact clamping load. As a result, samples were bonded at different clamping loads (*ie* bonding pressure). The 35 in-lb clamping load provided the highest strength of the joint compared to other clamping loads. Although the argon bonding environment provided the best microstructure, the maximum strength was obtained for the sample bonded in

vacuum. Among the three different cooling methods, air cooling provided the best strength of the bonded sample.

The sample diameter was not bonded fully for tensile specimens. There were always an unbonded region around the edges of the circular tensile specimen; this region measures about $\sim 500 \mu\text{m}$ thick. The strength values shown in the Table 11 were measured without considering this fact. If we consider only the bonded area then the sample diameter decreases approximately 1 mm from the original dimension. In this case, the maximum strength obtained for bonded SS 321 was $490 \pm 5 \text{ MPa}$ which is 89 % of the base alloy that went through the similar heat treatment process as the diffusion bonded sample. Another factor that can enhance the strength for bonded sample is the use thinner foil. As discussed earlier, there were Au-rich particles in the joint centerline for all types of joining conditions. The precipitation of these particles disrupts the composition of the base alloy at least in the joint microstructures. Using a thinner foil, for example $25 \mu\text{m}$ thick Au-12Ge foil, would decrease the Au-rich particles in the joint centerline significantly. This, in turn, would increase the strength of the joint.

TLP Bonding of Inconel 718

Microstructures

Inconel 718 is a Ni-based superalloy. The compositions of the as-received Inconel 718 alloy are shown in Table 12. This alloy is age-hardened by the precipitation of second phases such as gamma prime (γ' - $\text{Ni}_3(\text{Al,Ti})$, cubic (L12) crystal structure) and gamma double-prime (γ'' - Ni_3Nb - bct (D0_{22})) phases. The later provides the strength. Before age hardening, solution annealing is done to dissolve all aging constituents (Nb, Al, and Ti) in the matrix and to obtain a homogeneous microstructure. The usual heat treatment

process for Inconel 718 alloy is to solution anneal at 1700-1850°F followed by rapid cooling in water, plus age hardening at 1325°F for 8 h, furnace cooling to 1150°F, holding at this temperature for a total aging time of 18 h, followed by air cooling.

Table 12. Composition (wt. %) of Inconel 718 superalloy.

Ni	Cr	Fe	Mo	Ti	Al	Nb	Cu	C	Co	Ta	W	Mn	Si	V
53.73	17.81	18.41	2.9	.99	.52	5.13	.04	.02	.18	<.01	.02	.06	.06	.02

Figure 77 shows SEM images of diffusion bonded Inconel 718 using Cu interlayer (25 μm) at 1050°C for 15 h in vacuum with slow cooling (4°C/min). The interlayer did not diffuse completely and the thickness of the residual interlayer obtained was ~19 μm . The composition of the residual interlayer obtained was 79 wt. % Cu, 11.8 wt. % Ni, 3 wt. %

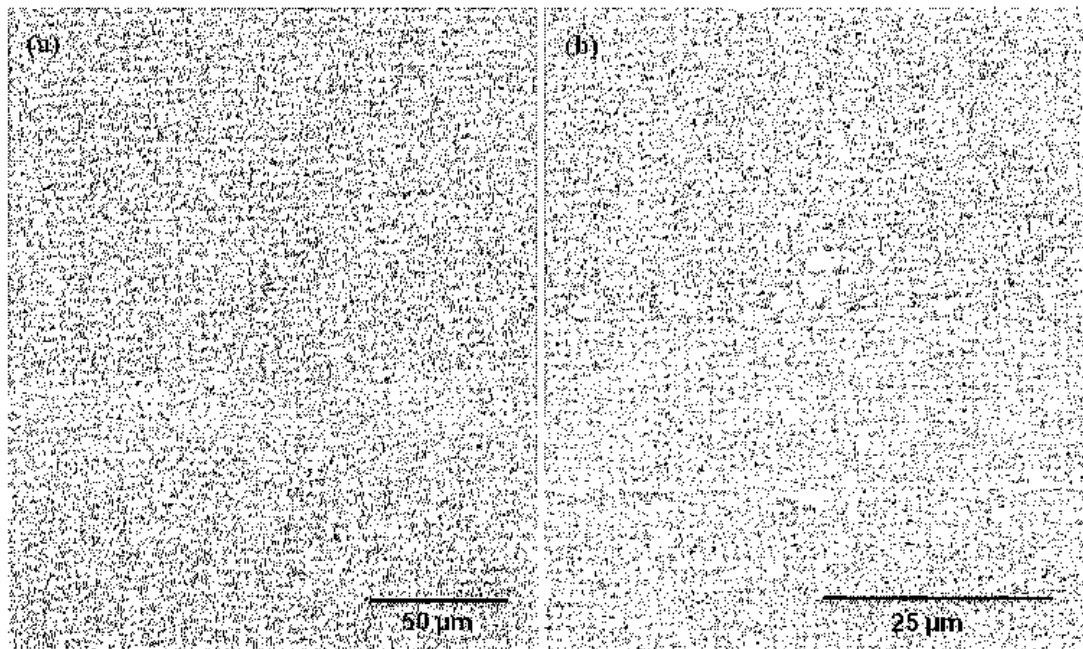


Figure 77. (a) SEM image of diffusion bonded Inconel 718 using Cu interlayer (25 μm) at 1050°C for 15 h in vacuum with slow cooling and (b) magnified image of (a).

Fe, 1.8 wt. % Cr, 1.3 wt. % Nb and small amounts of other alloying elements. Some precipitations were observed in the matrix approximately 15 μm away from the residual interlayer/base alloy interface. The composition found for these white particles was 38.8-39.9 wt. % Ni, 43-45 wt. % Nb, 3.9-4.9 wt. % Fe, 4-4.7 wt. Cr, 2.7-4 wt. % Ti and small amounts of other alloying elements. EDS analysis indicated that these white particles were either gamma double-prime or delta phase (the δ -phase, Ni_3Nb has an orthorhombic crystal structure and does not provide any strengthening effect). It was expected that the γ' , γ'' phases would dissolve during bonding. During cooling these constituents possibly precipitated.

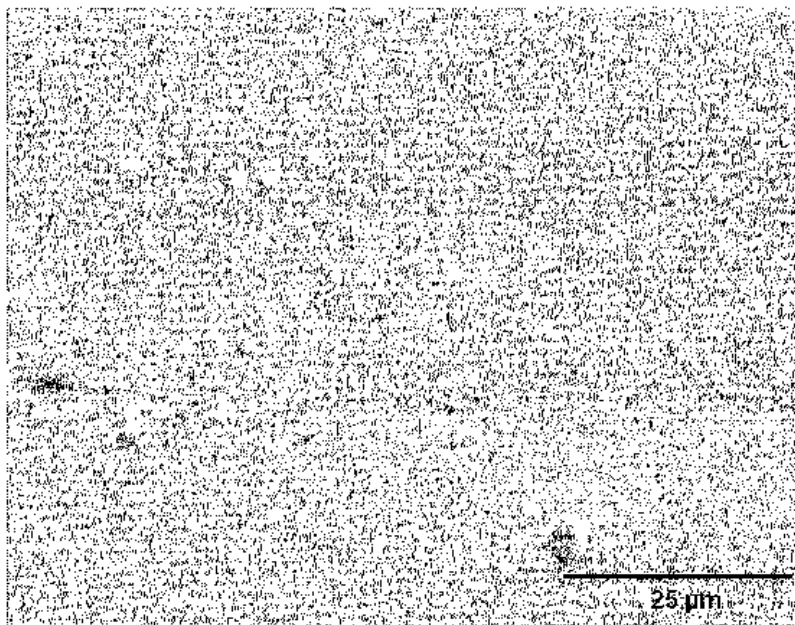


Figure 78. SEM image of diffusion bonded Inconel 718 using Cu (25 μm) at 1150°C for 5 h in vacuum with slow cooling (4°C/min).

Figure 78 shows SEM image of diffusion bonded Inconel 718 using Cu interlayer (25 μm) at 1150°C for 5 h in vacuum with slow cooling. Although the bonding temperature was much higher than the melting temperature of interlayer (1085°C) still the diffusion

was not complete. The thickness of the residual interlayer obtained was $\sim 19.9 \mu\text{m}$. The composition of the residual interlayer obtained was 68 wt. % Cu, 19.3 wt. % Ni, 4.8 wt. % Fe, 3.5 wt. % Cr, 1.1 wt. % Nb and small amounts of other alloying elements.

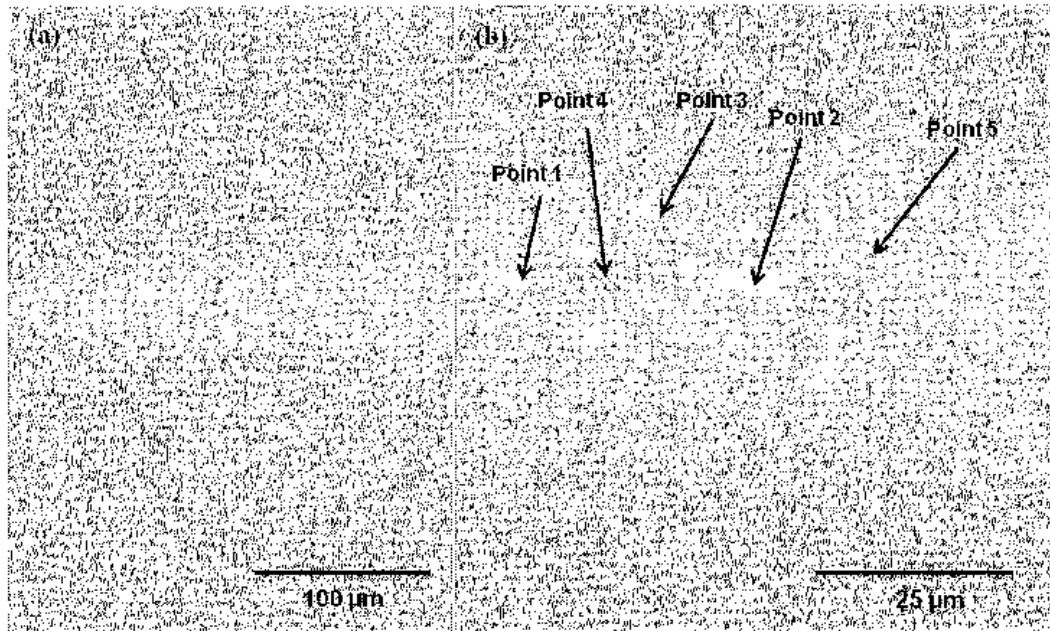


Figure 79. (a) SEM image of diffusion bonded Inconel 718 using Au-12Ge (100 μm) at 950°C for 15 h in vacuum and slow cooling and (b) magnified image of (a).

Table 13. EDS analysis of diffusion bonded Inconel 718 using Au-12Ge (100 μm) at 950°C for 15 h taken from 5 points shown in Figure 79 (b).

Elements (Wt. %)	EDS Point Number				
	1	2	3	4	5
Ni	36.37	24.79	32.06	35.91	35.24
Cr	4.54	15.62	16.95	16.78	11.5
Fe	7.11	14.8	15.76	15.06	11.7
Au	43.23	38.15	24.6	22.41	32.9
Ge	1.8	1.17	.48	1.84	0.56
Nb	0	0	0	0	1.25
Mo	0.45	0	3.79	3.4	2.1
Ti	2.92	1.55	1.53	1.55	2.26
Al	0.40	1.25	.91	0.6	0.18

Au-12Ge eutectic foils were also used to bond Inconel 718. Figure 79 shows SEM images of diffusion bonded Inconel 718 using Au-12Ge (100 μm) at 950°C for 15 h in vacuum and slow cooling. There was no residual interlayer in the joint centerline but some second phase particles were found in the bond centerline along the whole cross-section. The EDS elemental analysis of some points in Figure 79 (b) is shown in Table 13. The maximum Au obtained in the joint centerline was 43.23 wt. % and Nb content ranged from 0 to 1.25 wt. %. Precipitates were observed in the matrix 10-15 μm away from the bond centerline.

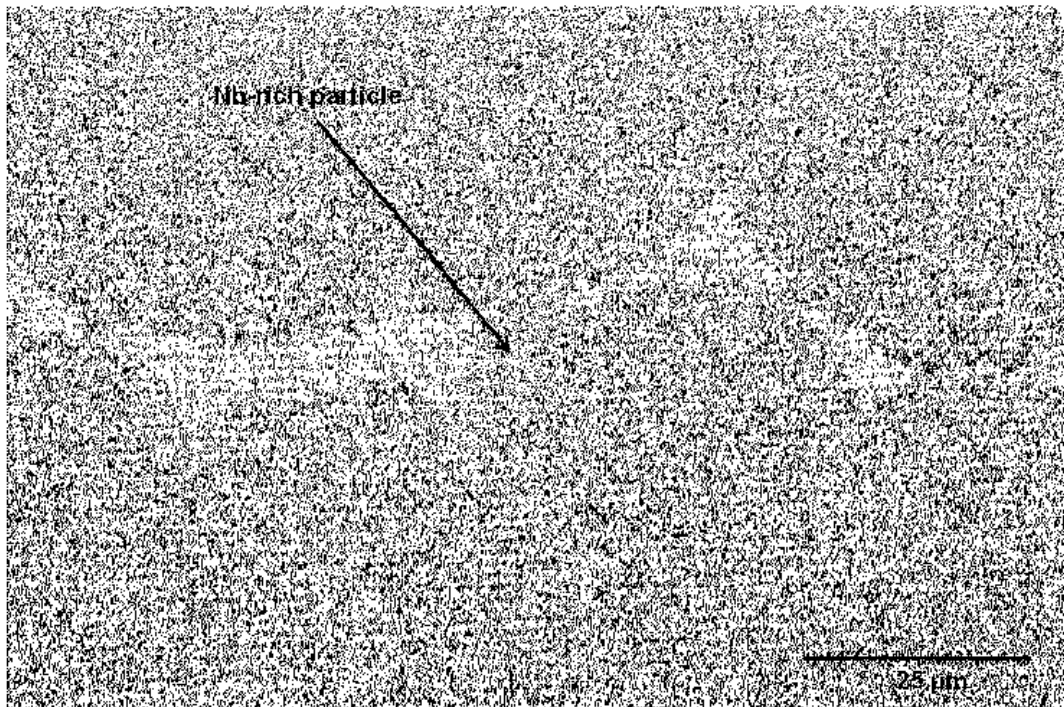


Figure 80. SEM image of diffusion bonded Inconel 718 using Au-12Ge (100 μm) at 1050°C for 15 h in vacuum and slow cooled.

Figure 80 shows SEM image of diffusion bonded Inconel 718 using Au-12Ge (100 μm) at 1050°C for 15 h in vacuum and cooled slowly. The bond centerline microstructure consisted of residual interlayer, micropores and eutectic-like microstructure next to the

residual interlayer. This eutectic-type microstructure extended from 16.4 to 20 μm on either side measured from the residual interlayer. The composition of the residual interlayer found was 60 wt. % Au, 3.2 wt. % Ge, 8.1 wt. % Ni, 14 wt. % Cr, 4.1 wt. % Fe and small amount of alloying elements. No Mo or Nb was found in the residual interlayer. A few Nb-rich particles were observed in the residual interlayer along the joint centerline. The composition of these particles observed was 33 wt. % Nb, 30 wt. % Ni, 7.4 wt. % Au, 7.6 wt. % Cr, 7.4 wt. % Fe, 5.7 wt. % Ge, 5.6 wt. % Mo and trace amounts of Ti and Al. The composition of the eutectic-like microstructure found was 13.9 wt. % Au, 2.6 wt. % Ge, 41.7 wt. % Ni, 15 wt. % Cr, 15.6 wt. % Fe, 5.4 wt. % Nb, 2.1 wt. % Mo, 0.8 wt. % Ti and trace amounts of other alloying elements. No precipitates were observed near the joint centerline.

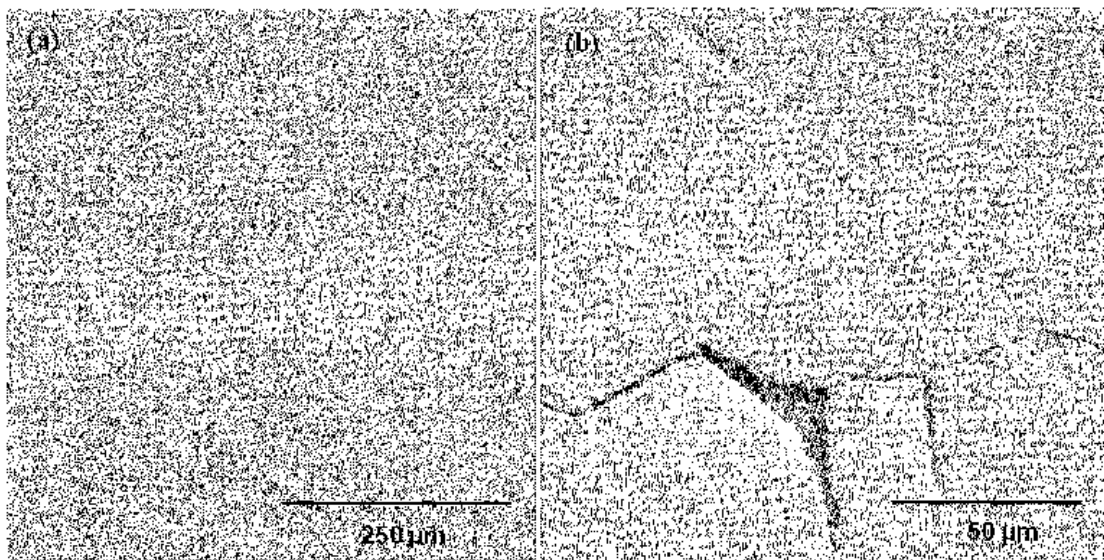


Figure 81. (a) SEM image of diffusion bonded Inconel 718 using Au-12Ge (100 μm) at 1050°C for 15 h in vacuum and quenched in water and (b) magnified image of (a).

To get rid of residual interlayer and second phase particles from the bonded area, a faster cooling method was applied. Figure 81 shows SEM images of diffusion bonded Inconel

718 using Au-12Ge (100 μm) at 1050°C for 15 h in vacuum and quenched in water. No residual interlayer observed in the bond centerline. However, near-continuous microcracks appeared in the joint centerline.

Figure 82 shows SEM images of diffusion bonded Inconel 718 using Au-12Ge (100 μm) at 1050°C for 15 h in vacuum and cooled in air. The interlayer did not diffuse completely and the thickness of the residual interlayer varied from 1.3-2.5 μm . A few micropores were observed in the residual interlayer. The composition of the residual interlayer obtained was 61 wt. % Au, 1.3 wt. % Ge, 14.2 wt. % Ni, 5.3 wt. % Fe, 11 wt. % Cr, 1 wt. % Ti and trace amounts of other elements with no Nb and Mo. The composition in the

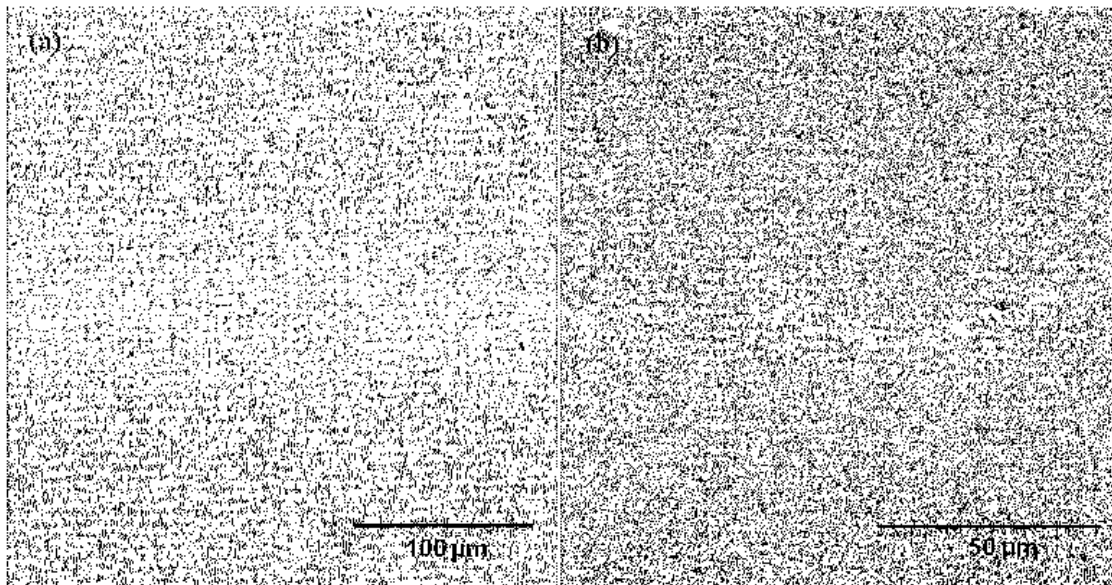


Figure 82. (a) SEM image of diffusion bonded Inconel 718 using Au-12Ge (100 μm) at 1050°C for 15 h in vacuum and cooled in air and (b) magnified image of (a).

base alloy near interface found was 12.7 wt. % Au, 2.6 wt. % Ge, 44 wt. % Ni, 14.8 wt. % Cr, 15 wt. % Fe, 4.5 wt. % Nb, 1.7 wt. % Mo and trace amounts Ti and Al. The amount of Au reduced to 5 wt. % approximately 50 μm away from the residual interlayer

and the original composition of the base alloy was almost restored except the amount of Ni which was 44 wt. % compared to 53.7 wt. % in the base alloy. No precipitates were observed in the microstructure of the bonded area because the aging constituents remained in the solution due to the faster cooling rate.

Figure 83 shows a SEM image of diffusion bonded Inconel 718 using Au-12Ge (100 μm) at 1050°C for 20 h in vacuum and cooled in air. By increasing bonding time by 5 h residual interlayer was avoided; however, micropores appeared along the bond centerline. These micropores extended approximately 2-2.5 μm along the longitudinal direction. The

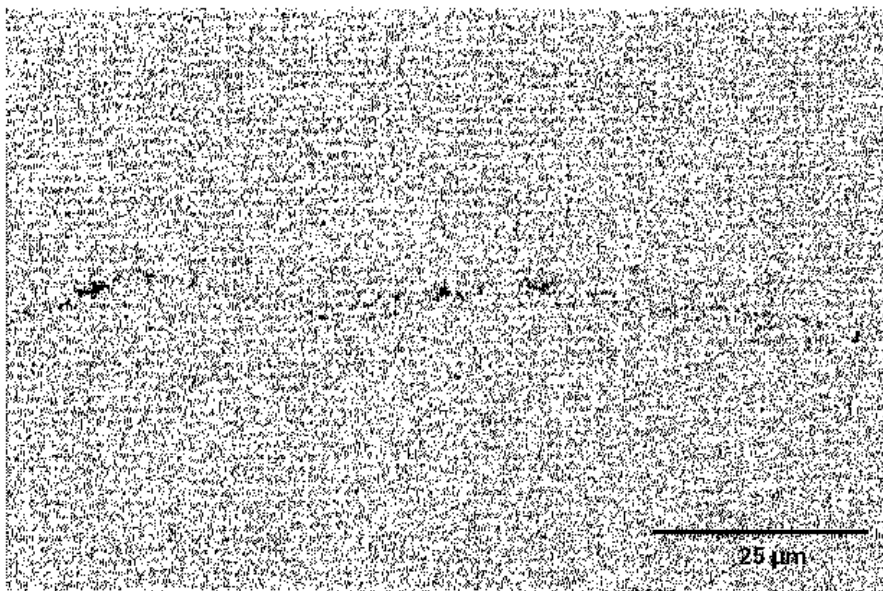


Figure 83. SEM image of diffusion bonded Inconel 718 using Au-12Ge (100 μm) at 1050°C for 20 h in vacuum and cooled in air.

EDS point analysis from the porous regions in the bond centerline provided 5.3 wt. % Au, 3.9 wt. % Ge, 22.9 wt. % Ni, 7.6 wt. % Fe, 8.3 wt. % Cr, 3.1 wt. % Nb, 1.7 wt. % Mo, 23.7 wt. % Al, 16.5 wt. % O and 1.2 wt. % Ti. Higher amounts of Al and O resulted from the contamination of polishing media ($\gamma\text{-Al}_2\text{O}_3$). Al_2O_3 particles might be trapped in

the pores during polishing. The compositions next to the porous region in the base alloy obtained were 10.7 wt. % Au, 2.8 wt. % Ge, 41.5 wt. % Ni, 16.4 wt. % Fe, 17.3 wt. % Cr, 3.8 wt. % Nb, 3.3 wt. % Mo, .96 wt. % Ti and trace amounts of other alloying elements. As the cooling method was faster, no precipitates were formed. The microstructures of the joint centerline of diffusion bonded Inconel 718 are summarized in Table 14.

Table 14. Summary of the microstructure of TLP bonded Inconel 718 using Cu and Au-12Ge interlayer in vacuum.

Interlayer	Interlayer Thickness (μm)	Bonding Temp. ($^{\circ}\text{C}$)	Bonding Time (h)	Cooling Method	Bond Centerline Microstructure
Cu	25	1050	15	Slow	Residual interlayer ($\sim 19 \mu\text{m}$)
Cu	25	1150	5	Slow	Residual interlayer ($\sim 19.9 \mu\text{m}$)
Au-12Ge	100	950	15	Slow	No residual interlayer, second phase particles in the joint centerline
Au-12Ge	100	1050	15	Slow	Residual interlayer, micropores and eutectic-like microstructure next to the residual interlayer
Au-12Ge	100	1050	15	Water quench	No residual interlayer, near-continuous microcracks
Au-12Ge	100	1050	15	Air quench	Residual interlayer (1.3-2.5 μm), a few micropores
Au-12Ge	100	1050	20	Air quench	No residual interlayer, micropores extended 2-2.5 μm along the longitudinal direction

Mechanical Properties

Table 15 shows tensile strengths of diffusion bonded Inconel 718. The maximum strength obtained for bonded sample was 400 MPa at 950 $^{\circ}\text{C}$ for 15 h in vacuum with slow cooling. Although the microstructure was able to be replicated, the strength could not be replicated at these joining conditions. The strengths for other samples bonded at the same bonding conditions obtained were 193 and 170 MPa. There were a few reasons that the

strengths of the joints were low including second phase particle in the bond centerline, residual interlayer and no hardening effects from precipitates. It has been mentioned before that the aging constituents were dissolved in the matrix during isothermal bonding and stayed in the matrix during fast cooling thereby providing no strengthening effects. During slow cooling from 950°C or above, δ -phase usually forms for this alloy which provides no strengthening effect.

Table 15. Tensile strength of diffusion bonded Inconel 718.

Interlayer	Temp. (°C)	Time (h)	surface finish (grit#)	clamping Torque (in-lb)	UTS (MPa)	Environment	Cooling
Base material (as machined specimen)					1012.8		
Au-12Ge	950	15	1200	50	400	vacuum	furnace
Au-12Ge	1050	15	1200	35	327	vacuum	water

TLP Bonding of Ti-6Al-4V (Grade 5 Ti alloy)

Microstructure

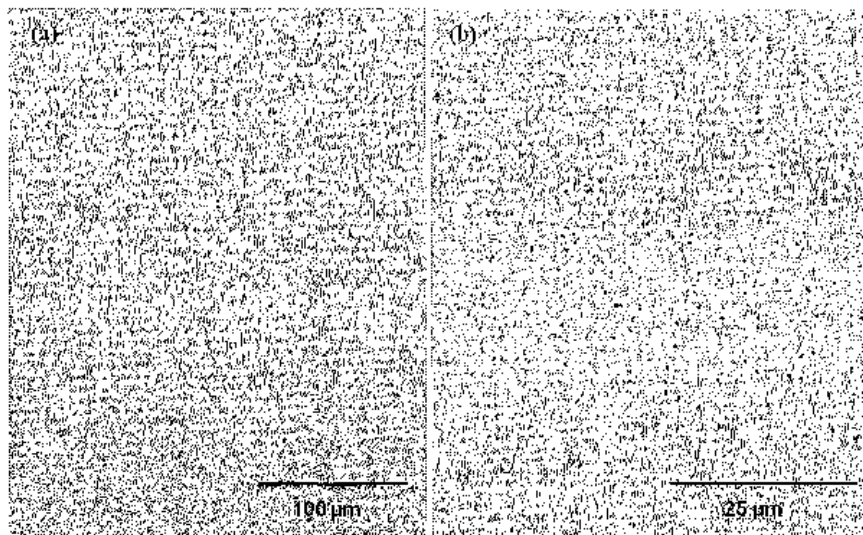


Figure 84. (a) SEM image of diffusion bonded Ti-6Al-4V using Cu (25 μ m) interlayer at 900°C for 10 h in vacuum, slow-cooled and (b) magnified image of (a).

Ti alloys are categorized as α alloy, near- α alloy, α - β alloy and β alloy. Ti-6Al-4V (also known as grade 5 Ti alloy or VT6 Ti alloy) is an α - β alloy containing dual α - and β -phase. This alloy has been diffusion bonded using Cu interlayer (25 μm). Figure 84 shows SEM images of diffusion bonded Ti-6Al-4V using Cu (25 μm) interlayer at 900°C for 10 h in vacuum, slow-cooled. Cu interlayer did not diffuse completely in the base alloy. The thickness of the residual interlayer found was 20.2-22.7 μm . The composition of the residual interlayer obtained was 25.6 wt. % Cu, 68 wt. % Ti, 5 wt. % Al, and no V. The base metal next to the bond interface had 8 wt. % Cu, 77.7 wt. % Ti, 11.7 wt. % Al and 1.4 wt. % V. The microstructure near the interface was a two-phase mixture.

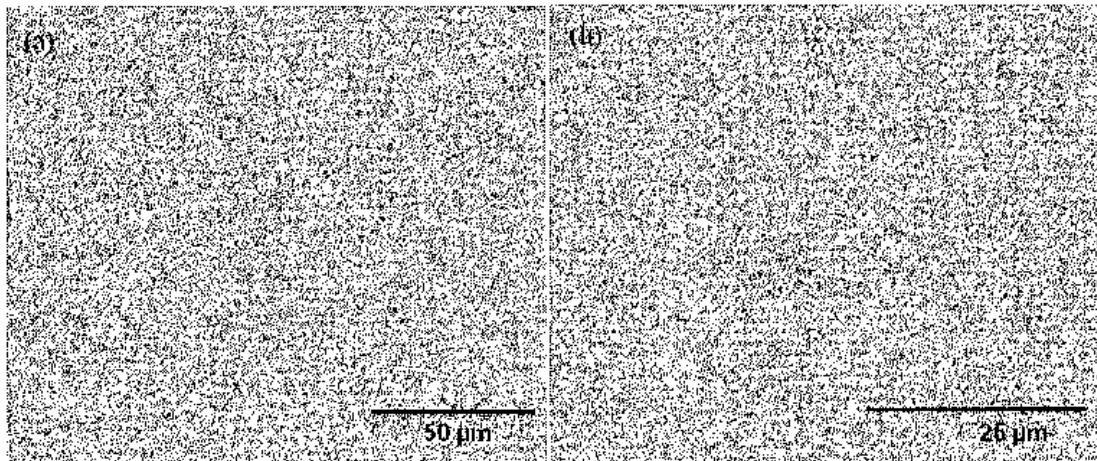


Figure 85. (a) SEM image of diffusion bonded Ti-6Al-4V using Cu (25 μm) interlayer at 950°C for 10 h in vacuum, slow-cooled and (b) magnified image of (a).

Figure 85 shows SEM images of diffusion bonded Ti-6Al-4V using Cu (25 μm) interlayer at 950°C for 10 h in vacuum, slow-cooled. At these bonding conditions, the interdiffusion between interlayer and the base alloy was high enough that no residual interlayer was observed. It was difficult to find the centerline of bonded area under SEM.

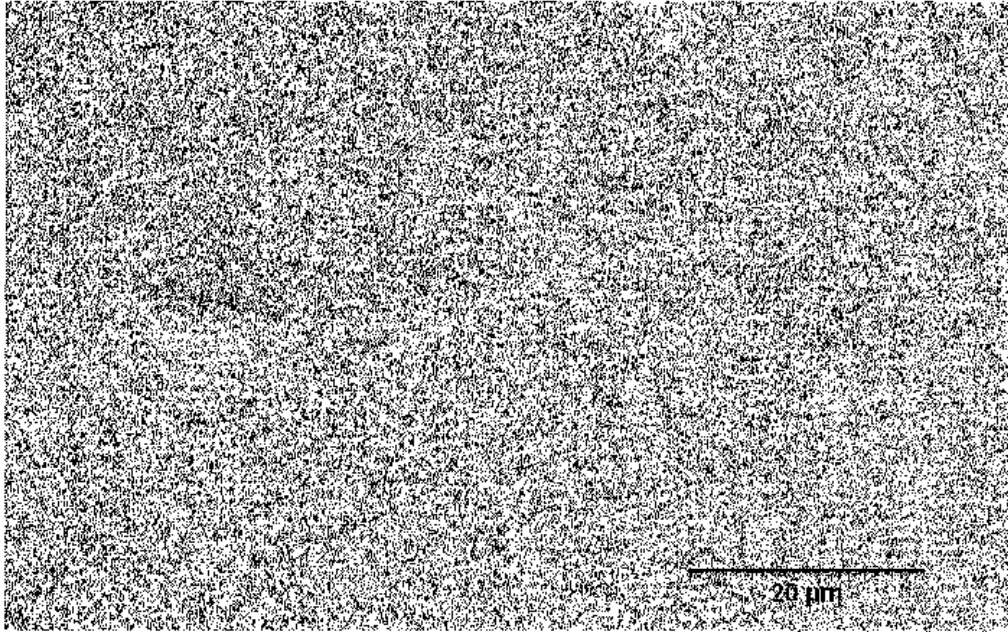


Figure 86. SEM image of diffusion bonded Ti-6Al-4V using Cu (25 μm) interlayer at 950°C for 10 h in vacuum and slow-cooled.

The EDS area analysis of the microstructure of bonded area found was 80.1 wt. % Ti, 8.8 wt. % Cu, 8.1 wt. % Al and 2.1 wt. % V. Figure 86 shows high a magnification image of the microstructure of bonded area. The bond centerline microstructure appeared as dendrites of Cu in the matrix of base alloy. White dendrites contained more Cu than the darker area did. The EDS point analysis of the white dendrites obtained was 17 wt. % Cu, 74.7 wt. % Ti, 5.9 wt. % Al and .3 wt. % V. On the other hand, darker area provided 2.6 wt. % Cu, 84.5 wt. % Ti, 9.8 wt. % Al and 1.4 wt. % V.

Figure 87 shows SEM images of diffusion bonded Ti-6Al-4V using Cu (25 μm) interlayer at 1000°C for 10 h in vacuum, slow-cooled in furnace. For these bonding conditions, the microstructures obtained were very similar to those obtained for the previous case. The bond centerline microstructure was not easily distinguishable and looked like fine dendrites in the matrix of base alloy. The bond centerline microstructures

contained 9.7 wt. % Cu, 78.3 wt. % Ti, 9.7 wt. % Al and 0.8 wt. % V. The microstructures were much more homogeneous than appeared in previous joining conditions as the Cu-rich dendrites were not observed. The microstructures of the bond centerline of diffusion Ti-6Al-4V are summarized in Table 16.

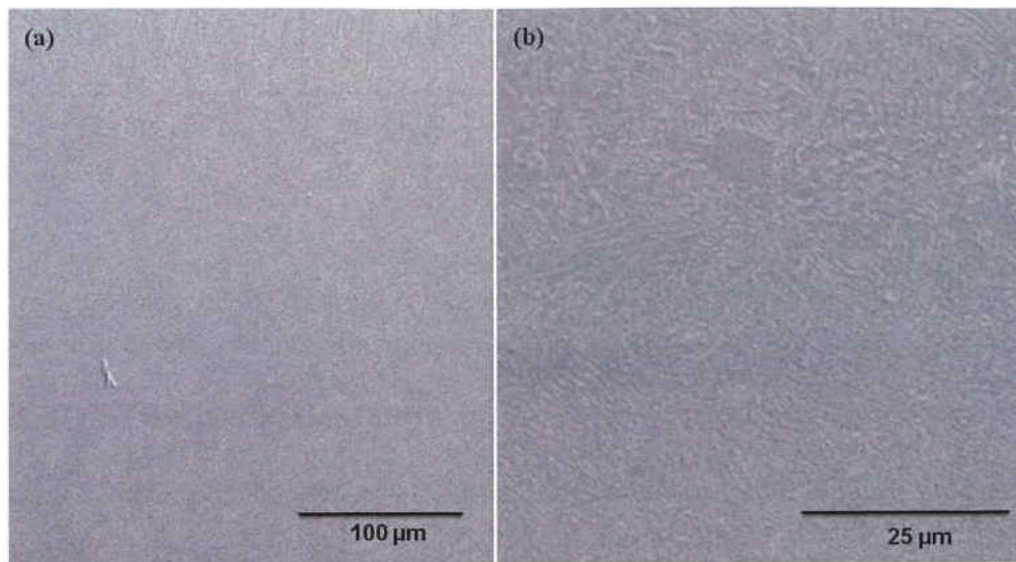


Figure 87. (a) SEM image of diffusion bonded Ti-6Al-4V using Cu (25 μm) interlayer at 1000°C for 10 h in vacuum, slow-cooled and (b) magnified image of (a).

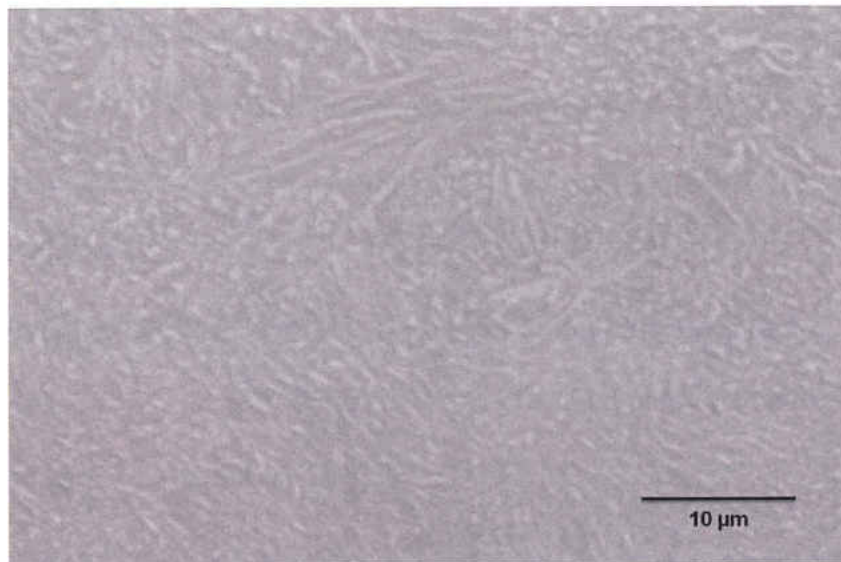


Figure 88. SEM image of diffusion bonded Ti-6Al-4V using Cu (25 μm) interlayer at 1000°C for 10 h in vacuum, slow-cooled in furnace.

Table 16. Summary of the microstructure of TLP bonded Ti-6Al-4V using interlayer in vacuum.

Interlayer	Interlayer Thickness (μm)	Bonding Temp. ($^{\circ}\text{C}$)	Bonding Time (h)	Cooling Method	Bond Centerline Microstructure
Cu	25	900	10	Slow	Residual interlayer (20.2-22.7 μm)
Cu	25	950	10	Slow	No residual interlayer, dendrites of Cu in the matrix of base alloy
Cu	25	1000	10	Slow	No residual interlayer, eutectic type microstructure

Conclusions

The best microstructures obtained for diffusion bonded SS 321 using Au-12Ge interlayer at 1050 $^{\circ}\text{C}$ bonding temperature in vacuum followed by cooling in air. Some Au-rich particles observed in the microstructure of bonded area for all joining conditions.

Although these particles were smaller for water cooling, microcracks appeared in the joint centerline at faster cooling rate. Using Cu interlayer to bond SS 321 seemed impractical as the interdiffusion was extremely slow. Au-Sn interlayer can be used to bond SS 321; however, the joining conditions have to be optimized. The maximum strength of the joint for SS 321 obtained was 70.4 % of the strength of base alloy.

However, if we consider the cross-sectional area that actually bonded (as it was observed that there was an unbonded ring about 500 μm thick along the outside edge of the bond line) then the joint strength increases to 89 % of the base alloy. It is expected that using a thinner Au-12Ge foil would decrease the second phase particles, which, in turn, would increase the strength of the joint.

The interdiffusion between Cu interlayer and Inconel 718 was too slow and Cu was found to be an impractical interlayer to join Inconel 718. No residual interlayer was found in the

joint centerline while Au-12Ge interlayer was used. However, micropores were observed in the joint centerline. The maximum strength obtained for bonded Inconel was 400 MPa at 950°C for 15 h with slow cooling. The optimum joining conditions for Inconel-(Au-12Ge) are yet to be determined. Although the interdiffusion between Cu and SS 321 or Inconel was highly sluggish, it was much faster with Cu and Ti-6Al-4V system. Cu diffused into Ti-6Al-4V remained as solution. However, no measurable strengths were found for this system possibly due to thermal expansion mismatch between tensile specimen and jig or microstructure disruption such as inappropriate ratio of α and β phases.

CHAPTER V

CONCLUSIONS

Commercially pure Ti, Fe and Ni were TLP bonded using commercially available pure or binary interlayers. The formation of intermetallics was dictated by the thermodynamics of the systems and can easily be explained using the binary or ternary equilibrium diagrams. It was certain that the formation of intermetallics in the microstructure of the bonded area affected the strengths of the joint adversely. However, the intermetallics formed in a eutectic type microstructure (Ti joints using Cu interlayer) did not affect the joint strengths appreciably. The maximum strength obtained was 502 MPa using Cu interlayer and the joints reached ~98% of the strength of the base metal.

Diffusion bonding of cp-Fe using Cu interlayers showed a residual Cu interlayer from 1000-1100°C for most bonding times. At 1100°C for 5h, no residual Cu was obtained; however, a porous microstructure appeared along the bond centerline. The microstructure of the base metal near bond centerline contained dispersed Au-rich particles when Au-12Ge interlayer was used. Generally, at a higher bonding temperature ($>0.7 T_m$) bulk diffusion is expected. However, grain boundary diffusion was observed only in the Fe-Cu joining systems even at 1100°C. TLP joining of cp-Ni using Al interlayer was not useful because of the formation of intermetallics at any bonding conditions. Although no intermetallics were found when bonding using Cu interlayer, no appreciable strength was obtained. The tensile strength obtained for the joint with Au-12Ge interlayer was very

low compared to the strength of base alloy.

Voids seemed to appear in the joint centerline if the joining temperature was much higher compared the melting temperature of the interlayer. This happened probably due to the differences in the diffusion rate for base metal and interlayer atoms. This phenomenon is known as the “Kirkendal effect”. This effect has been observed for joining Ti using Cu, Fe using Cu and Au-12Ge interlayers, and Ni using Al interlayers.

Simple TLP joints were also modeled using DICTRA/Thermocalc software. These software were used to simulate the concentration profiles of Cu and Ni in a Cu-Ni diffusion joint. DICTRA was also used to optimize the mobility parameters from experimental diffusion data obtained at 1000°C for Ni-Cu system. The interdiffusion coefficient calculated from the optimized mobility parameter agreed well with the experimental data. The simulated profile obtained at 1100°C agreed very well with experimental profile. For the Ni-Al binary and the Ni-(Au-12Ge) ternary systems the simulated profiles did not match with the simulated profiles because of the lack of proper mobility and thermodynamic database. This modeling method can be extended to different joining systems and for higher order alloys provided that appropriate mobility and thermodynamic database are available.

Generally, interdiffusions appeared to be much slower when a commercial alloy was TLP bonded using same interlayer compared to the pure base metal. For example, the interdiffusion between Cu and SS 321 was much slower than that observed between Fe and Cu. Another interesting phenomenon was observed during slow cooling when SS 321 or Inconel 718 was TLP bonded using Au-12Ge interlayers which might be called back-

diffusion.

Au-rich particles were observed in the microstructure of the TLP bonded SS 321 joints for all joining conditions. Microcracks appeared in the joint centerline at faster cooling rates than air-cooling. This could be due to the supersaturated solid solution retained at room temperature. During slower cooling rate the Au atoms precipitate out of the supersaturated solid solution, thus reducing the chances of microcracks. The maximum corrected strength of the joint for SS 321 obtained was 89 % of the strength of the base alloy. It is expected that using a thinner Au-12Ge foil would decrease the second phase particles, which, in turn, would increase the strength of the joint. Inconel 718 was TLP bonded using Cu and Au-12Ge interlayer. Residual interlayer disappeared at the expense of the introduction of a porous microstructure when Au-12Ge interlayer was used. The maximum strength obtained for bonded Inconel 718 was 400 MPa at 950°C for 15 h with slow cooling. The optimum joining conditions for Inconel-(Au-12Ge) are yet to be determined. Although the interdiffusion between Cu and SS 321 or Inconel 718 was highly sluggish, it was much faster between Cu and Ti-6Al-4V system. Cu diffused into Ti-6Al-4V remained as solution and eutectic mixture. However, any measurable strength is yet to be determined.

APPENDICES

Appendix A

Problem Setup for Optimization of Mobility Parameters

@@ problem_setup.DCM

@@-----

@@ FILE FOR READING THERMODYNAMIC DATA AND SETTING UP THE
KINETIC

@@ PARAMETERS WHICH ARE NEEDED FOR AN OPTIMIZATION OF THE
FCC PHASE

@@ IN THE BINARY NI-CU SYSTEM.

@@-----

@@ RETRIEVE THERMODYNAMIC DATA FROM A USER DEFINED
DATABASE

@@

go data

sw ssol4

dcf-sp

cu ni

rej ph *

rest ph fcc_al

get

@@

@@ APPEND THE KINETIC DATA FROM THE MOBILITY DATABASE IN
ORDER TO

@@ HAVE SOME DUMMY PARAMETERS.

@@

app mob2

def-sp

cu ni

rej ph *

res ph fcc_al

get

@@ GO TO THE DICTRA MODULE AND DEFINE THE KINETIC PARAMETERS.
THE

@@ VARIABLE V1,V2,V3 AND V4 ARE TO BE OPTIMIZED. NOTE THAT IF

@@ YOU ARE OPTIMIZING PARAMETERS FOR A PHASE WITH MAGNETIC

@@ CONTRIBUTION. I.E. USING BOTH MF- AND MQ-PARAMETERS YOU

@@ MIGHT HAVE TO ENTER THE PARROT MODULE AND GO BACK BEFORE

@@ ENTERING PARAMETERS CONTAINING VARIABLES.

@@

go par

go d-m

@@ MOBILITY OF NI IN NI

ENTER-MOB-DATA

MQ(FCC_A1&NI,NI:VA) 298.15 -287000-69.8*T; 6000 N

@@ MOBILITY OF NI IN CU

ENTER-MOB-DATA

MQ(FCC_A1&NI,NI:VA) 298.15 -236400+R*T*LN(2.7E-4); 6000 N

@@ MOBILITY OF NI INTERACTION BETWEEN NI AND CU

ENTER-MOB-DATA

MQ(FCC_A1&NI,NI,NI:VA;0) 298.15 V1+V2*T; 6000 N

@@ MOBILITY OF CU IN CU

ENTER-MOB-DATA

MQ(FCC_A1&CU,NI:VA) 298.15 -205872+R*T*LN(4.9E-5); 6000 N

@@ MOBILITY OF CU IN NI

ENTER-MOB-DATA

MQ(FCC_A1&CU,NI:VA) 298.15 -258153+R*T*LN(5.7E-5); 6000 N

@@ MOBILITY OF CU INTERACTION BETWEEN CU AND NI

ENTER-MOB-DATA

MQ(FCC_A1&CU,NI:VA;0) 298.15 V3+V4*T; 6000 N

@@

@@ GO TO PARROT AND SAVE SETUP ON FILE

@@

go parrot

create-new-store-file opt

set-inter

Interdiffusion Coefficients in Ni-Cu System at 1000°C (dop file)

\$-----
\$ DOP-FILE CONTAINING EXPERIMENTAL INFORMATION USED DURING
THE
\$ OPTIMIZATION IN PARROT (COMPARE WITH POP-FILE USED WHEN
EVALUATING
\$ THERMODYNAMIC DATA). THE EXPERIMENTAL DATA HERE STEAM
FROM
\$ V.T. Heumann, K.J. Grundhoff, Z. Metallk. 63 (1972) 173.
\$
\$ CONSULT THE THERMO-CALC USER'S GUIDE TO LEARN MORE ABOUT
SYNTAXES
\$ FOR OPTIMIZATION OF THERMODYNAMIC DATA.
\$-----

ENTER CONST P0=101325
TABLE_HEAD 10
CREATE_NEW @@,1
C-S PH FCC=ENT 1
S-C T=1273,N=1,P=P0
S-C X(Cu)=@1
EXPERIMENT LOGDC(FCC_A1,CU,CU,NI)=@2:1
TABLE_VALUES
0.05 -14.8

0.1	-14.78
0.146	-14.68
0.204	-14.655
0.25	-14.633
0.301	-14.575
0.35	-14.49
0.4	-14.415
0.455	-14.433
0.505	-14.275
0.553	-14.21
0.6	-14.165
0.65	-14.06
0.7	-13.96
0.755	-13.833
0.804	-13.725
0.859	-13.567
0.904	-13.475
0.93	-13.4125
0.953	-13.34
0.979	-13.325

TABLE_END

SAVE

END

Kinetic Database Used in DICTRA/ThermoCalc for Ni-Cu system

\$ Mobility database for Ni-Cu system.

```
ELEMENT VA VACUUM          0.0000E+00 0.0000E+00 0.0000E+00!
ELEMENT NI FCC_A1          5.8690E+01 4.7870E+03 2.9796E+01!
ELEMENT cu FCC_A1          6.3546E+01 5.0040E+03 3.3150E+01!
TYPE_DEFINITION % SEQ *!
DEFINE_SYSTEM_DEFAULT SPECIE 2 !
DEFAULT_COMMAND DEF_SYS_ELEMENT VA !
DATABASE_INFO NIST-NiMob database is for Ni-rich fcc alloys. !
PHASE FCC_A1 % 2 1.0 1.0 !
CONSTITUENT FCC_A1 :NI,CU : VA : !
ZEROVOLUME_SPECIES VA !
PARA VS(FCC_A1) 0 1.0e-5; 3.00E+3 N !
$$$$$ Mobility of Ni $$$$$$$$$$$$
PARAMETER MQ(FCC_A1&NI,NI:VA;0) 298.15 -287000-69.8*T; 6.00E+3 N !
PARAMETER MQ(FCC_A1&NI,CU:VA;0) 298.15 -236400+R*T*LN(2.7E-4);
6.00E+3 N !
PARAMETER MQ(FCC_A1&NI,CU,NI:VA;0) 298.15 -114969+79.78*T; 6.000E+3 N
!
$$$$$ Mobility of CU $$$$$$$$$$$$
PARAMETER MQ(FCC_A1&CU,CU:VA;0) 298.15 -205872+R*T*LN(4.9E-5);
6.00E+3 N !
```

PARAMETER MQ(FCC_A1&CU,NI:VA;0) 298.15 -258153+R*T*LN(5.7E-5);
6.00E+3 N !

PARAMETER MQ(FCC_A1&CU,CU,NI:VA;0) 298.15 -101869+87.8*T; 6.000E+3 N
!

Problem Setup in DICTRA to Calculate Concentration Profile of Diffusing Species

@@LOGFILE GENERATED ON PC/WINDOWS NT DATE 2010-12-28

@@With gradual heating, dwelling and cooling,,

go da

sw ssol4

def-spec ni cu

rej ph * all

res ph fcc_a1

get

app us nicumob.tdb

def-sys ni cu

rej ph * all

res ph fcc_a1

get

go d-m

set-cond

GLOBAL

T

0

630+time*.0667

11145

y

1373.37

y

1373.37-time*.0667

11145

N

enter-region

Ni-Cu

enter-grid

NI-CU

150e-6

LINEAR

301

enter-phase

ACTIVE

NI-CU

MATRIX

fcc_a1

enter-comp

NI-CU

FCC_A1

ni

w-p

cu

read cu.dat

set-sim-time

1c6

YES

1e5

1E-07

1E-07

s-s-c

0

1

2

NO

ACTIVITIES

YES

YES

1.0

2

NO

YES

save prac2 y

set-inter

Appendix B

Verification of mass conservation:

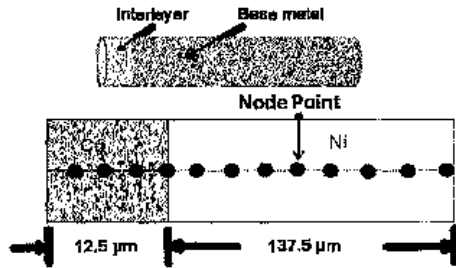


Figure 89. Diffusion couple used for simulation in DICTRA

Amount of Cu before simulation in the diffusion joint:

$$\text{Amount of Cu (wt. \%)} = \frac{\text{wt. \% Cu}}{\text{wt. \% Cu} + \text{wt. \% Ni}} = \frac{(\text{vol.} \times \text{density}) \text{ of Cu}}{(\text{vol.} \times \text{density}) \text{ of Cu} + (\text{vol.} \times \text{density}) \text{ of Ni}}$$

Considering the interlayer and base metal as cylinders (Fig. 7) we obtain

$$\text{Amount of Cu (wt. \%)} = \frac{\pi r^2 h_{Cu} \times \rho_{Cu}}{\pi r^2 h_{Cu} \times \rho_{Cu} + \pi r^2 h_{Ni} \times \rho_{Ni}}$$

Where h_{Cu} and h_{Ni} are the lengths of Cu interlayer and Ni, respectively, ρ_{Cu} and ρ_{Ni} are the densities of Cu and Ni, respectively, r is the diameter of the Cu foil and Ni

Because of equal diameter we get:

Amount of Cu (wt. %) =

$$\frac{h_{Cu} \times \rho_{Cu}}{h_{Cu} \times \rho_{Cu} + h_{Ni} \times \rho_{Ni}} = \frac{(12.5 \times 99.999 + 137.5 \times .001) \times 8.94}{(12.5 \times 99.999 + 137.5 \times .001) \times 8.94 + (12.5 \times .00001 + 137.5 \times 99.999) \times 8.902} = 8.458\%$$

Density of Cu and Ni are 8.94 and 8.902 gcm^{-3} , respectively. Interlayer contains 99.999 wt. % Cu and .001 wt. % Ni, base metal Ni contains 99.9 wt. % Ni and 0.1 wt. % Cu.

Amount of Ni (wt. %) =

$$\frac{h_{Ni} \times \rho_{Ni}}{h_{Cu} \times \rho_{Cu} + h_{Ni} \times \rho_{Ni}} = \frac{(12.5 \times .00001 + 137.5 \times 99.999) \times 8.902}{(12.5 \times 99.999 + 137.5 \times .001) \times 8.94 + (12.5 \times .00001 + 137.5 \times 99.999) \times 8.902} = 91.542\%$$

From simulated profiles:

$$\text{Total amount of Cu (wt. \%)} = \frac{\sum(\text{wt. \% Cu} \times \Delta x)}{150 \mu\text{m}} = \frac{\Delta x \sum(\text{wt. \% Cu})}{150 \mu\text{m}}$$

Where Δx is the distance between two node points and equals 0.5 μm . The amount of Cu was calculated at every 0.5 μm distance. The length of the interlayer was 12.5 μm and the length of base metals was 137.5 μm .

1. At 1050°C for 15 h: Cu wt. % = 9.168; Ni wt. % = 91.17

2. At 1070°C for 10 h: Cu wt. % = 9.16; Ni = 91.17%

3. At 1100°C for 10 h: Cu wt. % = 9.186; Ni = 91.15%

Average Cu wt. % = 9.171

There is a difference of 0.713 wt. % between the starting amount of Cu and the estimation from DICTRA with an error of 8.43 %. For Ni the difference is .379 % with an error of 0.41%

REFERENCES

- [1] <http://www.msm.cam.ac.uk/phase-trans/2005/Amir/bond.html>.
Accessed: August 2, 2012.
- [2] Gale, W.F., Butts, D.A., 2004, "Transient liquid phase bonding," *Sci. Technol. Weld. Joining*, 9, pp. 283–300.
- [3] Sheward, G. E., 1985, "High temperature brazing in controlled atmosphere," Oxford, UK, Pergamon Press.
- [4] Thwaites, C.J., 1982, "Capillary joining – brazing and soft soldering," Hertfordshire, UK, Research Studies Press.
- [5] Zorc, T.B. (ed.), 2000, *ASM handbook*, vol. 6, "Welding Brazing and Soldering," Materials park, OH, ASM international.
- [6] Rahman, A.H.M.E., and Cavalli, M.N., 2010, "Strength and Microstructure of Diffusion Bonded Titanium Using Silver and Copper Interlayers," *Mater. Sci. Eng. A*, 527, pp. 5189-5193.
- [7] Khan, T.I., and Wallach, E.R., 1995, "Transient Liquid-phase Bonding of Ferritic Oxide Dispersion Strengthened Superalloy MA957 Using a Conventional Nickel Braze and a Novel Iron-base Foil," *J. Mater. Sci.* 30(20), pp. 5151-5160.
- [8] Ward, A.G., and Taylor, J. W., 1957, "Dynamic Solution-Rate Studies of Solid Metals in Liquid Metals," *J. Inst. Metals*, 86, pp. 36-42.
- [9] Wu, X., Chandel, R.S. and Li, H., 2001, "Evaluation of transient liquid phase bonding between nickel-based superalloys," *J. Mater. Sci.* 36(6), pp. 1539-1546.

- [10] Blue, C.A., Sikka, V.K., Blue, R.A., and Lin, R.Y., 1996, "Infrared transient-liquid-phase joining of SCS-6/ β 21S titanium matrix composite," *Metall. Mater. Trans. A*, 27(12), pp. 4011-4017.
- [11] Tung, S.K., Lim, L.C., and Lai, M.O., 1995, "Solidification Phenomena in Nickel Base Brazes Containing Boron and Silicon," *Scripta Mater.*, 34(5), pp. 763-769.
- [12] Sakamoto, A., Fujiwara, C., Hattori, T., and Sakai, S., 1989, "Optimizing Processing Variables in High-Temperature Brazing with Nickel-based Filler Metals," *Weld. J.*, 68(3), pp. 63-71.
- [13] <http://www.aws.org/wj/supplement/Hosking/ARTICLE3.pdf>
Accessed: Nov 10, 2012
- [14] Sheng, Z.G., Hu, X.E., Lin, B.H., Ping, W.A., Qing, W., and Lie, R.J., 2009, "A study on transient liquid phase diffusion bonding of Ti-22Al-25Nb alloy," *Mater. Sci. Eng. A*, 499, pp. 101-105.
- [15] Lee, H.K., Han, H.S., Son, K.J., Hong, S.B., 2006, "Optimization of Nd:YAG laser welding parameters for sealing small titanium tube ends," *Mater. Sci. Eng. A*, 415 (1-2) pp. 149-55.
- [16] Peng, H., Jiuhai, Z., Ronglin, Z., and Xiaoqiang, L., 1999, "Diffusion Bonding Technology of a Titanium Alloy to a Stainless Steel Web With a Ni Interlayer," 1999, *Mater. Character.*, 43(5), pp. 287-292.
- [17] Kahraman, N., Gulenc, B., and Findik, F., 2007, "Corrosion and mechanical-microstructural aspects of dissimilar joints of Ti-6Al-4V and Al plates," *Int. J. Impact. Eng.*, 34, pp. 1423-1432.
- [18] Elrefaey, A., and Tillmann, W., 2009, "Solid state diffusion bonding of titanium to steel using a copper base alloy as interlayer," *J. Mat. Process. Technol.*, 209, pp. 2746-2752.

- [19] Atasoy, E., and Kahraman, N., 2008, "Diffusion bonding of commercially pure titanium to low carbon steel using a silver interlayer," *Mater. Character.*, 59, pp. 1481-1490.
- [20] Kundu, S., Ghosh, M., Laik, A., Bhanumurthy, K., Kale, G.B., and Chatterjee, S., 2005, "Diffusion bonding of commercially pure titanium to 304 stainless steel using copper interlayer," *Mater. Sci. Eng. A*, 407, pp. 154-160.
- [21] Dezellus, O., Andrieux, J., Bosselct, F., Sacerdote-Peronnet, M., Baffie, T., Hodaj, F., Eustathopoulos, N., and Viala, J.C., 2008, "Transient liquid phase bonding of titanium to aluminium nitride," *Mat. Sci. Eng. A*, 495, pp. 254-258.
- [22] Sheng, G.M., Huang, J.W., Qin, B., Zhou, B., Qui, S.Y., and Li, C., 2005, "An experimental investigation of phase transformation superplastic diffusion bonding of titanium alloy to stainless steel," *J. Mat. Sci.*, 40(24), pp. 6385-6390.
- [23] Khan, T.I., and Wallach, E.R., 1995, "Transient liquid-phase bonding of ferritic oxide dispersion strengthened superalloy MA957 using a conventional nickel braze and a novel iron-base foil," *J. Mater. Sci.*, 30(20), pp. 5151-5160.
- [24] Floreen, S., and Hayden, H.W., 1968, "The Influence of Austenite and Ferrite on the Mechanical Properties of Two Phase Stainless Steels Having Microduplex Structures," *Trans. Quart. ASM*, 61, pp. 489-499.
- [25] Blumfield, D., Clark, G.A., and Guha, P., 1981, "Welding duplex austenitic-ferritic stainless steel," *Met. Construct.*, 5, pp. 269-273.
- [26] <http://www.asminternational.org/content/ASM/StoreFiles/ACFAB86.pdf>
Accessed: March 17, 2013
- [27] Singer, R.F., 1994, "Advanced Materials and Processes for Land-based Gas Turbines," *Materials for Advanced Power Engineering Part 2*, pp. 1707-1729.
- [28] Seth, B.B., 2000, "Superalloys-The Utility Gas Turbine Perspective," *Proceedings of the 9th International Symposium on Superalloys*, Seven Springs, USA.

- [29] Reed, R.C., 2006, "The Superalloys: Fundamentals and Applications," Cambridge University Press, Cambridge.
- [30] Rae, C., 2009, "Alloys by Design: Modelling Next Generation Superalloys," *Mater. Sci. Technol.* 25(4) pp.479-487.
- [31] Caron, P., and Khan, T., 1999, "Evolution of Ni-based Superalloys for Single Crystal Gas Turbine Blade Applications," *Aerosp. Sci. Technol.*, 3(8), pp. 513-523.
- [32] Kashyap, B.P., and Chaturvedi, M.C., 2000, "Activation Energy for Superplastic Deformation of IN 718 Superalloy," *Scr. Mater.*, 43, pp. 429-433.
- [33] Idowu, O.A., Richards, N.L., and Chaturvedi, M.C., 2005, "Effect of Bonding Temperature on Isothermal Solidification Rate During Transient Liquid Phase Bonding of Inconel 738LC Superalloy," *Mater. Sci. Eng. A*, 397(25), pp. 98-112.
- [34] Jalilian, F., Jahazi, M., and Drew, R.A.L., 2006, "Microstructural Evolution During Transient Liquid Phase Bonding of Inconel 617 Using Ni-Si-B Filler Metal," *Mater. Sci. Eng. A* 423(15), pp. 269-281.
- [35] Thamburj, R., Wallace, W., and Goldak, J.A., 1983, "Post-weld Heat-treatment Cracking in Superalloys," *Int. Met. Rev.* 28, pp. 1-22.
- [36] Ojo, O.A., Richards, N.L., and Chaturvedi, M.C., 2004, "Microstructural Study of Weld Fusion Zone of TIG Welded IN 738LC Nickel-based Superalloy" *Scr. Mater.*, 51, pp. 683-688.
- [37] Speich, G.R., Gula, J.A., and Fisher, R.M., 1996, "Diffusivity and Solubility Limit of Cu in Alpha and Gamma iron," *The electron microprobe*, edited by T.D. MacKinley, John Wiley & Sons. Inc. New York, pp. 525-542.
- [38] Okamoto, H., Massalski, T.B., Swartzendruber, L.J., and Beck, P.A., 1992, "Alloy phase diagram," *ASM Handbook*, 10th ed., vol. 3, pp. 2-69.

- [39] Hosseini, S.A., and Manesh, H.D., 2009, "High-strength, High-conductivity Ultra-fine Grains Commercial Pure Copper Produced by ARB Process," *Mater. Design*, 30, pp. 2911–2918.
- [40] Padron, T., Khan, T. I., and Kabir, M. J., 2004, "Modelling the Transient Liquid Phase Bonding Behavior of a Duplex Stainless Steel Using Copper Interlayers," *Mat. Sci. & Eng. A*, 385, pp. 220-228.
- [41] Tuah-Poku, I., Dollar, M. and Massalski, T.B., 1988 "A Study of the Transient Liquid Phase Bonding Process Applied to a Ag/Cu/Ag Sandwich Joint," *Metall. Trans. A*, 19(3), pp. 675-686.
- [42] Zhou, Y., Gale, F. W., and North, T. H., 1995, "Modelling of Transient Liquid Phase Bonding," *Int. Mater. Rev.*, 40(5) pp. 181-196.
- [43] Zhou, Y., 2001, "Analytical Modeling of Isothermal Solidification During Transient Liquid Phase (TLP) Bonding," *J. Mater. Sci. Letter.*, 20(9), pp. 841-844.
- [44] Arafin, M. A., Medraj, M., Turner, D. P., and Bocher, P., 2007, "Transient Liquid Phase Bonding of Inconel 718 and Inconel 625 with BNi-2: Modeling and Experimental Investigations," *Mat. Sci. & Eng. A*, 447, pp. 125–133.
- [45] Illinworth, T. C., Golosnoy, I. O., Gergely, V., and Clyne, T. W., 2005, "Numerical Modelling of Transient Liquid Phase Bonding and Other Diffusion Controlled Phase Changes," *J. Mat. Sci.*, 40, pp. 2505-2511.
- [46] Zhou, Y., and North, T. H., 1993, "Kinetic Modelling of Diffusion-Controlled, Two-Phase Moving Interface Problems," *Modelling Simul. Mater. Sci. Eng.*, 1(4), pp. 505.
- [47] Rappaz, M., Bellet, M., and Deville, M., 2003, "*Numerical Modeling in Materials Science and Engineering*," Springer Series in Computational Mathematics, Springer-Verlag, Berlin.
- [48] MacDonald, W.D., and Eagar, T.W., 1992, "Transient Liquid Phase Bonding," *Ann. Rev. Mater. Sci.*, 22, pp. 23–46.

- [49] Zhou, Y., Gale, W.F., and North, T.H., 1995, "Modelling of Transient Liquid Phase Bonding," *Int. Mater. Rev.*, 40, pp.181–196.
- [50] Sundman, B., Jansson, B., and Andersson, J.O., 1985, "The Thermo-Calc Databank System," *Calphad*, 9, pp. 153-190.
- [51] Andersson, J.O., Hoglund, L., Jonsson, B., and Agren, J., 1990, *Fundamentals and Applications of Ternary Diffusion*, Purdy GR ed. Pergamon Press, New York, pp. 153-163.
- [52] Onsager, L., 1931, "Reciprocal Relations in Irreversible Processes I," *Phys. Rev.*, 37, pp. 405-426.
- [53] Onsager, L., 1931, "Reciprocal Relations in Irreversible Processes II," *Phys. Rev.*, 38, pp.2265-2279.
- [54] Andersson, J.O., and Ågren, J., 1992, "Models for Numerical Treatment of Multicomponent Diffusion in Simple Phases," *J Appl. Phys.*, 72, pp. 1350-1355.
- [55] Boltzmann, L., 1894, "Zur Integration der Diffusionsgleichung bei variablen Diffusionscoefficienten," *Wiedemanns Ann. Physik*, 53, pp. 959-964.
- [56] Matano, C., 1933, "On the Relation Between the Diffusion-Coefficients and Concentrations of Solid Metals (The Nickel-Copper System)," *Japan. J. Phys.*, 8, pp. 109-113.
- [57] Schmalzried, H., 1981, "Solid State Reactions," *Verlag Chemie*, pp. 87-89.
- [58] F.J.A.den Broeder, 1969, "A General simplification and Improvement of the Matano-Boltzmann Method in the Determination of the Interdiffusion Coefficients in Binary Systems," *Scrip. Metallurgica*, 3, pp. 321-326.
- [59] Sauer F., and Freise, V., 1961, "Diffusion in Binary Mixtures with Volume Change," *Z. Elektrochem.* 66, pp. 353-363.
- [60] Wagner, C., 1969, "The Evaluation of Data Obtained with Diffusion Couples of Binary Single-phase and Multiphase Systems," *Acta Metall.*, 17, pp. 99-107.

- [61] Agren, J., 1992, "Computer Simulations of Diffusional Reactions in Complex Steels," *Iron Steel Inst. Jpn. Int.*, 32(3), pp. 291-296.
- [62] Borgenstam, A., Engstrom, A., Hoglund, L., and Agren, J., 2000, "DICTRA, a Tool for Simulation of Diffusional Transformations in Alloys," *J. Phase Equilibria*, 21 (3), pp. 269-280.
- [63] Ghosh, G., 2001, "Dissolution and Interfacial Reactions of Thin-Film Ti/Ni/Ag Metallizations in Solder Joints," *Acta mater.*, 49, pp. 2609-2624.
- [64] Jönsson, B., 1995, "Assessment of the Mobilities of Cr, Fe and Ni in Binary fcc Cr-Fe and Cr-Ni Alloys," *Scand. J Metall.*, 24(1), pp. 21-27.
- [65] Mackliet, C.A., 1958, "Diffusion of Fe, Co, and Ni in Single Crystal of Pure Cu," *Phys. Rev.*, 109, pp.1964-1970.
- [66] Monma, K., Sato, H., and Oikawa, H., 1964, "Diffusion of Ni and Cu in Nickel-Copper Alloys (in Japanese)," *Nippon Kinzoku Gakkaishi*, 28, pp.192-196.
- [67] Anand, M.S., Murarka, S.P., and Agarwala, R.P., 1965, "Diffusion of Copper in Nickel and Aluminum," *J. Appl. Phys.* 36(3), pp. 860-3862.
- [68] Heumann, Th., and Grundhoff, K.J., 1972, "Diffusion and Kirkendal Effect in Cu-Ni Alloys." *Z Metallkd*, 63, pp.173-180.
- [69] Iijima, Y., Hirano, K., and Kikuchi, M., 1982, "Determination of Intrinsic Diffusion Coefficients in a Wide Concentration Range of a Cu-Ni Couple by the Multiple Markers Method," *Trans. Japan Inst. Metals*, 23(1), pp.19-23.
- [70] http://www.thermocalc.se/res/Manuals/DICTRA26_examples.pdf.
- [71] Yamamoto, T., Takashima, T., and Nishida, K., 1980, "Interdiffusion in the ζ -Solid Solution of a Ni-Al System," *Trans. Japan Inst. Metals*, 21(9), pp. 601-608.
- [72] Helander, T., and Ågren, J., 1999, "A phenomenological treatment of diffusion in Al-Fe and Al-Ni alloys having B2-b.c.c. ordered structure," *Acta. Mater.*, 47(4), pp. 1141-1152.